Aleksandra Snoch

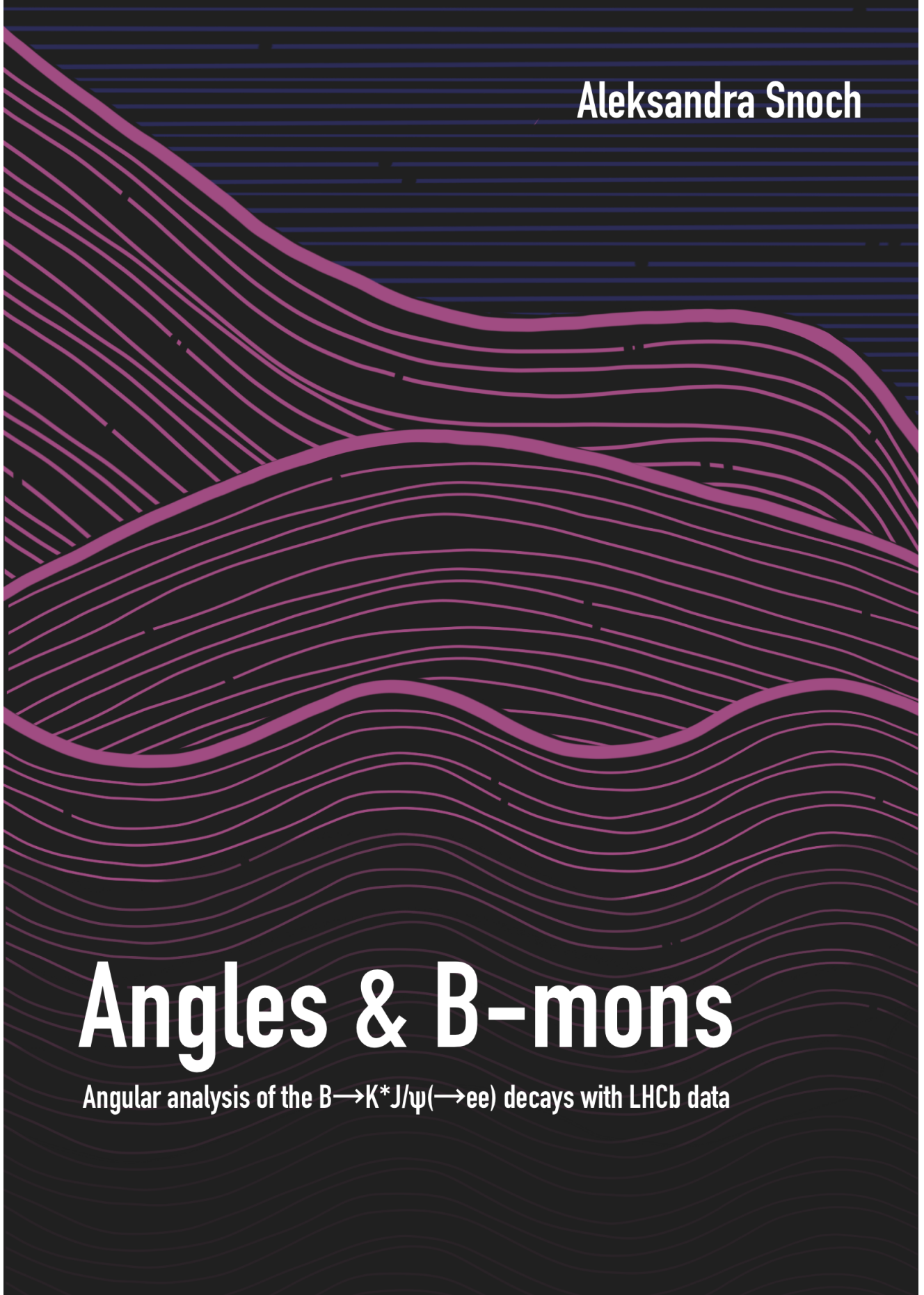

# Angles & B-mons

Angular analysis of the $B \to K^* J/\psi(\to ee)$ decays with LHCb data

# Angles and B-mons

Angular analysis of $B^0 \to K^{0*} J/\psi(\to e^+ e^-)$ decays with LHCb data

*Angles and B-mons.*
*Angular analysis of* $B^0 \to K^{0*} J/\psi(\to e^+e^-)$ *decays with LHCb data*

Cover: Aleksandra Snoch

Printed by Gildeprint
ISBN: 978-94-6496-188-1



This work is part of the research programme of the Netherlands Organisation for Scientific Research (NWO). The work is carried out at the National Institute of Subatomic Physics (Nikhef) in Amsterdam, The Netherlands.

university of groningen

# Angles and B-mons

Angular analysis of $B^0 \to K^{0*} J/\psi(\to ee)$ decays with LHCb data

**PhD thesis**

to obtain the degree of PhD at the
University of Groningen
on the authority of the
Rector Magnificus Prof. J.M.A. Scherpen
and in accordance with
the decision by the College of Deans.

This thesis will be defended in public on

Friday 20 September 2024 at 11.00 hours

by

**Aleksandra Snoch**

born on 2 October 1992

**Supervisor**
Prof. A. Pellegrino

**Co-supervisor**
Dr. W. Hulsbergen

**Assessment Committee**
Prof. D. Boer
Prof. C.F.F. van Den Broeck
Prof. W. Verkerke

# Contents

# Introduction

The current understanding of the Universe in terms of interactions between matter and forces is described by the Standard Model (SM) of Particle Physics. However, despite being the best model up to date, it still does not offer a complete description of all known phenomena. These open questions lead to searches for physics beyond the Standard Model.

One of the ways to test the theoretical assumptions of the Standard Model is by analysing rare decays of a beauty quark $b$, that are highly suppressed by the SM. In particular the $b \to sll$ transition is used, in which a beauty quark $b$ decays to a strange quark $s$ and two leptons $l^+l^-$ of opposite charge. Results of several physics analyses of this decay hint at deviations from the SM predictions and motivate further research. A full description of the theoretical framework and detailed motivations and results of these searches are presented in Chapter 1.

One of the particle physics experiments performing these searches is the LHCb experiment located at the CERN Large Hadron Collider (LHC). It is a combination of particle detectors forming a forward spectrometer, optimised for the detection of decays of charm and beauty quarks. The experimental setup is described in Chapter 2. The LHCb physics program includes heavy ion studies, W and Z boson production, and searches for new exotic particles. Among the analyses performed by the LHCb collaboration are the studies of rare b hadron decays, $b \to sll$ . An example of such a decay is $B^0 \to K^{0*}\mu^+\mu^-$ . The angular analysis of this decay showed a tension with the Standard Model predictions. This observation encourages a search for new physics also in the electron channel, $B^0 \to K^{0*}e^+e^-$ .

The work presented in this thesis is a part of the angular analysis of the $B^0 \to K^{0*}e^+e^-$ decays. The full angular analysis will be performed on the rare channel, while in this thesis the analysis of the corresponding control channel, $B^0 \to K^{0*}J/\psi(\to e^+e^-)$, is presented.

The analysis is performed with data collected by the LHCb experiment in LHC Run 1 (2011 - 2012) and Run 2 (2015-2016 and 2017-2018), corresponding to a total integrated luminosity of 9.0 $\text{fb}^{-1}$. To evaluate the efficiencies, the size of various background contributions, and the fit itself, corresponding simulated data were used. The details of the data and simulation are explained in Chapter 3, including the selection and reconstruction details.

The reconstruction and selection result in a distortion of the angular distributions of the final state particles. These effects are known as acceptance effects and are accounted for by a parametrisation with a series of polynomials and trigonometric functions, described in Chapter 4. The acceptance parametrisation is included in the maximum likelihood fit to the data: a four-dimensional fit to the invariant mass and three decay angles.

The fitting procedure is validated on the control channel $B^0 \to K^{0*}J/\psi(\to e^+e^-)$ in both simulation and data. The fitting procedure and the background treatment are further explained in Chapter 5. The results are compared to the results from the previous $B^0 \to K^{0*}\mu^+\mu^-$ analyses in the corresponding control channels. To complete the understanding of the results, possible sources of systematic uncertainties were studied. The considered uncertainty sources are connected to the acceptance parametrisation, the choice of simulation-data correction strategy and the electron reconstruction resolution.

# 1 | Motivation

The current understanding of the universe in terms of interactions between matter and forces is described by the Standard Model (SM) of Particle Physics [1]. This model contains two types of particles: *fermions* (quarks and leptons) that are the building blocks of matter, and *bosons* that carry the interactions. One of these interactions, the strong force, allows quarks to form more complex particles that consist of two or three quarks, respectively called mesons and baryons. The mesons containing the beauty quark $b$ will be the focus of this dissertation. In particular, the research presented in this thesis concerns the transition $b \to sll$, in which a beauty quark $b$ decays to a strange quark $s$ and two leptons $l$. Rare decays of this type allow stringent tests of the theoretical foundations of the Standard Model.

The Standard Model, its theoretical framework and predictions are described in Section 1.1. The details of the physics of rare $b \to sll$ decays and their role in the SM tests are discussed in Section 1.2. Sections 1.3 and 1.4 introduce the kinematics of the decay and its angular distributions, later used to derive the observables that can be compared with the Standard Model predictions. Similar tests were carried out by other particle physics experiments that resulted in a tension with theoretical predictions, are reported in Section 1.5.

## 1.1 Standard Model of Particle Physics

The Standard Model of Particle Physics describes all known elementary particles and the interactions among them. The elementary particles can be divided in two groups: matter particles (fermions) and interaction particles (bosons).

Each of the fermions can be described by a set of quantum numbers. The particles are divided into three families that have identical properties. Each of the

families consists of an up- and down-type quark, a charged lepton and a neutral lepton, a neutrino, and have increasingly higher masses, as indicated in Figure 1.1.

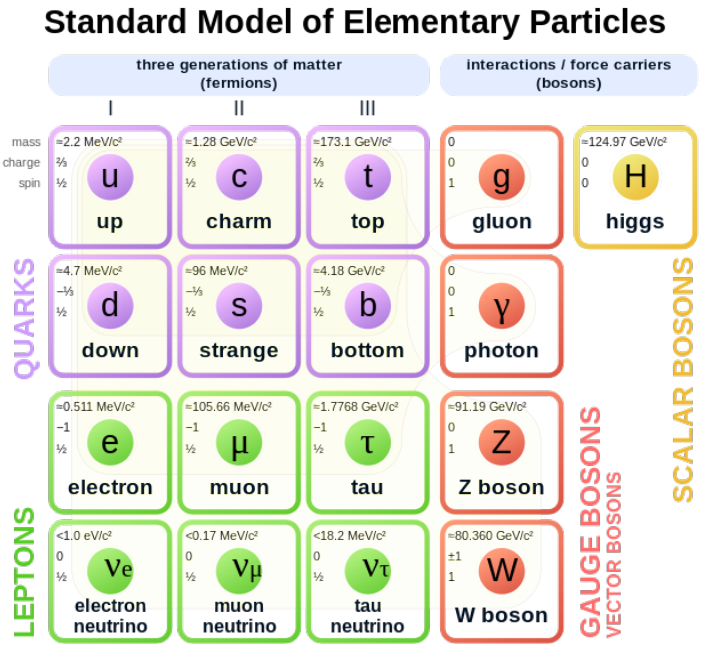


**Figure 1.1:** The particle content of the Standard Model. On the left side are the matter particles (fermions: quarks and leptons) divided in three generations. On the right side are the force carriers (bosons) [2].

Interactions between elementary particles are carried by bosons, each of them being responsible for one of the possible interactions. The weak, strong and electromagnetic interaction all originate from a local gauge symmetry: $\mathrm{SU(3)_C} \otimes \mathrm{SU(2)_L} \otimes \mathrm{U(1)_Y}$.

The strong interaction is mediated by gluons, $g$, and affects particles carrying a colour charge: quarks and gluons. It binds quarks together in more complex color-neutral particles, called hadrons. These can consist of a quark and an antiquark forming a meson, or of a triplet of quarks, forming a baryon.

The weak interaction is mediated by three heavy bosons: $W^+$, $W^-$, $Z^0$ and, due to the bosons large masses, at low energies is the weakest of these forces. It affects all Standard Model fermions and is the only interaction that can change the flavour of the particles and therefore is responsible for the $b \to sll$ decays, as will

be described in Section 1.2.

The electromagnetic interaction is mediated by photons, $\gamma$, and affects electrically charged particles.

The Higgs boson interacts with all fermions and all weak gauge bosons in the Standard Model, giving rise to their mass.

## 1.2 Rare $b \to sll$ decays

The focus of the research presented in this thesis is the transition $b \to sll$, in which a beauty quark $b$ decays to a strange quark $s$ and two leptons $l^+l^-$ of opposite charge, in particular an electron and a positron. This decay is represented by the Feynman diagram show in Figure 1.2.

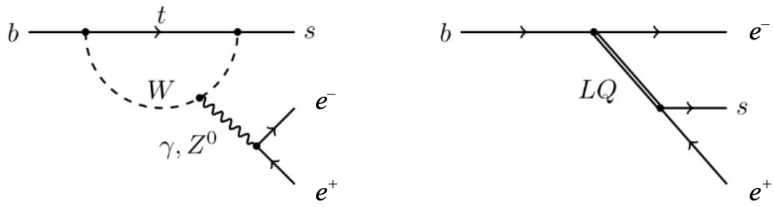


**Figure 1.2:** Feynman diagrams according to the Standard Model (*left*) and with hypothetical leptoquarks contributing to the decay (*right*).

The left diagram represents a change of the quark flavour, in which a beauty quark $b$ transitions into a strange quark $s$. This transition requires the presence of a Flavour Changing Neutral Current (FCNC), an interaction changing a flavour of a fermion without changing its charge [3]. In the SM, this interaction occurs only in loop-level processes, during which a virtual particle is temporarily created and annihilated, as can be seen with the top quark $t$ in Figure 1.2 (*left*). However, there might be processes that are not predicted by the Standard Model, with yet-undiscovered particles participating in the $b \to sll$ transition. An example of such a hypothetical scenario, with a leptoquark mediating the decay, is shown in Figure 1.2 (*right*).

Rare beauty decays are ideal tools to search for new physics effects like those shown in Figure 1.2 (*right*). In a loop-level process, since the particles transmitting the decay are virtual particles, their masses can be bigger than the initial and

final state particles, which opens a possibility of discovering especially heavy new particles. Moreover, in these decays, the values of the SM decay amplitudes are typically very small, which would make the presence of new physics contributions more pronounced.

To compute the decay amplitudes, the decay is described using effective low-energy theory. In such a description, the heavy degrees of freedom (top quark, $W$ boson, $Z$ boson) are integrated out and the interaction is reduced to an effective four-point interaction, with associated Wilson coefficients $C_i$ and operators $\mathcal{O}_i$. The amplitude associated with the $b \to sll$ decay is given by:

$$\mathcal{A}(b \to sll) = \langle sll|H_{\text{eff}}|b\rangle, \tag{1.1}$$

where $H_{\text{eff}}$ is the effective hamiltonian associated with the four-point interaction. For the $b \to sll$ transition it takes the form:

$$H_{\text{eff}} = -\frac{G_{\text{F}}\alpha}{\sqrt{2}\pi} V_{\text{ts}}^* V_{\text{tb}} \left[ \sum_{i=7,9,10,S,P} C_i^{(\prime)} \mathcal{O}_i^{(\prime)} \right], \tag{1.2}$$

where $G_{\text{F}}$ is the Fermi Constant, $\alpha$ is the fine structure constant, and $V_{\text{ts}}^*$ and $V_{\text{tb}}$ are the relevant CKM elements in the Standard Model [4].

The Wilson operators $\mathcal{O}_i$ encode long-distance non-perturbative effects [4]. The two sets, $\mathcal{O}_i$ and $\mathcal{O}_i'$, correspond to different chirality states, but the primed operators are either highly suppressed or vanish in the SM [5]. The Wilson coefficients $C_i$ describe the short-distance interaction and are calculated in perturbation theory, including higher order corrections. Due to the separation of scales, contributions from new heavy particles only affect the Wilson coefficients.

One of the decays used for these investigations is the $B \to K^* ll$ decay. Its rate depends on the invariant mass squared of the dilepton system, $q^2 = m_{ll}^2$. The invariant mass spectrum is schematically shown in Figure 1.3. As indicated, different regions of the spectrum are sensitive to different Wilson coefficients. A number of $q^2$ dependent observables can be constructed, such as differential branching ratios or angular coefficients, as will be described in Section 1.5. Including this dependence in the observables allows probing different Wilson coefficients depending on the $q^2$ interval.

The structure of the $q^2$ spectrum is caused by contributions from different decays with the same final state. Four components of the spectrum can be distinguished: the $B^0 \to K^{0*} l^+ l^-$ decays, the photon pole on the right and two resonant peaks of $J/\psi$ and $\psi(2S)$, corresponding to $B^0 \to K^{0*} J/\psi (\to l^+ l^-)$ and

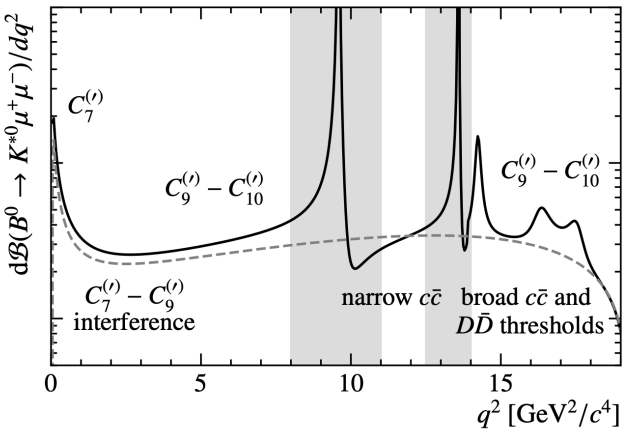


**Figure 1.3:** Schematic view of the $B^0 \to K^{0*}l^+l^-$ spectrum as a function of $q^2$, with the dominant Wilson coefficients displayed and possible $c\bar{c}$ contributions marked with grey bands. The dashed line corresponds to the pure rare semileptonic decay, while the solid line includes the impact of different charmonium resonances [6].

$B \to K^*\psi(2S)(\to l^+l^-)$ decays, respectively. In physics analyses, the search for physics beyond Standard Model is performed using the rare (non-resonant) decays, $B \to K^*ll$, while the resonant modes are used as control channels.

### 1.2.1 $B^0 \to K^{0*}J/\psi$ decay

The $B^0 \to K^{0*}J/\psi(\to e^+e^-)$ decay is used in the angular analysis of $B^0 \to K^{0*}e^+e^-$ decays as a control channel. The final state particles are the same in both cases, although the underlying decays are different: $b \to se^+e^-$ ($B^0 \to K^{0*}e^+e^-$ ) and $b \to c\bar{c}s$ ($B^0 \to K^{0*}J/\psi$ ), with the charmonium state $c\bar{c}$ decaying to an $e^+e^-$ pair. This means that the underlying physics of these decays will be different.

In the Standard Model, the $B^0 \to K^{0*}J/\psi$ decay is dominated by a colour-suppressed tree diagram, not involving FCNC, as shown in Figure 1.4 (*left*), with a highly suppressed contributions from loop diagrams Figure 1.4 (*right*). However, in case of a presence of physics beyond the SM, the loop contributions could be enhanced and introduce *CP*-violating differences between $B^0$ and $\bar{B}^0$ decays, not existing within the SM predictions.

These SM predictions were tested by several high energy physics experiments in the angular analyses of the $B^0 \to K^{0*}J/\psi$ decays, which will be summarized

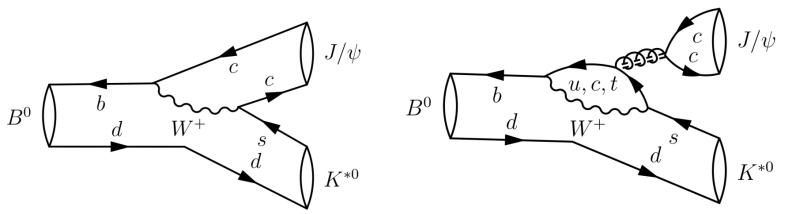


**Figure 1.4:** Tree (*left*) and loop (*right*) level Feynman diagram contributing to $B^0 \to K^{0*} J/\psi$ decay [7].

in Section 1.5. The results are consistent with each other and with the SM predictions [8]. Moreover, the SM does not predict a difference between the electron and muon final state in this decay, which has also been confirmed by other experiments [7]. This feature makes the $B^0 \to K^{0*} J/\psi$ decay suitable as a control channel. In this analysis, the comparison of the electron final state with the well understood muon final state is used to confirm obtained results.

## 1.3 Angular basis of the decay

In the angular analyses, new physics contributions are expected to be visible in the distributions of the decay angles $\vec{\Omega} = (\theta_l, \theta_K, \phi)$, schematically shown in Figure 1.5.

The angle $\theta_l$ is the angle between the direction of the $e^+$ ($e^-$) in the dielectron rest frame and the direction of the dielectron in the $B^0$ ($\bar{B}^0$) rest frame. The angle $\theta_K$ is the angle between the direction of the $K^0$ in the $K^{*0}$ ($\bar{K}^{*0}$) rest frame and the direction of the $K$ ($\bar{K}$) in the $B^0$ ($\bar{B}^0$) rest frame. The angle $\phi$ is the angle between the plane containing the $e^+$ and $e^-$ and the plane containing the $K$ and $\pi$ coming from the decay of $K^{*0}$.

The decay angles can be defined as scalar products of the momentum vectors of the final state particles:

$$\cos\theta_l = \left(\hat{p}_{e^+}^{(e^+e^-)}\right) \cdot \left(\hat{p}_{e^+e^-}^{(B^0)}\right) = \left(\hat{p}_{e^+}^{(e^+e^-)}\right) \cdot \left(-\hat{p}_{B^0}^{(e^+e^-)}\right), \tag{1.3}$$

$$\cos\theta_k = \left(\hat{p}_{K^+}^{(K^{*0})}\right) \cdot \left(\hat{p}_{K^{*0}}^{(B^0)}\right) = \left(\hat{p}_{K^+}^{(K^{*0})}\right) \cdot \left(-\hat{p}_{B^0}^{(K^{*0})}\right), \tag{1.4}$$

$$\cos\phi = \left(\hat{p}_{e^+}^{(B^0)} \times \hat{p}_{e^-}^{(B^0)}\right) \cdot \left(\hat{p}_{K^+}^{(B^0)} \times \hat{p}_{\pi^-}^{(B^0)}\right), \tag{1.5}$$

$$\sin\phi = \left[\left(\hat{p}_{e^+}^{(B^0)} \times \hat{p}_{e^-}^{(B^0)}\right) \times \left(\hat{p}_{K^+}^{(B^0)} \times \hat{p}_{\pi^-}^{(B^0)}\right)\right] \cdot \hat{p}_{K^{*0}}^{(B^0)}, \tag{1.6}$$

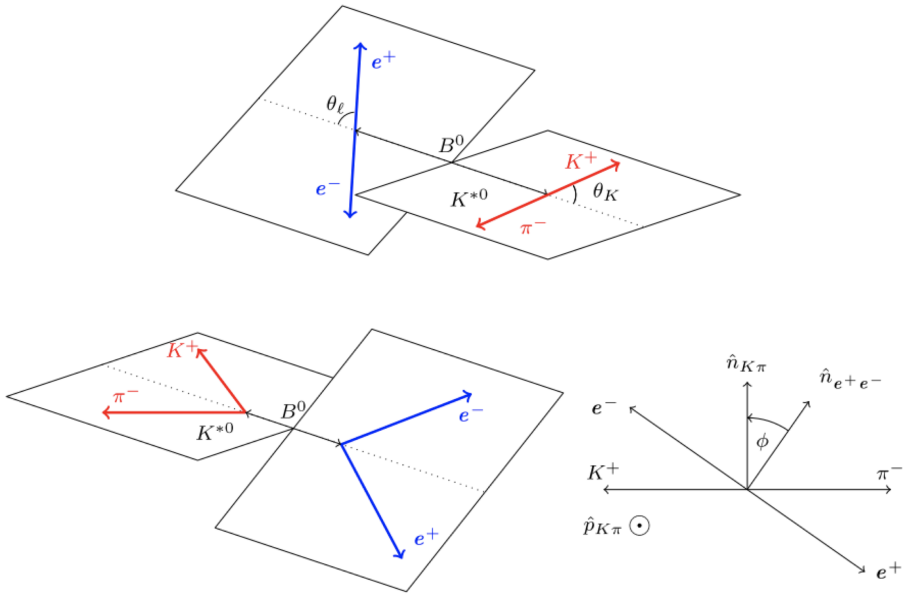


**Figure 1.5:** Schematic sketch of the $b \to sll$ decay geometry with the decay angles $\theta_l$, $\theta_K$, $\phi$ indicated. The vector labeled $B^0$ indicates the meson's flight direction.

where $\hat{p}_X^{(Y)}$ is the momentum of particle $X$ in the rest frame of particle $Y$ [9]. All particle momenta in Equations (1.3) – (1.6) are first boosted to the $B^0$ rest frame. The angles for the $\bar{B}^0$ decay are obtained from these by applying a *CP*-transformation and then using Equations (1.3) – (1.6) for the corresponding anti-particles.

## 1.4 Angular distributions

The observables measured in the angular analyses are derived from the differential decay rate. This is a function of the invariant mass of the dielectron pair, $q^2$, and three decay angles, $\vec{\Omega} = (\theta_l, \theta_K, \phi)$. It can be written as [10]:

$$\begin{aligned}\frac{\mathrm{d}^4\Gamma\left[\bar{B}^0 \to \bar{K}^{*0} ee\right]}{\mathrm{d}q^2 \mathrm{d}\vec{\Omega}} &= \frac{9}{32\pi}\sum_i^{12} I_i(q^2) f_i(\vec{\Omega}), \\ \frac{\mathrm{d}^4\Gamma\left[B^0 \to K^{*0} ee\right]}{\mathrm{d}q^2 \mathrm{d}\vec{\Omega}} &= \frac{9}{32\pi}\sum_i^{12} \bar{I}_i(q^2) f_i(\vec{\Omega}),\end{aligned} \tag{1.7}$$

where $I_i(q^2)$ are $q^2$-dependent angular coefficients, and $f_i(\vec{\Omega})$ are angular base functions depending on the angles.

The angular coefficients $I_i(q^2)$ can be expressed as bilinear combinations of six complex decay amplitudes $\mathcal{A}^{\mathrm{L,R}}_{0,\parallel,\perp}$, shown in Equations (1.8) – (1.10) [11]. These amplitudes correspond to different combinations of the transversity states of the $K^{*0}$ meson $(0, \parallel, \perp)$ and different (left- and right-handed) chiralities of the dielectron system. They are defined as follows:

$$\begin{aligned}\mathcal{A}^{\mathrm{L,R}}_{\perp} =& \mathcal{N}\sqrt{2\lambda}\left\{[(C_9^{\mathrm{eff}} + C_9^{\prime\mathrm{eff}}) \mp (C_{10}^{\mathrm{eff}} + C_{10}^{\prime\mathrm{eff}})]\frac{V(q^2)}{m_B + m_{K^*}}\right. \\ &\left. + \frac{2m_b}{q^2}(C_7^{\mathrm{eff}} + C_7^{\prime\mathrm{eff}})T_1(q^2)\right\},\end{aligned} \tag{1.8}$$

$$\begin{aligned}\mathcal{A}^{\mathrm{L,R}}_{\parallel} =& -\mathcal{N}\sqrt{2}(m_B^2 + m_{K^*}^2)\left\{[(C_9^{\mathrm{eff}} - C_9^{\prime\mathrm{eff}}) \mp (C_{10}^{\mathrm{eff}} - C_{10}^{\prime\mathrm{eff}})]\frac{A_1(q^2)}{m_B + m_{K^*}}\right. \\ &\left. + \frac{2m_b}{q^2}(C_7^{\mathrm{eff}} - C_7^{\prime\mathrm{eff}})T_2(q^2)\right\},\end{aligned} \tag{1.9}$$

$$\begin{aligned}\mathcal{A}^{\mathrm{L,R}}_{0} =& -\frac{\mathcal{N}}{2m_{K^*}\sqrt{q^2}}\left\{[(C_9^{\mathrm{eff}} - C_9^{\prime\mathrm{eff}}) \mp (C_{10}^{\mathrm{eff}} - C_{10}^{\prime\mathrm{eff}})]\right. \\ &\times [(m_B^2 - m_{K^*}^2 - q^2)(m_B^2 + m_{K^*}^2)A_1(q^2) - \lambda\frac{A_2(q^2)}{m_B + m_{K^*}}] \\ &\left. + 2m_b(C_7^{\mathrm{eff}} - C_7^{\prime\mathrm{eff}})[(m_B^2 + 3m_{K^*}^2 - q^2)T_2(q^2) - \frac{\lambda}{m_B^2 - m_{K^*}^2}T_3(q^2)]\right\},\end{aligned} \tag{1.10}$$

with left- and right-handed amplitudes (L,R) denoted by $\pm$. In these equations $\mathcal{N}$

denotes a normalization factor:

$$\mathcal{N} = V_{tb}V_{ts}^{*}\left[\frac{G_F^2\alpha_{\text{em}}^2}{3\cdot 2^{10}\pi^5 m_B^3}q^2\lambda^{1/2}\beta_l\right]^{1/2}, \tag{1.11}$$

where $\lambda \equiv m_B^4 + m_{K^*}^4 + q^4 - 2(m_B^2 m_{K^*}^2 + m_{K^*}^2 q^2 + m_B^2 q^2)$, $\beta_l \equiv \sqrt{1 - 4m_l^2/q^2} \approx 1$ in the case of massless leptons, and $V(q^2)$, $T_{1,2,3}(q^2)$, $A_{0,1,2}(q^2)$ are the $q^2$-dependent hadronic form factors [12, 13], reflecting the distribution of charge and current in the particles, and therefore their internal structure [14].

These six amplitudes correspond to P-wave contributions from the vector meson $K^{*0}$ decaying to the $K^+\pi^-$ system. However, the $K^+\pi^-$ final state can also be in an S-wave configuration, corresponding to the non-resonant decays or to decays of scalar resonances [15]. This introduces additional complex amplitudes $\mathcal{A}_{S0}^{\text{L,R}}$, given by:

$$\begin{aligned}\mathcal{A}_{S0}^{\text{L,R}} =& \mathcal{N}_0\sqrt{\frac{\lambda_{K_0^*}}{q^2}}\Big\{\left[(C_9 - C_9') \mp (C_{10} - C_{10}')\right] f_+\left(q^2\right) \\ &+ (C_7 - C_7')\, 2m_b \frac{f_T\left(q^2\right)}{m_B + m_{K_0^*}}\Big\},\end{aligned} \tag{1.12}$$

where $f_+$, $f_T$ and $f_0$ are $q^2$-dependent hadronic form factors.

Table 1.1 shows the list of the angular coefficients $I_i(q^2)$, their definitions in terms of the decay amplitudes and the corresponding angular functions, with $i \in (1s, 9)$ corresponding to P-wave, $i = 10, 17$ to S-wave contributions, and the remaining ones to the interference between the P-wave and the S-wave. Determining the angular coefficients in Equation (1.7) allows to obtain the decay amplitudes and therefore the Wilson coefficients.

In the literature, the angular coefficients $I_i$ are used to define $q^2$-dependent CP-averaged observables:

$$S_i = \left(I_i + \bar{I}_i\right) \Big/ \left(\frac{\mathrm{d}^4\Gamma}{\mathrm{d}q^2\mathrm{d}\vec{\Omega}} + \frac{\mathrm{d}^4\bar{\Gamma}}{\mathrm{d}q^2\mathrm{d}\vec{\Omega}}\right). \tag{1.13}$$

A number of known properties [15] are used to reduce the number of independent *CP*-averaged observables from twelve to nine, removing observables $S_{1s}$, $S_{2s}$ and $S_{2c}$. The $S_{1c}$ observable corresponds to the fraction of longitudinal polarisation of the $K^{*0}$ meson and is commonly referred to as $F_{\text{L}}$:

$$F_{\text{L}} = \frac{|\mathcal{A}_0^{\text{L}}|^2 + |\mathcal{A}_0^{\text{R}}|^2}{|\mathcal{A}_0^{\text{L}}|^2 + |\mathcal{A}_0^{\text{R}}|^2 + |\mathcal{A}_\perp^{\text{L}}|^2 + |\mathcal{A}_\perp^{\text{R}}|^2 + |\mathcal{A}_\parallel^{\text{L}}|^2 + |\mathcal{A}_\parallel^{\text{R}}|^2}. \tag{1.14}$$

| $i$ | Angular coefficient $I_i$ | Angular function $f_i(\vec{\Omega})$ |
|---|---|---|
| $1s$ | $\frac{3}{4}\left[\left\|\mathcal{A}_\parallel^{\mathrm{L}}\right\|^2+\left\|\mathcal{A}_\perp^{\mathrm{L}}\right\|^2+\left\|\mathcal{A}_\parallel^{\mathrm{R}}\right\|^2+\left\|\mathcal{A}_\perp^{\mathrm{R}}\right\|^2\right]$ | $\sin^2\theta_K$ |
| $1c$ | $\left\|\mathcal{A}_0^{\mathrm{L}}\right\|^2+\left\|\mathcal{A}_0^{\mathrm{R}}\right\|^2$ | $\cos^2\theta_K$ |
| $2s$ | $\frac{1}{4}\left[\left\|\mathcal{A}_\parallel^{\mathrm{L}}\right\|^2+\left\|\mathcal{A}_\perp^{\mathrm{L}}\right\|^2+\left\|\mathcal{A}_\parallel^{\mathrm{R}}\right\|^2+\left\|\mathcal{A}_\perp^{\mathrm{R}}\right\|^2\right]$ | $\sin^2\theta_K\cos 2\theta_l$ |
| $2c$ | $-\left\|\mathcal{A}_0^{\mathrm{L}}\right\|^2-\left\|\mathcal{A}_0^{\mathrm{R}}\right\|^2$ | $\cos^2\theta_K\cos 2\theta_l$ |
| $3$ | $\frac{1}{2}\left[\left\|\mathcal{A}_\perp^{\mathrm{L}}\right\|^2-\left\|\mathcal{A}_\parallel^{\mathrm{L}}\right\|^2+\left\|\mathcal{A}_\perp^{\mathrm{R}}\right\|^2-\left\|\mathcal{A}_\parallel^{\mathrm{R}}\right\|^2\right]$ | $\sin^2\theta_K\sin^2\theta_l\cos 2\phi$ |
| $4$ | $\sqrt{\frac{1}{2}}\,\mathrm{Re}\left(\mathcal{A}_0^{\mathrm{L}}\mathcal{A}_\parallel^{\mathrm{L}*}+\mathcal{A}_0^{\mathrm{R}}\mathcal{A}_\parallel^{\mathrm{R}*}\right)$ | $\sin 2\theta_K\sin 2\theta_l\cos\phi$ |
| $5$ | $\sqrt{2}\,\mathrm{Re}\left(\mathcal{A}_0^{\mathrm{L}}\mathcal{A}_\perp^{\mathrm{L}*}-\mathcal{A}_0^{\mathrm{R}}\mathcal{A}_\perp^{\mathrm{R}*}\right)$ | $\sin 2\theta_K\sin\theta_l\cos\phi$ |
| $6s$ | $2\,\mathrm{Re}\left(\mathcal{A}_\parallel^{\mathrm{L}}\mathcal{A}_\perp^{\mathrm{L}*}-\mathcal{A}_\parallel^{\mathrm{R}}\mathcal{A}_\perp^{\mathrm{R}*}\right)$ | $\sin^2\theta_K\cos\theta_l$ |
| $7$ | $\sqrt{2}\,\mathrm{Im}\left(\mathcal{A}_0^{\mathrm{L}}\mathcal{A}_\parallel^{\mathrm{L}*}-\mathcal{A}_0^{\mathrm{R}}\mathcal{A}_\parallel^{\mathrm{R}*}\right)$ | $\sin 2\theta_K\sin\theta_l\sin\phi$ |
| $8$ | $\sqrt{\frac{1}{2}}\,\mathrm{Im}\left(\mathcal{A}_0^{\mathrm{L}}\mathcal{A}_\perp^{\mathrm{L}*}+\mathcal{A}_0^{\mathrm{R}}\mathcal{A}_\perp^{\mathrm{R}*}\right)$ | $\sin 2\theta_K\sin 2\theta_l\sin\phi$ |
| $9$ | $\mathrm{Im}\left(\mathcal{A}_\parallel^{\mathrm{L}*}\mathcal{A}_\perp^{\mathrm{L}}+\mathcal{A}_\parallel^{\mathrm{R}*}\mathcal{A}_\perp^{\mathrm{R}}\right)$ | $\sin^2\theta_K\sin^2\theta_l\sin 2\phi$ |
| $10$ | $\frac{1}{3}\left[\left\|\mathcal{A}_{\mathrm{S}0}^{\mathrm{L}}\right\|^2+\left\|\mathcal{A}_{\mathrm{S}0}^{\mathrm{R}}\right\|^2\right]$ | $1$ |
| $11$ | $\sqrt{\frac{4}{3}}\,\mathrm{Re}\left(\mathcal{A}_{\mathrm{S}0}^{\mathrm{L}}\mathcal{A}_0^{\mathrm{L}*}+\mathcal{A}_{\mathrm{S}0}^{\mathrm{R}}\mathcal{A}_0^{\mathrm{R}*}\right)$ | $\cos\theta_K$ |
| $12$ | $-\frac{1}{3}\left[\left\|\mathcal{A}_{\mathrm{S}0}^{\mathrm{L}}\right\|^2+\left\|\mathcal{A}_{\mathrm{S}0}^{\mathrm{R}}\right\|^2\right]$ | $\cos 2\theta_l$ |
| $13$ | $-\sqrt{\frac{4}{3}}\,\mathrm{Re}\left(\mathcal{A}_{\mathrm{S}0}^{\mathrm{L}}\mathcal{A}_0^{\mathrm{L}*}+\mathcal{A}_{\mathrm{S}0}^{\mathrm{R}}\mathcal{A}_0^{\mathrm{R}*}\right)$ | $\cos\theta_K\cos 2\theta_l$ |
| $14$ | $\sqrt{\frac{2}{3}}\,\mathrm{Re}\left(\mathcal{A}_{\mathrm{S}0}^{\mathrm{L}}\mathcal{A}_\parallel^{\mathrm{L}*}+\mathcal{A}_{\mathrm{S}0}^{\mathrm{R}}\mathcal{A}_\parallel^{\mathrm{R}*}\right)$ | $\sin 2\theta_l\sin\theta_K\cos\phi$ |
| $15$ | $\sqrt{\frac{8}{3}}\,\mathrm{Re}\left(\mathcal{A}_{\mathrm{S}0}^{\mathrm{L}}\mathcal{A}_\perp^{\mathrm{L}*}-\mathcal{A}_{\mathrm{S}0}^{\mathrm{R}}\mathcal{A}_\perp^{\mathrm{R}*}\right)$ | $\sin\theta_l\sin\theta_K\cos\phi$ |
| $16$ | $\sqrt{\frac{8}{3}}\,\mathrm{Im}\left(\mathcal{A}_{\mathrm{S}0}^{\mathrm{L}}\mathcal{A}_\parallel^{\mathrm{L}*}-\mathcal{A}_{\mathrm{S}0}^{\mathrm{R}}\mathcal{A}_\parallel^{\mathrm{R}*}\right)$ | $\sin\theta_l\sin\theta_K\sin\phi$ |
| $17$ | $\sqrt{\frac{2}{3}}\,\mathrm{Im}\left(\mathcal{A}_{\mathrm{S}0}^{\mathrm{L}}\mathcal{A}_\perp^{\mathrm{L}*}+\mathcal{A}_{\mathrm{S}0}^{\mathrm{R}}\mathcal{A}_\perp^{\mathrm{R}*}\right)$ | $\sin 2\theta_l\sin\theta_K\sin\phi$ |

**Table 1.1:** Dependence of the angular observables $I_i(q^2)$ on the transversity amplitudes $\mathcal{A}_{0,\parallel,\perp}^{\mathrm{R,L}}$ and the corresponding angular functions $f_i(\vec{\Omega})$, with $i\in(1s,9)$ corresponding to P-wave, $i=10,17$ to S-wave contributions, and the remaining ones to the interference between the P-wave and the S-wave. The angular observables $\bar{I}_i(q^2)$ are given by complex conjugation of all weak phases $\mathcal{A}\to\vec{\mathcal{A}}$ [11].

It is also customary to replace $S_{6s}$ by the forward-backward asymmetry of the dilepton system, $A_{\mathrm{FB}}$, with $S_{6s}=\frac{4}{3}A_{\mathrm{FB}}$.

The *CP*-averaged angular distribution of the $B^0 \to K^{0*}e^+e^-$ decay can be written as:

$$\begin{aligned}\frac{1}{\mathrm{d}(\Gamma+\bar{\Gamma})/\mathrm{d}q^2}\frac{\mathrm{d}^4(\Gamma+\bar{\Gamma})}{\mathrm{d}q^2\mathrm{d}\vec{\Omega}} = \frac{9}{32\pi}\Big[&\frac{3}{4}(1-F_\mathrm{L})\sin^2\theta_K + F_\mathrm{L}\cos^2\theta_K \\ &+ \frac{1}{4}(1-F_\mathrm{L})\sin^2\theta_K\cos 2\theta_l \\ &- F_\mathrm{L}\cos^2\theta_K\cos 2\theta_l + S_3\sin^2\theta_K\sin^2\theta_l\cos 2\phi \\ &+ S_4\sin 2\theta_K\sin 2\theta_l\cos\phi + S_5\sin 2\theta_K\sin\theta_l\cos\phi \\ &+ \frac{4}{3}A_\mathrm{FB}\sin^2\theta_K\cos\theta_l + S_7\sin 2\theta_K\sin\theta_l\sin\phi \\ &+ S_8\sin 2\theta_K\sin 2\theta_l\sin\phi + S_9\sin^2\theta_K\sin^2\theta_l\sin 2\phi\Big].\end{aligned} \tag{1.15}$$

If in addition to the P-wave $K^{*0}$ contributions to the final state, the S-wave contribution is taken into account, the *CP*-averaged angular distribution is expressed as:

$$\begin{aligned}\frac{1}{\mathrm{d}(\Gamma+\bar{\Gamma})/\mathrm{d}q^2}\frac{\mathrm{d}^4(\Gamma+\bar{\Gamma})}{\mathrm{d}q^2\mathrm{d}\vec{\Omega}}\Big|_{\mathrm{S+P}} =&(1-F_\mathrm{S})\frac{1}{\mathrm{d}(\Gamma+\bar{\Gamma})/\mathrm{d}q^2}\frac{\mathrm{d}^4(\Gamma+\bar{\Gamma})/\mathrm{d}q^2}{\mathrm{d}q^2\mathrm{d}\vec{\Omega}}\Big|_\mathrm{P} \\ &+\frac{3}{16\pi}\Big[F_\mathrm{S}\sin^2\theta_l + S_{S1}\sin^2\theta_l\cos\theta_K \\ &\quad + S_{S2}\sin 2\theta_l\sin\theta_K\cos\phi \\ &\quad + S_{S3}\sin\theta_l\sin\theta_K\cos\phi \\ &\quad + S_{S4}\sin\theta_l\sin\theta_K\sin\phi \\ &\quad + S_{S5}\sin 2\theta_l\sin\theta_K\sin\phi\Big],\end{aligned} \tag{1.16}$$

where $F_\mathrm{S}$ defined as

$$F_\mathrm{S} = \frac{|\mathcal{A}_\mathrm{S}^\mathrm{L}|^2+|\mathcal{A}_\mathrm{S}^\mathrm{R}|^2}{|\mathcal{A}_0^\mathrm{L}|^2+|\mathcal{A}_0^\mathrm{R}|^2+|\mathcal{A}_\perp^\mathrm{L}|^2+|\mathcal{A}_\perp^\mathrm{R}|^2+|\mathcal{A}_\parallel^\mathrm{L}|^2+|\mathcal{A}_\parallel^\mathrm{R}|^2+|\mathcal{A}_\mathrm{S}^\mathrm{L}|^2+|\mathcal{A}_\mathrm{S}^2|^2}, \tag{1.17}$$

denotes the S-wave fraction and additional terms $S_{S1} - S_{S5}$ arise from the interference between the S- and P-wave amplitudes.

## 1.5 Flavour anomalies

Several physics analyses of the $b \to sll$ decays have been performed in search of physics beyond Standard Model. These analyses, in addition to angular analy-

ses, include also the measurements of differential branching fractions and Lepton Flavour Universality ratios. Some of these results, including the angular analyses of the $B^0 \to K^{0*} J/\psi$ decays, are summarized below.

### 1.5.1 Differential branching fractions

The branching fraction $\mathcal{B}$ refers to the fraction of all decays that result in a given final state. In addition, one can define a differential branching fraction $\mathrm{d}\mathcal{B}/\mathrm{d}q^2$ in order to study the dependence on $q^2$, which is highly sensitive to extensions of the SM [16].

The differential branching fraction results for $B^+ \to K^+\mu^+\mu^-$, $B^0 \to K^0\mu^+\mu^-$ and $B^+ \to K^{*+}\mu^+\mu^-$ decays are shown in Figure 1.6 with theoretical predictions superimposed [17, 18]. All three measurements are consistent with the Standard Model prediction, but the values in low and central $q^2$ regions are consistently lower than the theoretical predictions.

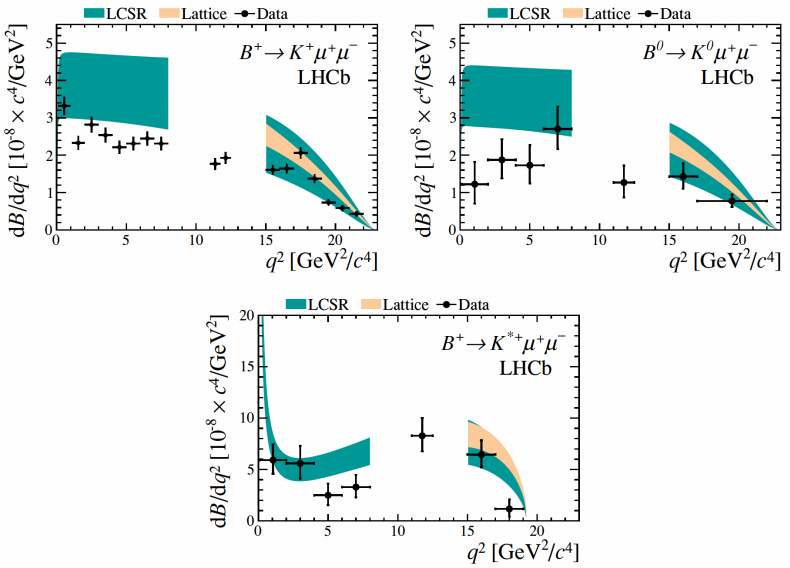


**Figure 1.6:** Differential branching fraction results for the $B^+ \to K^+\mu^+\mu^-$, $B^0 \to K^0\mu^+\mu^-$ and $B^+ \to K^{*+}\mu^+\mu^-$ decays. The uncertainties shown on the data points are the quadratic sum of the statistical and systematic uncertainties. The shaded regions illustrate theoretical predictions [17, 18] and their uncertainties obtained from light cone sum rule and lattice QCD calculations [16].

Although all three differential branching fraction measurements are consistent with the SM, they all have values consistently lower than the theoretical prediction. Similar results have been obtained by the BaBar [19] and Belle [20] experiments.

### 1.5.2 Lepton Flavour Universality studies

Lepton Flavour Universality (LFU) refers to the Standard Model feature that the gauge bosons have identical coupling to each of the lepton flavours and thus that differences between them are only dependent on the lepton mass. To test this feature, an observable called a LFU ratio $R$ is used. Rare $B^+ \to K^+ l^+ l^-$ and $B^0 \to K^{0*} l^+ l^-$ decays have been studied, where $l$ refers to muons and electrons, and their differential decay rates were used to construct the $R_K$ and $R_{K^*}$ observables:

$$R_{K,K^*}(q_a^2, q_b^2) = \frac{\int_{q_a^2}^{q_b^2} \mathrm{d}q^2 \, \frac{\mathrm{d}\Gamma(B^{(+,0)} \to K^{(+,*0)} \mu^+ \mu^-)}{\mathrm{d}q^2}}{\int_{q_a^2}^{q_b^2} \mathrm{d}q^2 \, \frac{\mathrm{d}\Gamma(B^{(+,0)} \to K^{(+,*0)} e^+ e^-)}{\mathrm{d}q^2}}, \tag{1.18}$$

where $q_a^2 < q^2 < q_b^2$ refers to $q^2$ intervals: $0.1 < q^2 < 1.1\,\mathrm{GeV}$ referred to as low $q^2$, and $1.1 < q^2 < 6.0\,\mathrm{GeV}$ referred to as central $q^2$.

Figure 1.7 and Table 1.2 show the results of the $R_K$ and $R_{K^*}$ measurements and the SM predictions in low and central $q^2$ bin. All four measurements are compatible with the Standard Model predictions, with the maximum discrepancy being around one standard deviation [21].

| Measurement | Standard Model | LHCb result |
|---|---|---|
| $R_K$ low $q^2$ | $0.9936 \pm 0.0003$ | $0.994\ ^{+0.090}_{-0.082}\ ^{+0.029}_{-0.027}$ |
| $R_K^*$ low $q^2$ | $1.0007 \pm 0.0003$ | $0.927\ ^{+0.093}_{-0.087}\ ^{+0.036}_{-0.035}$ |
| $R_K$ central $q^2$ | $0.9832 \pm 0.0014$ | $0.949\ ^{+0.042}_{-0.041}\ ^{+0.022}_{-0.022}$ |
| $R_K^*$ central $q^2$ | $0.9964 \pm 0.0006$ | $1.027\ ^{+0.072}_{-0.068}\ ^{+0.027}_{-0.026}$ |

**Table 1.2:** LFU ratios. In the LHCb measurement the first uncertainty is statistical, the second is systematical [21]. SM predictions and uncertainties from the `flavio` software package [22].

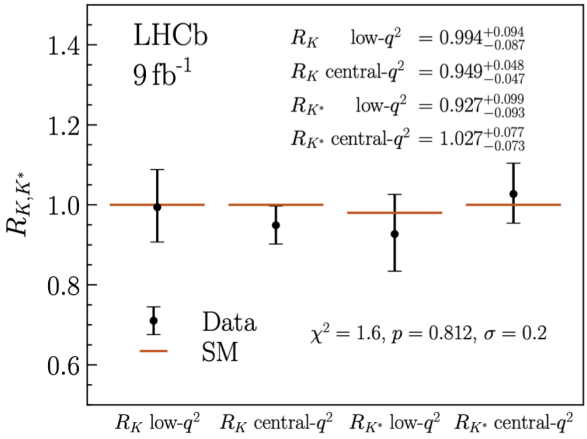


**Figure 1.7:** Measured values of LU observables in $B^+ \to K^+ l^+ l^-$ and $B^0 \to K^{0*} l^+ l^-$ decays and their overall compatibility with the SM [21].

### 1.5.3 Angular analyses

Several experiments have performed angular analyses of $B^0 \to K^{0*}\mu^+\mu^-$ decays, measuring the values of the angular coefficients. In addition to the observables mentioned in Section 1.4, an additional set of optimized angular observables $P_i^{(\prime)}$ has been used [23], defined as:

$$P'_{i=4,5,6,8} = \frac{S_{i=4,5,6,8}}{\sqrt{F_{\rm L}(1-F_{\rm L})}}, \tag{1.19}$$

and constructed in order to reduce the dependence on hadronic uncertainties. Results for the $P'_5$ observable have been obtained by the LHCb [24], ATLAS [25], CMS [26] and Belle [27] experiments and are shown in Figure 1.8 (*left*). Figure 1.8 (*right*) shows a comparison of the LHCb and Belle results separated for muons and electrons. All measurements are compatible within three standard deviations with the SM predictions, with the biggest tension observed in the $4.0 < q^2 < 8.0$ region.

In addition, a dependence on $\mathcal{R}e(C_9)$ was tested by performing a fit to the angular observables with the `flavio` software package [22]. Figure 1.9 shows the likelihood scan, exhibiting a minimum of the likelihood at $\Delta\mathcal{R}e(C_9) = -0.99^{+0.25}_{-0.21}$, 3.3 $\sigma$ away from the SM predictions [24].

Observed tensions in the $B^0 \to K^{0*}\mu^+\mu^-$ decay encourage a new physics search also in the electron channel, $B^0 \to K^{0*}e^+e^-$ . The research presented in this thesis contributes to this search.

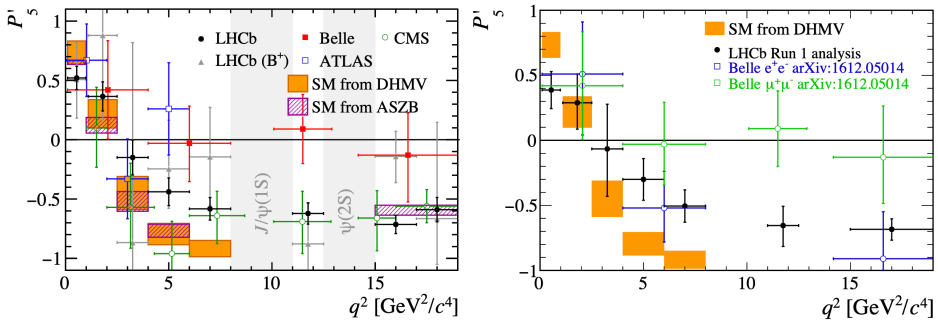


**Figure 1.8:** Results for the $P_5'$ observable for the $B^0 \to K^{0*}\mu^+\mu^-$ decays in bins of $q^2$ [24, 25, 26, 27] (*left*) and comparison of the LHCb and Belle results, with the latter separated for muons and electrons (*right*). The data are compared to SM predictions [13, 28, 29].

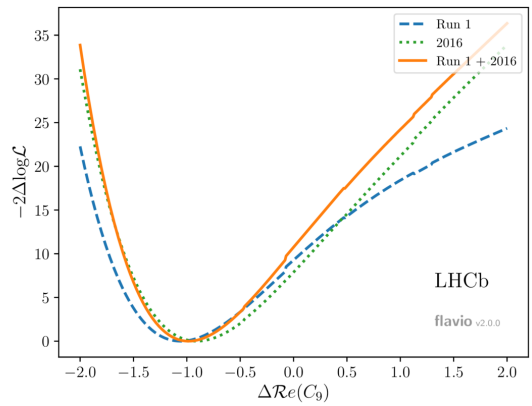


**Figure 1.9:** Likelihood scan of $\Delta\mathcal{R}e(C_9)$ with the `flavio` software package [22], using $B^0 \to K^{0*}\mu^+\mu^-$ data from Run 1, 2016 and both combined [24].

### $B^0 \to K^{0*} J/\psi$ decays

Angular analyses have also been performed in the $B^0 \to K^{0*} J/\psi(\to \mu^+\mu^-)$ channel, fitting directly the individual polarisation amplitudes: $\mathcal{A}_0$ , $\mathcal{A}_\perp$, $\mathcal{A}_\parallel$, $\mathcal{A}_S$, the first three referring to the P-wave contributions and the last one to the S-wave. These amplitudes are analogous to the decay amplitudes defined in Equation (1.9) – (1.10) and Equation (1.12).

Table 1.3 shows the comparison of the LHCb results assuming no S-wave component [7] with BaBar [30] and Belle [31] results. Since the amplitude values are correlated due to the constraint $|\mathcal{A}_0|^2+|\mathcal{A}_\perp|^2+|\mathcal{A}_\parallel|^2= 1$, only the values of $\mathcal{A}_\perp$ and $\mathcal{A}_\parallel$ are reported.

| param. | LHCb | BaBar | Belle |
|---|---|---|---|
| $\lvert\mathcal{A}_\parallel\rvert^2$ | $0.220 \pm 0.004 \pm 0.003$ | $0.211 \pm 0.010 \pm 0.006$ | $0.231 \pm 0.012 \pm 0.008$ |
| $\lvert\mathcal{A}_\perp\rvert^2$ | $0.210 \pm 0.004 \pm 0.004$ | $0.233 \pm 0.010 \pm 0.005$ | $0.195 \pm 0.012 \pm 0.008$ |
| $\delta_\parallel$ [rad] | $-2.98 \pm 0.03 \pm 0.01$ | $-2.93 \pm 0.08 \pm 0.04$ | $-2.887 \pm 0.090 \pm 0.008$ |
| $\delta_\perp$ [rad] | $2.97 \pm 0.02 \pm 0.02$ | $2.91 \pm 0.05 \pm 0.03$ | $2.938 \pm 0.064 \pm 0.010$ |

**Table 1.3:** Comparison of the results for the polarisation amplitudes $\mathcal{A}$ and their phases $\delta$ in the $B^0 \to K^{0*} J/\psi(\to \mu^+\mu^-)$ decay rate, obtained by LHCb with partial Run 1 data assuming no S-wave component [7], BaBar [30] and Belle [31]. The uncertainties are statistical and systematic, respectively. The values are negatively correlated due to the constrain $|\mathcal{A}_0|^2+|\mathcal{A}_\perp|^2+|\mathcal{A}_\parallel|^2= 1$.

The results are consistent with each other and this decay is expected to be a good control channel for searches of physics beyond the Standard Model.

# 2 | LHCb experiment

This dissertation presents an analysis performed using the data collected by the LHCb collaboration. The LHCb experiment is located at the Large Hadron Collider at CERN, the European Organization for Nuclear Research. The experiment is a combination of particle detectors forming a forward spectrometer, optimised for the detection of decays of charm and beauty quarks.

## 2.1 Large Hadron Collider

The Large Hadron Collider (LHC), is a 27 km long underground particle accelerator, located at CERN near Geneva, Switzerland. It has been designed to collide beams of protons at center of mass energy of 14 TeV.

A schematic drawing of the CERN Accelerator Complex is shown in Figure 1.1. Particles are accelerated to increasingly high energies in a chain of accelerators. The protons that are collided in the LHC, are created by stripping electrons from hydrogen gas and injected into the acceleration chain. First, protons are accelerated with a linear accelerator (LINAC) to 160 MeV and they are injected into proton synchrotron BOOSTER and accelerated to 2 GeV. Subsequently, they are injected into Proton Synchrotron (PS) and Super Proton Synchrotron (SPS), where they achieve energies of 26 GeV and 450 GeV, respectively. The 450 GeV protons are finally transferred to the LHC ring and are accelerated to their top energies, with 7 TeV per beam.

Once the protons reach LHC, they circulate in two beams in opposite directions. When they reach their top energy, the protons are brought into collision at rate of 40 MHz at the four LHC interaction points, around which four big LHC experiments are located: ATLAS, CMS, ALICE and LHCb. Each of these experiments collects

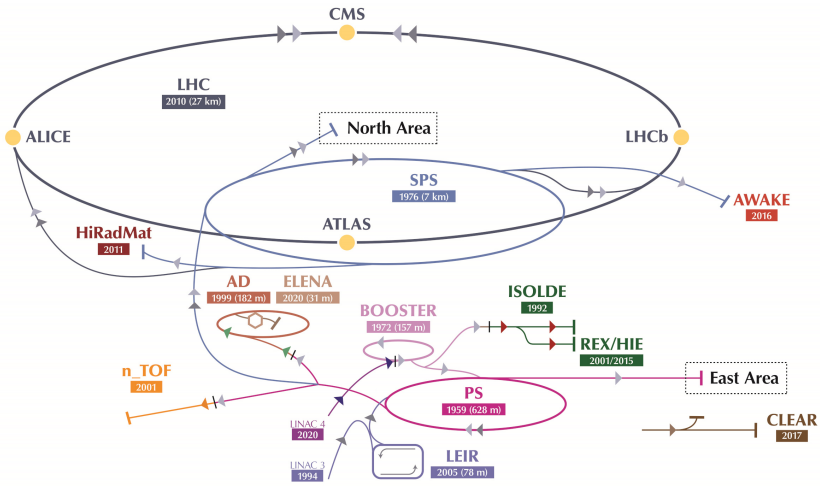


**Figure 2.1:** The accelerator complex at CERN, showing the chain of accelerators used to inject protons into the LHC ring [32].

data during 'LHC runs': data taking periods with specific accelerator and detector configurations. The analysis presented in this thesis uses data collected during two runs: Run 1 that took place from 2011 to 2012 and Run 2 from 2015 to 2018. After each run, a Long Shutdown of the LHC takes place, during which both the accelerator complex and the experiments undergo maintenance and upgrade. The Long Shutdown 2 (LS2) ended in 2022 after which the LHC experiments resumed data collection (Run 3).

During LS2, the LHCb experiment underwent a major upgrade [33]. However, the analysis described in this thesis was carried out with the data collected with the prior LHCb detector.

## 2.2 LHCb detector

The work presented in this thesis concerns analysis of data collected by the LHCb collaboration during LHC Run 1 and Run 2. The LHCb detector is a forward spectrometer designed to primarily study the decays of $b$ hadrons in search for asymmetries between matter and anti-matter. The LHCb physics program includes heavy ion study, $W$ and $Z$ boson production, and searches for new exotic particles. This thesis presents the study of rare $b$ hadron decays, as motivated in Chapter 1.

The design of the LHCb detector is motivated by the fact that $b$ hadrons and their decay products are mainly produced in the forward-backward region. The detector design covers pseudorapidity region $2 < \eta < 5$, with the pseudorapidity defined as $\eta \equiv -\ln\tan(\theta/2)$, where $\theta$ is the polar angle relative to the beam direction ($z$ axis). The layout of the LHCb detector is shown in Figure 2.2.

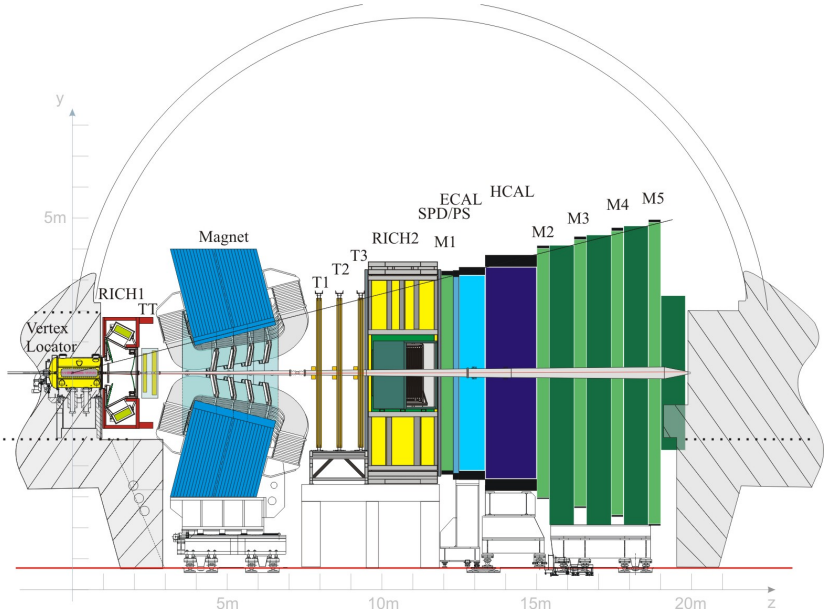


**Figure 2.2:** The layout of the LHCb detector before the LS2 upgrade [34].

The detector consists of several sub-detectors, contributing to the reconstruction of properties of the particles that are produced in the collision. These sub-detectors comprise larger systems with specific tasks. The particle tracking system consists of the Vertex Locator (Velo) and several tracking stations (TT, IT, OT). The particle identification system consists of Ring-imagining Cherenkov detectors (RICH1-2), the calorimeter system (SPD/PS, ECAL, HCAL) and the muons stations (M1-M5).

## 2.3 Particle Tracking

The particle tracking system is used for the reconstruction of the trajectories of the particles that were created in the $pp$ collisions. It consists of the Vertex Locator (Velo) and several tracking stations: Tracker Turicensis (TT), Inner Tracker

(IT) and Outer Tracker (OT). The latter two are usually referred to as T stations. A dipole magnet, located between TT and IT trackers, with an integrated field of 4 T m, deflects the particles resulting in curved trajectories. Combining the information in the tracking stations before and after the magnet allows for a precise reconstruction of the particle trajectories and the determination of their momenta. During data taking, the magnet polarity is periodically reversed in order to investigate and account for possible detector asymmetries.

Not every particle produced during the $pp$ collision will be registered by each of the tracking detectors, due to the geometrical acceptance and detector performance, such as the single hit efficiency. The probability to record a particle depends on its particle type and charge, momentum, flight direction, and lifetime. Based on the information in each of the detectors, independent track segments are created and used to reconstruct particle tracks. Firstly, Velo segments and T station segments are reconstructed. These segments are used to create long tracks, using two algorithms: forward tracking and track matching [35]. TT hits close to the resulting tracks are added afterwards. Finally, Velo and T-station segments that have not been used in longer tracks are independently added to the final track list as well. It is possible that tracks are reconstructed multiple times: these 'clones' are removed from the final track list.

As a results, there are five track categories, as indicated in the sketch in Figure 2.3:

— Long tracks traverse all the tracking detectors, which results in the most precise momentum determination. These are the most important tracks for most analyses, including the $B^0 \to K^{0*} e^+ e^-$ analysis.

— Downstream tracks traverse only TT and T stations. They are relevant for the detection of $K_S$ and $\Lambda$ decays.

— Upstream tracks traverse only Velo and TT stations, corresponding to low-momentum particles that are deflected out of the LHCb acceptance by the magnet.

— T tracks are the remaining T station segments. They are used to identify photons in the ECAL, acting as a veto for charged particles.

— Velo tracks are remaining Velo segments. These are included for primary vertex reconstruction.

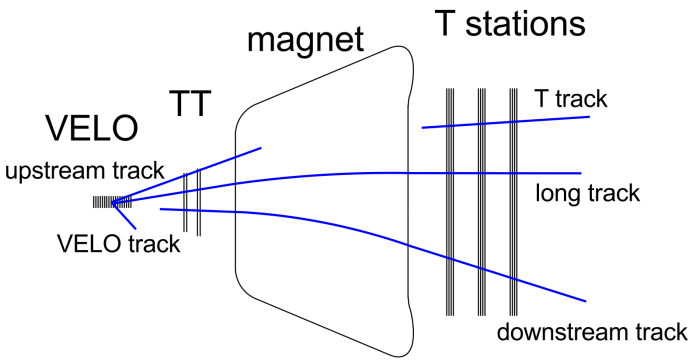


**Figure 2.3:** Track types in LHCb, with the definition of the tracks and the subsystem in which the tracks have hits. The magnetic field is oriented perpendicular to the tracks [35].

### 2.3.1 Vertex Locator

The Vertex Locator (Velo) is a silicon multistrip tracking detector surrounding the $pp$ interaction point. It registers charged particle trajectories near the primary vertex (PV), the interaction point where the particles are produced during the $pp$ collision. The data coming from the detector are used for track reconstruction and play a crucial role in the separation of the primary and decay vertices (points of decay of unstable particles). Impact parameter (IP) is the distance between a track and a vertex. Its good resolution is a key ingredient of the analyses of $b$ and $c$-hadron decays, as the reconstruction of their displaced decay vertices is crucial.

The Velo consists of 42 modules placed in two retractable detector halves around the beam axis. Each Velo module consists of two adjacent semicircular sensors, $r$ and $\phi$. The two types of sensors differ by the arrangement of the silicon strips, as shown in Figure 2.4, in order to measure the radial ($r$ sensor) and azimuthal coordinates ($\phi$ sensor). The relative position of the sensors in the station is indicated in Figure 2.5, where the solid lines stand for $r$ sensors, and dashed lines for $\phi$.

The modules are placed in two equal halves, arranged in a way that strikes balance between the gain in track reconstruction from a bigger number of stations, and the loss coming from multiple scattering introduced by adding material in the trajectories of the particles. The modules are located only 7 mm from the LHC beams, which is a smaller distance than that allowed during the injection of the beams into the LHC. During the beam injection and acceleration periods the two halves are retracted 3 cm away from the beam, as indicated in Figure 2.4 (*left*), and

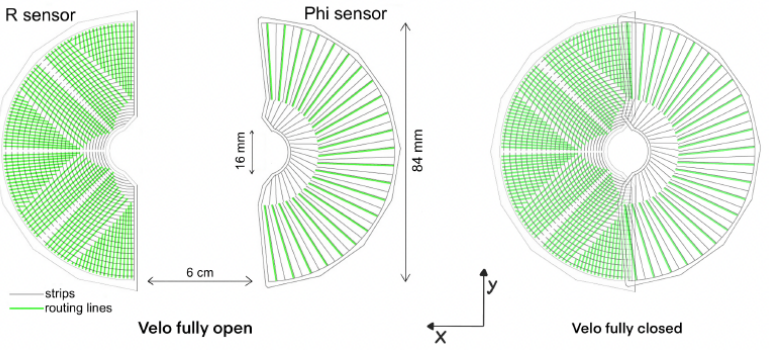


**Figure 2.4:** Representation of the front face of a Velo module in the open and close positions, with the different layout of the R and Φ sensors displayed. Reproduced from Ref. [36].

later closed for data taking, as shown in Figure 2.4 (*right*). Since the detector is located so close to the beam, each of the detector halves is located inside a custom aluminum RF foil, that separates the LHC beam vacuum from the vacuum created around the Velo sensors. The foils also protect the Velo sensors from the radio frequency radiation induced by the moving protons of the beams.

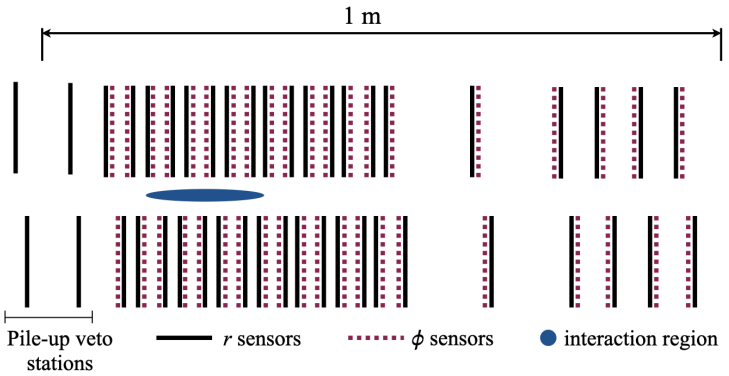


**Figure 2.5:** Cross section of the Velo in the $x$-$z$ plane. The $\phi$ and $r$ sensors are represented by dashed and solid lines, and the $pp$ interaction region is highlighted in blue. Reproduced from Ref. [36].

### 2.3.2 Tracking stations

The tracking stations in LHCb consist of three detectors: Tracker Turicensis (TT) located before the magnet (upstream) and Inner Tracker (IT) and Outer Tracker (OT), referred to collectively as T stations, located after the magnet (downstream). Their location on two sides of the magnetic field allows for the estimation of the momentum of charged particles from the tracks' curvature.

The two TT stations (TTa and TTb) are based on silicon microstrip sensors, located in four detection layers ($x-u-v-x$). The first and the last layer consist of vertical strips and the second and third of strips rotated by by $+5^\circ$ and $-5^\circ$, respectively, as shown in Figure 2.6.

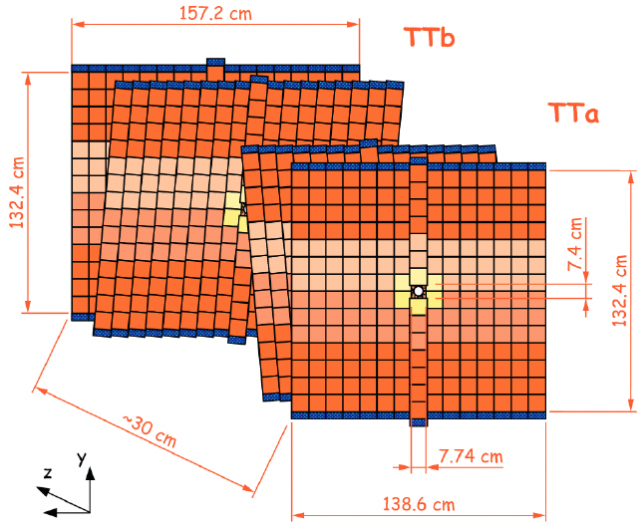


**Figure 2.6:** Schematic drawing of the TT layout, with the two $+5^\circ$ and $-5^\circ$ rotated layers [37].

The three T stations (T1, T2 and T3) are located downstream of the magnet and composed of both IT and OT modules. The IT modules are built with silicon microstrip sensors, and the OT modules with drift straw tubes filled with a mix of gasses. The sensors are arranged in four detection layers, as illustrated in Figure 2.7. The differences in their size and design are motivated by the differences in the multiplicity of particles.

Together, the tracking stations allows for a precise momentum and track reconstruction. The TT stations can be used to make an early estimation of the

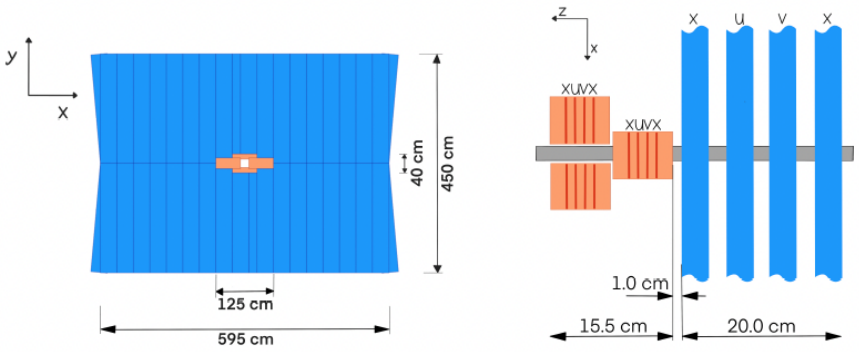


**Figure 2.7:** Front (left) and top (right) view of one of the T stations showing the IT and OT in orange and blue, respectively. The lateral dimensions in the top view are not on scale. Adapted from Ref. [38].

momentum, as they are placed close to the dipole magnet and the charged particles are only slightly affected by its field. The T stations located after the magnet provide the large sagittas necessary to determine even the smallest curves and thus provide a very precise momentum estimation.

## 2.4 Particle Identification

To be able to distinguish between particle species, the particle identification system (PID) is used. It is formed by three complementary detector sub-systems: Ring-imagining Cherenkov detectors, the calorimeter system and the muon stations. Each of the PID detectors interacts differently with electrons, photons, hadrons and muons and returns information used to create two types of PID variables. The first one, the combined differential log-likelihood (`DLL`) corresponds to the difference in log-likelihoods between two particle hypotheses. The second one, `ProbNN`, used multivariate techniques to combine tracking and PID information and provides a pseudo-probability of a particle track having a specific particle hypothesis. These variables are later used in the selection procedure in physics analyses.

### 2.4.1 Ring-imagining Cherenkov detectors

Ring-imagining Cherenkov (RICH) detectors make use of the Cherenkov radiation: when a particle traverses a medium with a speed larger than the speed of light in that medium, it emits photons in a form of a cone, with the angle of the cone depending on the velocity of the particle [39]. Using the particle momentum information provided by the tracking system, the mass of the particle can then be estimated. This is crucial to distinguish between different hadron types, such as pions, kaons and protons, which in turn is important for the signal and background distinction in the $B^0 \to K^{0*}e^+e^-$ analysis.

The LHCb PID system includes two RICH detectors, referred to as RICH1 and RICH2, located upstream and downstream of the magnet. To enable the Cherenkov radiation, the detectors are filled with a stable gas, $C_4F_{10}$ in case of RICH1 and $CF_4$ in case of RICH2. Photons created by the traversing particles are reflected by a set of mirrors and detected by hybrid photon detectors (HPDs). The cross-section of the RICH detector is shown in Figure 2.8 (*left*). The RICH1 detector is located between Velo and TT stations and is used to measure low particle momenta ($2-40\,\text{GeV}$), while RICH2 is located after the T stations and is used for high particle momenta ($15-100\,\text{GeV}$) measurement. Figure 2.8 (*right*) shows the reconstructed Cherenkov angle as a function of the track momentum for different particle types, used for particle identification.

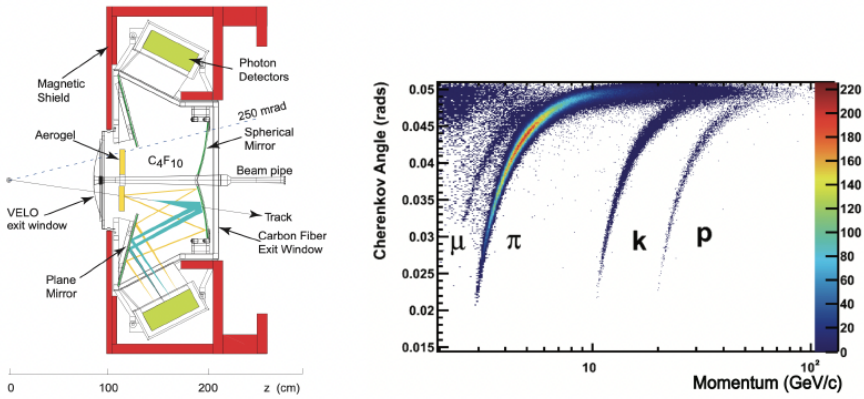


**Figure 2.8:** On the left, the schematic $x-y$ cross-section of RICH1 [34]. On the right, the reconstructed Cherenkov angle as a function of the track momentum for different particle types in the RICH1 [40].

### 2.4.2 Calorimeter System

The calorimeter system is used to distinguish between electrons, photons and hadrons, and to measure their energy. It is composed of several detectors located downstream of the magnet: the scintillator pad detector (SPD), preshower detector (PS), electromagnetic calorimeter (ECAL) and hadronic calorimeter (HCAL) [41]. Their response differs depending on the particle type, which allows for their distinction. The illustration of their response to different particle species is shown in Figure 2.9.

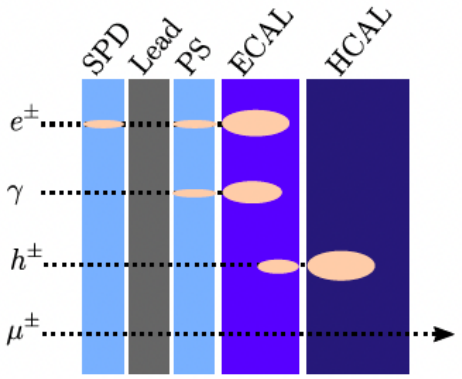


**Figure 2.9:** Interaction of electrons, photons, muons and hadrons with the different sub-detectors forming the calorimetry system: the scintillator pad detector (SPD), preshower detector (PS), electromagnetic calorimeter (ECAL) and hadronic calorimeter (HCAL) [42].

The scintillator pad detector (SPD) is used to separate charged and uncharged particles, such as photons and electrons, as it only interacts with the charged ones. It is followed by a 15 mm lead converter wall, placed there to induce an electromagnetic shower, and then by the preshower detector (PS), where the photons from the shower are registered. As only photons and electrons will induce this shower, this allows to distinguish them from hadrons.

The electromagnetic calorimeter (ECAL) measures the energy of electromagnetically interacting particles: photons and electrons. It consists of alternating layers of lead converter inducing an electromagnetic shower, and scintillator plate registering photons from the shower. The hadronic calorimeter (HCAL) provides an analogous function for hadrons. It consists of alternating layers of iron con-

verter and scintillator plate and measures a hadronic shower for the hadron energy measurement.

The way the electrons, photons and hadrons deposit energy in various sub-detectors of the calorimeter system is shown in Figure 2.9. These deposits are used to reconstruct the energy of the particles. The electromagnetic calorimeter also contributes to the bremsstrahlung recovery process, as will be described in Section 2.6.

### 2.4.3 Muon Stations

The muon system is composed of five stations, located at the outermost end of the LHCb detector. Muons and neutrinos are the only particles that reach this point; however, neutrinos only interact via the weak interaction (and thus very rarely) and therefore traverse the entire detector without leaving a signal. Muons reach this point, despite the fact that they interact electromagnetically, just like electrons; however, their mass is much higher than electrons' and their bremsstrahlung is negligible in comparison.

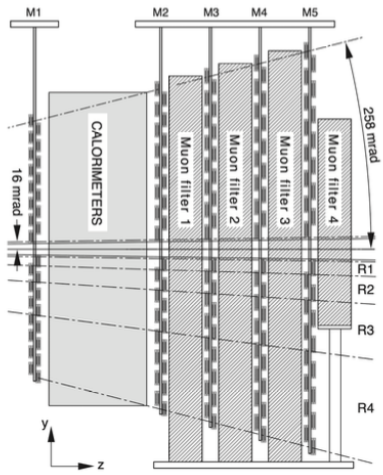


**Figure 2.10:** Side view of the muon stations with the four separated regions in each station [34].

The muon stations are located at the outermost end of the LHCb detector [34, 43], with the first one, M1, placed upstream of the calorimeter system, and the remaining four, M2-M5, downstream of the calorimeters, as indicated in

Figure 2.10. They are constructed using multi-wire proportional chambers and the stations M2-M5 are interleaved with iron absorbers. Station M1 is placed in front of the calorimeters in order to improve the precision of the transverse momentum measurement, together with the information from stations M2 and M3. Stations M4 and M5 are used mostly to detect penetrating muons, as only these will traverse multiple layers of muons stations and iron absorber.

## 2.5 Trigger System

During a $pp$ collision, with a bunch crossing rate about 40 MHz, a lot of data is produced, more than what LHCb can store. This issue is solved by the trigger system: a set of detector information and selection algorithms designed to select events relevant for physics analyses. The LHCb trigger system consists of two stages: the hardware trigger (level-zero trigger, L0) and the software trigger (high level trigger, HLT). It contains several groups of requirements, called 'trigger lines'.

The L0 trigger is based on the information from the calorimeter system and the muon stations and brings the rate of the events of interests down to 1 MHz, sufficiently low to allow the readout of the sub-detectors. The calorimeter system is used to estimate the energy deposited by the particles and a requirement is set on the minimum $E_{\mathrm{T}}$ and the maximum number of SPD hits. These requirements are used to build the following trigger lines: L0Electron, L0Photon and L0Hadron. Analogously for muons, a requirement on transverse momentum of one or two muon candidates is set, giving rise to the L0Muon and L0DiMuon trigger lines.

The information passing the L0 trigger requirements reaches the HLT trigger, where it is further processed. HLT consists of two levels: HLT1 and HLT2. The HLT1 trigger uses the information from the tracking stations and performs a partial event reconstruction. It selects events with high momentum and transverse momentum, as these events are connected to $b$-hadron decays, reducing the rate to 110 kHz. The full event reconstruction takes place at the HLT2 level, where requirements on PID and other relevant variables are applied, reducing the rate to about 12.5 kHz, sufficiently low for data storage.

An event has to be accepted by at least one trigger line in order to be stored for further analysis. The trigger requirements used in the $B^0 \to K^{0*}e^+e^-$ and $B^0 \to K^{0*}J/\psi$ analyses are described in Section 3.1.1.

## 2.6 Electrons in LHCb

While passing through the detector, electrons and muons give rise to very different detector response which impacts their reconstruction. Muons being much heavier than electrons, will not emit significant amount of bremsstrahlung or leave a noticeable energy deposit in the calorimeter. In contrast, electrons will emit bremsstrahlung photons as they traverse the LHCb detector. The differences in the detector response to muons and electrons are illustrated in Figure 2.11, including bremsstrahlung emission.

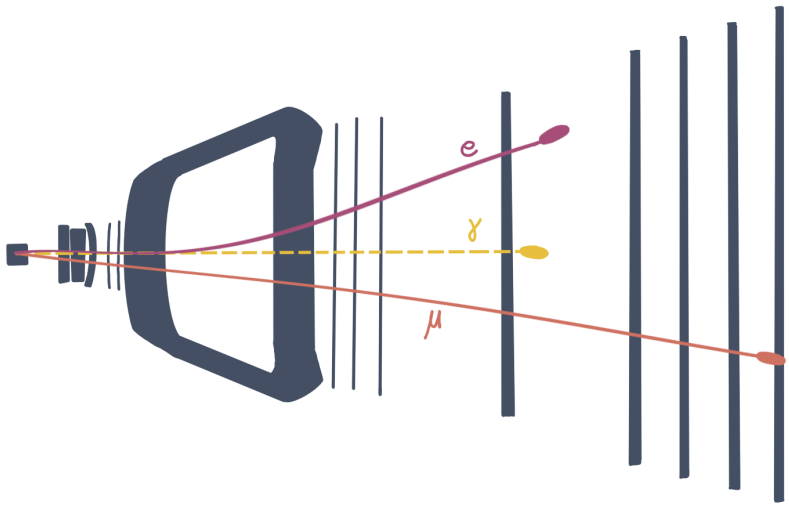


**Figure 2.11:** Illustration of the difference in detector response to muons (orange) and electrons (pink), together with the calorimeter response, including the bremsstrahlung emission.

The impact on the reconstruction depends on the place in the detector where the bremsstrahlung emission occurred. In LHCb, an electron coming from the interaction point will first pass the detectors upstream of the dipole magnet, then the magnet itself (where its trajectory will be curved), and finally the detectors downstream of the magnet, up to the electromagnetic calorimeter. If the electron emits bremsstrahlung *after* it passes the magnet, the trajectories of the photon and of the electron will be quite close to each other and there is a high probability that they will end up in the same calorimeter cluster. However, if the electrons emit bremsstrahlung *before* they reach the magnet, the electron's trajectories will

get curved but the photon's will not. As a result, they will create two separate calorimeter clusters and the electron momentum is evaluated after bremsstrahlung emission. This results in a degradation of the momentum resolution [44].

In order to improve the electron momentum reconstruction, a dedicated bremsstrahlung recovery process is applied [45]. For each electron track, the track segment upstream of the magnet is extrapolated to the calorimeter region and a search is performed for an energy deposit that is larger than 75 MeV and not associated with a charged track. In the case of $B^0 \to K^{0*} J/\psi(\to e^+e^-)$ decays, one bremsstrahlung cluster is added to either of the electrons in case of about half the events, two clusters are added for a quarter of the events and the remaining quarter does not have a bremsstrahlung cluster added. These three event categories will be later referred to as `Brem0`, `Brem1` and `Brem2`.

Moreover, the amount of signal registered for electrons is lower comparing to muons. This is due to the amount of background: electrons in ECAL have much more background from hadrons and photons, than muons have in the MUON system. Therefore a higher $p_T$ thresholds are set resulting in a lower registered signal.

These problems can be illustrated by comparing the distributions of the invariant mass of $B^0$ candidate coming from previous rare-decay analysis of $B^0 \to K^{0*}e^+e^-$ decay and $B^0 \to K^{0*}\mu^+\mu^-$ decays, shown in Figure 2.12.

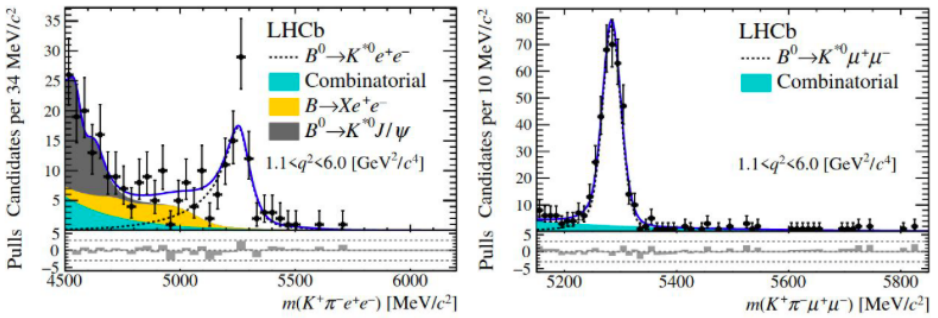


**Figure 2.12:** Invariant mass distribution of the $B^0$ candidates in the $B^0 \to K^{0*}e^+e^-$ decay (*left*) and $B^0 \to K^{0*}J/\psi(\to e^+e^-)$ decay (*right*) [44].

This comparison shows the significant differences between the electron and the muon final state channels: lower efficiency, worse resolution and higher amount of background.

# 3 | Data samples and selection

The angular analysis presented in this thesis concerns the four body decay $B^0 \to K^{0*} J/\psi$ , schematically shown in Figure 1.4. There are four final state particles: a kaon, a pion (the decay products of $K^*$) and two electrons with opposite charges (the decay products of the $J/\psi$).

The $B^0$ decay is reconstructed from the tracks of the final state particles that are registered by the LHCb detector, using RICH, ECAL and the tracking stations described in detail in Chapter 2. All $B^0$ candidates are reconstructed by combining four tracks in the event. However, the information obtained from the detector itself contains background in addition to the decay of interest. In order to reject the very large background, a series of selection criteria is applied, explained in detail in Section 3.1.

Applying this selection to simulation and to experimental data provides a dataset used for further analysis. This analysis is performed on the full available data set collected by LHCb during data-taking campaigns referred to as LHC Run 1 (data taking in years 2011-2012) and Run 2 (data taking in years 2015-2018). For each of the datasets, a corresponding simulated dataset was generated. These simulations are used to evaluate the detection efficiencies, the size of various background contributions and to validate the fit procedure. The details of all the recorded data samples and simulated samples used in this analysis are described in Section 3.2.

## 3.1 Candidate selection

The candidate selection procedure can be divided in two categories: online and offline selection. The online selection is used to select events in real time, with the use of the trigger system. All other steps are part of the offline selection, with the purpose of extracting a clear signal.

### 3.1.1 Trigger selection

The trigger system is used in real time during data taking in order to determine whether the candidate event should be further processed or rejected, as introduced in Section 2.5. Later, during the offline selection, exclusive $B^0$ candidates are reconstructed (see Section 3.1.2) and divided into two trigger categories, in order to allow a study of the trigger efficiency. The first of these two categories is Triggered-On-Signal (`TOS`), i.e. events triggered by at least one of the particles in the signal candidate and not triggered by particles that are not in the signal candidate. The second category is Triggered-Independently-of-Signal (`TIS`), referring to events triggered by particles that are not in the signal candidate.

There are several trigger lines used in this analysis, as summarized in Table 3.1. In most of the used trigger lines candidates are required to be `TOS`, unless explicitly stated otherwise.

| Run 1 | Run 2 |
|---|---|
| `L0Electron` | |
| `L0Hadron(TIS)` \| `L0Muon(TIS)` \| `L0Electron(TIS)` | |
| `Hlt1TrackAllL0` | `Hlt1TrackMVA` |
| | `Hlt1TwoTrackMVA` |
| `Hlt2Topo(E)[2,4]BodyBBDT` | `Hlt2Topo(E)[2,4]Body` |

**Table 3.1:** Summary of the trigger requirements for the offline candidate. All trigger lines are required to be TOS, unless stated otherwise.

At the hardware trigger level `L0`, two independent trigger categories are used, referred to as `L0I` and `L0E`. The `L0I` trigger is a combination of several lines, namely `L0Hadron(TIS)`, `L0Muon(TIS)` and `L0Electron(TIS)`, all of them being Triggered-Independently-of-Signal. The `L0E` trigger refers to events triggered by at least one of the electrons in the signal candidate (`TOS`).

At the HLT1 level, events are selected by the `Hlt1TrackAllL0` line for Run 1 and by the `Hlt1TrackMVA` or `Hlt1TwoTrackMVA` for Run 2. The `Hlt1TrackAllL0` and `Hlt1TrackMVA` lines select events in a three-stage process, selecting displaced tracks, performing a partial track reconstruction in order to select tracks with high momenta, and finally performing a fit to track parameters to select tracks with good enough track quality. The `Hlt1TwoTrackMVA` line selects events using a multivariate algorithm that identifies two-track displaced vertices with a large sum of the transverse momenta of the associated charged particles.

In the last stage, at the HLT2 level, the low data rate allows for a more complete track reconstruction. The trigger lines then choose tracks that have a topology that resembles a two- or three-track $b$ hadron decay, with displaced vertices and high $p_{\mathrm{T}}$.

A more detailed description of the LHCb trigger lines is given in Ref. [46].

### 3.1.2 Offline selection

The events that pass the trigger selection are subjected to the offline selection, performed in two stages. First a loose selection is applied, called *stripping*, in order to decrease the size of the sample and save only the events that are relevant to a particular analysis. During the stripping process, the particle candidates are reconstructed.

The $K^{*0}$ candidates are formed by combining all well-identified pions and kaons, with requirements set on the candidate mass and the quality of the reconstructed vertex. Di-electron candidates, $e^+e^-$, are formed by combining pairs of opposite sign electrons, corrected for bremsstrahlung emission (see Section 2.6). Finally, $B^0$ candidates are created by combining the $K^{*0}$ and $e^+e^-$ candidates. In each event, multiple $B^0$ candidates are created and these are all considered in the following selection. A summary of the requirements of the `Bu2LLKeeLine2` stripping line used in this analysis is shown in Table 3.2.

Subsequently, a series of pre-selection cuts is applied to ensure good track quality, proper particle identification and to reduce the level of the background. In addition, a boosted decision tree (BDT) is used to classify the contribution of the combinatorial background. The summary of the offline selection requirements discussed in this section is presented in Table 3.3.

A series of requirements was set on particle identification. The invariant mass reconstructed from a kaon and a pion, $m_{K\pi}$, is required to be within $100\,\mathrm{MeV}/c^2$ from the known mass of $K^{0*}(\to K\pi)$. All particles are required to have clusters

| | Requirement |
|---|---|
| Event | $N_{PV} \geq 1$ |
| | $n_{\mathrm{SPD}} \leq 600$ |
| $B^0$ | $\lvert m - m_{B^0}^{\mathrm{PDG}} \rvert < 1000\,\mathrm{MeV/c^2}$ |
| | `DIRA` $> 0.9995$ |
| | $\chi^2_{\mathrm{IP}}$ (primary) $< 25$ |
| | $\chi^2_{\mathrm{vertex}}/\mathrm{ndf} < 9$ |
| $K^{*0}$ | PV $\chi^2$ separation $> 100$ |
| | $\lvert m - m_{K^{*0}}^{\mathrm{PDG}} \rvert < 300\,\mathrm{MeV/c^2}$ |
| | $p_{\mathrm{T}} > 500\,\mathrm{MeV/c}$ |
| | $\chi^2_{\mathrm{vertex}}/\mathrm{ndf} < 25$ |
| $K^0$ | $\mathrm{DLL}_{K\pi} > -5$ |
| | $\chi^2_{\mathrm{IP}}$ (primary) $< 9$ |
| $\pi$ | $\chi^2_{\mathrm{IP}}$ (primary) $< 9$ |
| $e^+e^-$ | $m < 5500\,\mathrm{MeV/c^2}$ |
| | $\chi^2_{\mathrm{vertex}}/\mathrm{ndf} < 9$ |
| | PV $\chi^2$ separation $> 16$ |
| $e$ | $\mathrm{DLL}_{e\pi} > 0$ |
| | $p_{\mathrm{T}} > 300\,\mathrm{MeV/c}$ |
| | $\chi^2_{\mathrm{IP}}$ (primary) $< 9$ |

**Table 3.2:** Summary of the requirements of the `Bu2LLKeeLine2` stripping.

associated with them in the RICH detector and also – in case of electrons – in the ECAL.

There are also requirements set on the PID variables introduced in Section 2.4. Each registered particle has an assigned probability of being of a certain type, `ProbNN`. Particle candidates that do not have a high enough probability of being of a certain type, are rejected. In addition, the `DLL` variable is used, differentiating between two particle hypotheses (for instance, to distinguish electrons from pions). The distribution of `DLL` takes mostly positive values for electrons, and negative for pions.

The transverse momentum of a particle, $p_{\mathrm{T}}$, is another of the variables that have been used. A $p_{\mathrm{T}} > 250\,\mathrm{MeV}/c$ threshold is applied to kaons and pions, and $p_{\mathrm{T}} > 500\,\mathrm{MeV}/c$ to electrons, with an additional requirement $p > 3000\,\mathrm{MeV}/c$.

| Type | | Requirement |
|---|---|---|
| Quality | all tracks | $\chi^2/\text{ndf} < 3$ |
| | | $\texttt{GhostProb} < 0.4$ |
| | $e$ | $\texttt{region}^{\texttt{L0Calo}}_{\text{ECAL}} \geq 0$ |
| | | $!(\lvert\texttt{xProjection}^{\texttt{L0Calo}}_{\text{ECAL}}\rvert < 363.6\,\text{mm}$ |
| | | $\&\ \lvert\texttt{yProjection}^{\texttt{L0Calo}}_{\text{ECAL}}\rvert < 282.6\,\text{mm})$ |
| | | $\texttt{InAccEcal}$ |
| | | $\sqrt{p^2_{x,track} + p^2_{y,track}} > 200$ |
| Clone | $K, \pi, e$ | $\theta(\pi, e) > 0.0005,\ \theta(K, e) > 0.0005,\ \theta(K, \pi) > 0.0005$ |
| ID | $K^{*0}$ | $\lvert m(K\pi) - m^{PDG}_{K^{*0}}\rvert < 100\,\text{MeV}/c^2$ |
| PID | all | $\texttt{hasRich}$ |
| | $e$ | $\texttt{hasCalo}$ |
| | $K, \pi$ | $p_{\text{T}} > 250\,\text{MeV}/c$ |
| | $e$ | $p_{\text{T}} > 500\,\text{MeV}/c\ ,\ p > 3000\,\text{MeV}/c$ |
| | $K$ | $\texttt{ProbNNk} \cdot (1 - \texttt{ProbNNp}) > 0.05$ |
| | $\pi$ | $\texttt{V2ProbNNpi} \cdot (1 - \texttt{ProbNNk}) \cdot (1 - \texttt{ProbNNp}) > 0.1$ |
| | $e$ | $\texttt{ProbNNe} > 0.2$ |
| | $K$ | $\texttt{DLL}_{K\pi} > 0$ |
| | $e$ | $\texttt{DLL}_{e\pi} > 2$ |
| BKG | charmonium $e - h$ swap | $!(\lvert m_{J\psi,\psi(2S)cons.}(K_{\to e}\pi e_{\to K}e) - m^{PDG}(B^0)\rvert < 60\ \&\ \texttt{eProbNNe<0.8}$ |
| | | $\lvert\rvert\ \lvert m_{J\psi,\psi(2S)cons.}(K\pi_{\to e}ee_{\to\pi}) - m^{PDG}(B^0)\rvert < 60\ \&\ \texttt{eProbNNe<0.8})$ |
| | $B^+ \to K^+e^+e^-$ | $\max(m(Ke^+e^-), m(\pi_{\to K}e^+e^-)) < 5100\,\text{MeV}/c^2$ |
| | $B^0_s \to \phi e^+e^-$ | $!(m(K(\pi_{\to K})) < 1040\,\text{MeV}/c^2\ \&\ \pi\texttt{ProbNN}\pi < 0.8)$ |
| | $B^0 \to \bar{D}^0(\to K^+\pi^-)\pi^-e^+\nu_e$ | $!(\lvert m(Ke_{\to\pi}) - m^{PDG}(D^0)\rvert < 30\text{MeV}\ \&\ \texttt{eProbNNe} < 0.8)$ |
| | $B^0 \to D^-(\to K^{*0}(\to K^+\pi^-)\pi^-)e^+\nu_e$ | $!(\lvert m(K\pi e_{\to\pi}) - m^{PDG}(D^-)\rvert < 30\text{MeV}\ \&\ \texttt{eProbNNe} < 0.8)$ |
| | K $-\ \pi$ swap | $K\,\texttt{DLL}_{K\pi} - \pi\,\texttt{DLL}_{K\pi} > 0$ |
| | part-reco ($J/\psi$ only) | $m(K\pi e^+e^-)_{J/\psi} > 5150\,\text{MeV}/c^2$ |
| | comb | $\texttt{MVA} > 0.99$ |

**Table 3.3:** Summary of the offline selection requirements.

This selects candidates that have a higher chance of coming from a $B^0$ decay and ensures that the momentum range is good enough to be used by the tools computing the efficiency of particle identification.

In order to ensure that the reconstruction algorithm did not reconstruct as two separate tracks one track coming from the same particle, a rejection algorithm is used and an additional cut is applied on the angle between two tracks in the final state: if it is too close to zero (less than 0.5 mrad), the candidate is rejected.

Finally, a series of requirements was applied in order to reject specific background sources. Following previous analyses of $B^0 \to K^{*0}e^+e^-$ and the analyses of $B^0 \to K^{*0}\mu^+\mu^-$ , several backgrounds were considered for the control channel: combinatorial background, partially reconstructed $B$ decays, double semi-leptonic decays (DSL), and misidentified $\Lambda_b \to pKJ/\psi(\to e^+e^-)$ and $B^0_s \to \phi e^+e^-$ de-

cays. Figure 3.1 schematically shows all these backgrounds as they appear in the invariant mass distribution of the $B^0$ candidate in the $B^0 \to K^{0*} J/\psi$ decay.

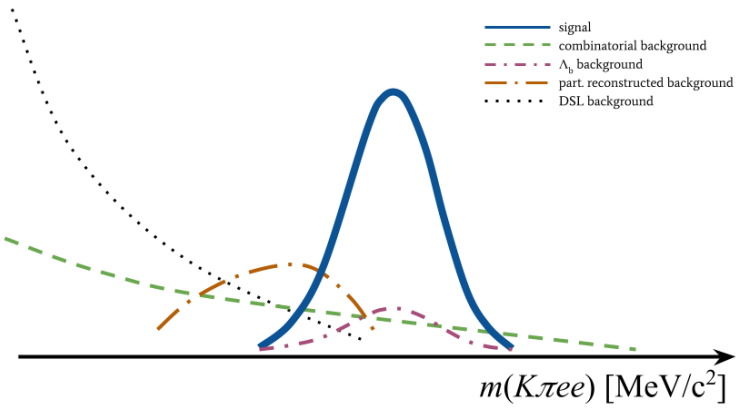


**Figure 3.1:** Schematic distribution of the backgrounds present in the $B^0 \to K^{0*} J/\psi$ invariant mass spectrum.

**Combinatorial background** appears when a $B^0$ candidate is reconstructed from tracks coming from two different decays or from the primary vertex. A substantial amount of it is removed on the base of a BDT classifier, and the remainder is modeled in the fit.

**Partially reconstructed background** comes from other $B^0$ decays, in which one of the final state particles has not been accounted for: a five-body decay was mistaken for a four-body one. An example of such a case can be a $B^+ \to K^+\pi^+\pi^- J/\psi$ decay, in which one of the pions is not used during the reconstruction and the final particles are $K^+\pi^- J/\psi$, just like in the $B^0 \to K^{0*} J/\psi$ signal. This background is removed by using the PV- and $J/\psi$-constrained invariant $B$ mass and requiring it to be higher than $5150\,\mathrm{MeV}/c^2$. The effect of this cut (part-reco) is shown in Figure 3.2, where different resonances show up as bands in the $m(B)$–$m(J/\psi)$ plane: $B \to K^* J/\psi$, $B \to K^* \psi(2S)$, $B^+ \to K^* J/\psi X$ and $B^+ \to K^* \psi(2S) X$, where $X$ stands for the missing particle.

**Double semi-leptonic background** (DSL) consists of $B^0 \to D^- X$ decays, that have the same visible decay products as the signal state. It is removed by a number of vetos, shown in Table 3.3. However, it was observed that the presence of these cuts have an effect on the distribution of one of the angular observables, $\cos\theta_l$, causing a step in the distribution around $\cos\theta_l = \pm 0.8$, that can be seen later in $\cos\theta_l$ distributions in Figure 4.3. In future studies an alternative selection

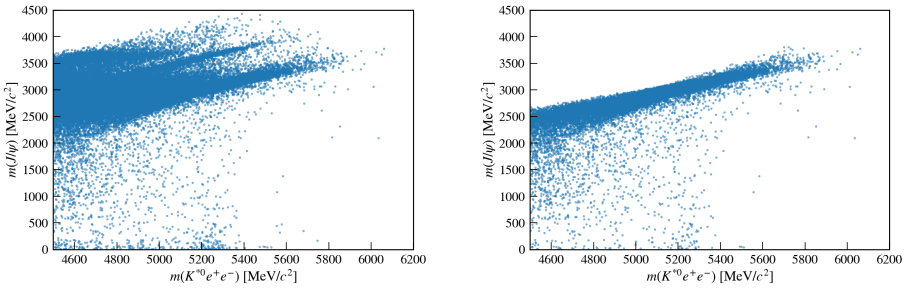


**Figure 3.2:** Effects of the part-reco cut on the $B^0$ and $J/\psi$ invariant mass distributions: before the cut application on the left and after the cut application on the right.

will be chosen to address the same backgrounds.

**Misidentified $\Lambda_b$ decays** refer to $\Lambda_b \to pKJ/\psi(\to e^+e^-)$ decays, in which the proton was mistaken for a pion and the final products are identical to the final products of the signal decay: a pion, a kaon and two electrons. It is a peaking background for the $B^0 \to K^{0*}J/\psi$ channel: it appears below the mass peak and can easily be mistaken for the signal. However, its contribution is not expected to be large and it will be modeled in the fit to the data.

**Misidentified $B_s^0$ decays** refer to a $B_s^0 \to \phi J/\psi$ decay, with $\phi$ decaying into two kaons: $\phi \to K^+K^-$. If one of the kaons is misidentified as pion, $\phi$ can be reconstructed as $K^{*0}$ and fall within the $K^{*0}$ invariant mass window. This background is reduced by requiring the invariant mass of the $K\pi$ system calculated using the $\pi \to K$ substitution to be greater than 1040 MeV/$c^2$ for events that have the probability of a pion to be identified as a pion smaller than 80%.

## 3.2 Data and simulation samples

The work presented in this thesis was performed using the data collected by the LHCb in $pp$ collisions. The data were taken during two data taking campaigns, called LHC Run 1 (2011 - 2012) and Run 2 (2015-2016 and 2017-2018), respectively. The data collected during Run 1 correspond to a total integrated luminosity of 3.0 fb$^{-1}$, and during Run 2 – to 6.0 fb$^{-1}$. The information about the data used is listed in Table 3.4.

In addition to the data samples, corresponding simulated samples are used. In this analysis two simulated samples were used: $B^0 \to K^{0*}J/\psi(\to e^+e^-)$ decays and $\Lambda_b \to pKJ/\psi(\to e^+e^-)$ decays. The first sample was used to develop the

| | Run 1 | | | Run 2 | | |
|---|---|---|---|---|---|---|
| Year | 2011 | 2012 | 2015 | 2016 | 2017 | 2018 |
| $\sqrt{s}$ [TeV] | 7 | | | 13 | | |
| $\int \mathcal{L}$ [fb$^{-1}$] | 1.1 | 2.1 | 0.3 | 1.7 | 1.7 | 2.2 |
| $N_{\text{ev}}^{\text{data}}$ | 18314 | 37311 | 9743 | 65796 | 62713 | 72720 |
| $N_{\text{ev}}^{\text{sim.}}$ | 87362 | 126014 | 66403 | 430195 | 174173 | 156031 |

**Table 3.4:** Information about the $pp$ collision conditions at the LHCb experiment and the size of the data and simulation $B^0 \to K^{0*} J/\psi$ samples used in this thesis.

angular acceptance parametrisation described in Chapter 4, and the second to develop a parametrisation of the background caused by the $\Lambda_b^0$ decays, described in Section 5.3.

In the simulation, $pp$ collisions are generated using `PYTHIA` [47, 48] with a specific LHCb configuration [49]. Decays of unstable particles are described by `EvtGen` [50], in which final-state radiation is generated using `PHOTOS` [51]. The interaction of the generated particles with the detector, and its response, are implemented using the `Geant4` toolkit [52, 53, 54].

While the simulated data aim at replicating the experimental data as well as possible, these cannot be reproduced perfectly. The discrepancies may be caused by mis-modelling of the $pp$ interaction or of the detector response. In order to compensate for that, a four-step correction procedure is introduced.

First a correction for the particle identification response is implemented. There is a large disagreement between the simulated and the actual LHCb detector response, caused by effects such as detector occupancy or changes in the operation conditions during the data taking campaigns. This is accounted for by using a re-sampling procedure, in which high-purity control samples (*i.e.* $D^{*+} \to D^0\pi^+$, $\Lambda^0 \to p\pi^-$, $\Lambda_c^+ \to pK^+\pi^-$ for hadrons, $J/\psi \to \mu^+\mu^-$ for muons and $B^+ \to J/\psi(\to e^+e^-)K^+$ for electrons) are used to correct known poorly modelled PID distributions [55].

Following that, a procedure is introduced to account for differences in trigger configurations. The real data is collected using different configurations (Trigger Configuration Keys, TCKs) while simulated data have a single configuration which leads to discrepancies. In order to minimize them, a tighter selection is applied to either real or simulated data, to match the set using tighter cuts to the set using looser cuts.

Another discrepancy between experimental and simulated samples comes from the mis-modelling of the $B$ kinematics. The variables with the largest deviations are typically the $p_{\mathrm{T}}$ of the $B^0$ candidate and the pseudorapidity $\eta$. To account for that, a dedicated multidimensional re-weighting [56] based on a Boosted Decision Tree (BDT) is performed, providing event-by-event weights.

Finally, the discrepancies coming from the trigger efficiencies have to be accounted for. The trigger efficiency is not well described in the simulation, as it depends on the detector occupancy. This correction is applied by assigning a correction factor to each of the simulated events so that the efficiency of the simulated sample matches the efficiency of the data [46].

Applying the aftermentioned four corrections results in a set of simulation samples that can be used in the analysis.

# 4 | Angular acceptance

Not every particle created during the collision will end up in the data set used for physics analysis. This is due to many different effects, such as the finite detector fiducial acceptance, the thresholds in the detector electronics, and the selection cuts needed to suppress backgrounds. These effects will lead to a distortion of the angular distributions of the final state particles, referred to as "acceptance effects". Figure 4.1 shows two simulated distributions of the $\cos\theta_K$ angle; the difference between them is the result of angular acceptance effects.

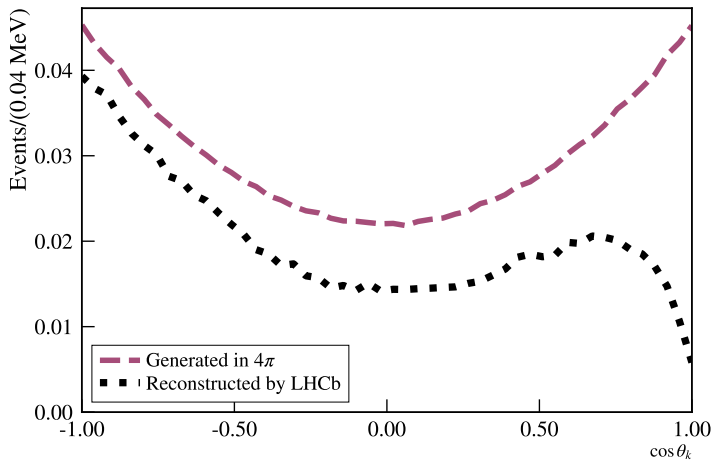


**Figure 4.1:** Distributions of the $\cos\theta_K$ angle in 2011 simulated data obtained with all events generated in the full phase space by the Monte Carlo generator (pink dashed line) and only with those events that were reconstructed by LHCb (black dotted line). The distributions are normalized to the number of events in the sample and the Generated line was shifted upwards for illustrative purpose.

In the analysis, the acceptance effects are accounted for by an efficiency function, defined as the ratio of the angular distributions after selection over the angular distribution that was generated, as described in Section 4.1. Also the angular resolution affects the reconstructed data and this is especially important for analyses involving electrons in the final state (see Section 2.6). In this analysis, the angular resolution effect on the angular distributions was included in the acceptance parametrisation, as described in Section 4.3. The details of the acceptance parametrisation obtained for this analysis are given in Section 4.4. Finally, the angular analysis might require splitting the available data set into sub-sets, which might impact the acceptance and require separate parametrisations. This has been tested for splits in data taking periods, bremsstrahlung recovery categories and bins of the invariant mass of the $K\pi$ system, $m_{K\pi}$. The details of this study are discussed in Section 4.5.

## 4.1 Angular acceptance in the PDF

The distortions of the angular distributions of the final state particles ("acceptance effects") can be parametrized with an efficiency function $\varepsilon(x)$. The efficiency is understood as the average probability for recording an event as function of $x$, in this instance the decay angles, $\vec{\Omega}$, integrating out all other degrees of freedom. In this analysis it is obtained from the simulated data.

The acceptance correction can then be applied in two ways. In the first one, the correction is performed by including a per-event weight, with each event weighted by the inverse of the efficiency function, $1/\varepsilon(x_i)$. In the second one, the acceptance is included in the probability density functions (PDFs, $\mathcal{P}$) describing the decay. This analysis takes the second approach. The probability density function of recorded events, $\mathcal{P}_{\text{obs}}(\Omega, \vec{S})$, can then be expressed as:

$$\mathcal{P}_{\text{obs}}(\Omega, \vec{S}) = \frac{\varepsilon(\Omega)\mathcal{P}_{\text{phys}}(\Omega, \vec{S})}{\int \mathrm{d}\Omega\ \varepsilon(\Omega)\mathcal{P}_{\text{phys}}(\Omega, \vec{S})}, \tag{4.1}$$

where $\mathcal{P}_{\text{phys}}(\Omega, \vec{S})$ is the normalized physics PDF describing only the physics-related properties of the decay (see Equation (1.15)). $\mathcal{P}_{\text{phys}}(\Omega, \vec{S})$ can be written as a linear combination of known angular functions:

$$\mathcal{P}_{\text{phys}}(\Omega, \vec{S}) = \sum_{k=0} S_k f_k(\Omega), \tag{4.2}$$

where $f_k$ are the PDF base functions and $S_k$ are the PDF coefficients. The base functions used in this analysis are shown in Table 4.1. The coefficients listed in the right column correspond to the $S_k$ coefficients. The coefficient $S_0$ is zero for the PDF in Equation (1.15). The function $f_0$ is included because the analysis also makes use of so-called "flat MC" samples which were generated with a PDF that has $S_0 = 1$ and all other coefficients zero.

| Name | Function | PDF coefficient |
|---|---|---|
| $f_0$ | $1$ | $0$ |
| $f_1$ | $\sin^2\theta_K\,(1+\cos^2\theta_l)/2$ | $(1-F_S)$ |
| $f_2$ | $(-1+5\cos^2\theta_K-\cos^2\theta_l-3\cos^2\theta_l\cos^2\theta_K)/2$ | $F_L(1-F_S)$ |
| $f_3$ | $\sin^2\theta_K\sin^2\theta_l\cos 2\phi$ | $S_3(1-F_S)$ |
| $f_4$ | $\sin 2\theta_K\sin 2\theta_l\cos\phi$ | $S_4(1-F_S)$ |
| $f_5$ | $\sin 2\theta_K\sin\theta_l\cos\phi$ | $S_5(1-F_S)$ |
| $f_6$ | $\sin^2\theta_K\cos\theta_l$ | $\frac{4}{3}A_{FB}(1-F_S)$ |
| $f_7$ | $\sin 2\theta_K\sin\theta_l\sin\phi$ | $S_7(1-F_S)$ |
| $f_8$ | $\sin 2\theta_K\sin 2\theta_l\sin\phi$ | $S_8(1-F_S)$ |
| $f_9$ | $\sin^2\theta_K\sin^2\theta_l\sin 2\phi$ | $S_9(1-F_S)$ |
| $f_{10}$ | $\sin^2\theta_l$ | $F_S$ |
| $f_{11}$ | $\sin^2\theta_l\cos\theta_K$ | $S_{S1}$ |
| $f_{12}$ | $\sin 2\theta_l\sin\theta_K\cos\phi$ | $S_{S2}$ |
| $f_{13}$ | $\sin\theta_l\sin\theta_K\cos\phi$ | $S_{S3}$ |
| $f_{14}$ | $\sin\theta_l\sin\theta_K\sin\phi$ | $S_{S4}$ |
| $f_{15}$ | $\sin 2\theta_l\sin\theta_K\sin\phi$ | $S_{S5}$ |

**Table 4.1:** The angular functions $f(\cos\theta_l, \cos\theta_K, \phi)$, together with the coefficients with which they appear in the PDF.

With the definition from Equation (4.2), the normalization integral in Equation (4.1) takes the form:

$$\begin{aligned}\int \mathrm{d}\Omega\ \varepsilon(\Omega)\mathcal{P}(\Omega,\vec{S}) &= \int \mathrm{d}\Omega\ \varepsilon(\Omega)\sum_k S_k f_k(\Omega) \\ &= \sum_k S_k \left[\int \mathrm{d}\Omega\ \varepsilon(\Omega) f_k(\Omega)\right].\end{aligned} \tag{4.3}$$

Using Equation (4.3), one can then define efficiency moments $a_k$ in the $f_k$ basis:

$$a_k \equiv \int \mathrm{d}\Omega\ \varepsilon(\Omega) f_k(\Omega) \tag{4.4}$$

and re-write Equation (4.1) as follows:

$$\mathcal{P}_{\mathrm{obs}}(\Omega,\vec{S}) = \frac{\varepsilon(\Omega)\mathcal{P}_{\mathrm{phys}}(\Omega,\vec{S})}{\sum_{k=0} S_k a_k}. \tag{4.5}$$

When fitting a model without a background, the efficiency function $\varepsilon(\Omega)$ drops out of the likelihood minimization and only the efficiency moments matter. When fitting a model with a background, an explicit representation of $\varepsilon(\Omega)$ is needed (this representation is also needed for plotting projections of the PDF overlaid with the data or for generating events for toy studies).

In Section 4.4 it is described how $\varepsilon(\Omega)$ is parametrized in terms of polynomial and periodic basis functions. Because this parametrization is not perfect, the choice of functions necessarily leads to a systematic uncertainty in the analysis. As will be shown in Section 4.2, the efficiency moments in the denominator of Equation (4.5) can be computed from MC samples without an explicit representation of $\varepsilon(\Omega)$. Consequently, in order to minimize the impact of the systematic uncertainty, the efficiency in the numerator and the efficiency moments in the denominator of Equation (4.5) will be treated separately.

## 4.2 Monte Carlo integration

The efficiency moments $a_k$ can be calculated using Monte Carlo simulations and the Monte Carlo numerical integration method for definite integrals [57]. In this method, a multidimensional integral

$$I = \int_V g(\bar{x}) \mathrm{d}\bar{x} \tag{4.6}$$

can be approximated, in the case of a uniform distribution of $\bar{x}_i$, as

$$I \approx V \frac{1}{N} \sum_{i=1}^{N} g(\bar{x}_i), \tag{4.7}$$

where $N$ is the number of data points and $V = \int_V \mathrm{d}x$. In the case of a non-uniform distribution of $\bar{x}_i$:

$$I \approx \frac{1}{N} \sum_{i=1}^{N} \frac{g(\bar{x}_i)}{p(\bar{x}_i)}, \tag{4.8}$$

with $p(\bar{x})$ is the PDF with which the sample $\bar{x}_i$ was generated.

To compute the efficiency moments, Equation (4.8) is used with $g(\Omega) = \varepsilon(\Omega) f_i(\Omega)$. It can be shown [56] that, for the purpose of the computation of the integral, $\varepsilon(\Omega)$ takes only two values, namely 1 for selected events and 0 for the other events. Consequently, the efficiency moments can be computed as:

$$a_k = \frac{1}{n_{\mathrm{sel}}} \sum_{i}^{n_{\mathrm{sel}}} \frac{f_k(\Omega_i)}{\mathcal{P}_{\mathrm{gen}}(\Omega_i)}, \tag{4.9}$$

where the sum only runs over selected events. Because the PDF in Equation (4.6) is insensitive to an overall scale factor of the efficiency functions, $n_{\mathrm{gen}}$ is replaced by $n_{\mathrm{sel}}$ in Equation (4.9).

As mentioned in Section 3.2, the differences between the simulation sample used for the parametrisation and the data used in the fit are corrected using per-event weights, $w_i$. These weights are included in the efficiency moments by modifying Equation (4.9):

$$a_k = \frac{1}{N'} \sum_{i} w_i \frac{f_k(\Omega_i)}{\mathcal{P}_{\mathrm{gen}}(\Omega_i)}, \tag{4.10}$$

where the normalization is chosen to be $N' = \sum w_i$.

As Equation (4.10) shows, the efficiency moments depend on two variables: the distributions of the angles $\Omega$ and the parameters of the PDF of the events generated in the phase space, $\mathcal{P}_{\mathrm{gen}}$.

## 4.3 Angular resolution

The finite resolution of the detector, in particular the electron momentum resolution (see Section 2.6), also distorts the shape of the angular distributions. Under certain conditions this effect can be included in the efficiency parametrisation.

In Equation (4.1) – (4.10), the values of the observables $\Omega$ are coming only from the physics of the decay. In the simulation they are referred to as "true values" and are the values originally generated by the Monte Carlo generator. In the simulation, another set of variables, the "reconstructed values", are obtained using the same reconstruction process used to reconstruct real data collected during a collision. A PDF $\mathcal{P}_{\text{obs}}$ accounting for both acceptance and resolution effects can be obtained modifying Equation (4.1) as follows:

$$\mathcal{P}_{\text{obs}}(\Omega_{\text{reco}}|S) = \frac{1}{N}\int \mathrm{d}\Omega_{\text{true}}\ R(\Omega_{\text{reco}}|\Omega_{\text{true}})\varepsilon(\Omega_{\text{true}})\mathcal{P}_{\text{phys}}(\Omega_{\text{true}}|S), \tag{4.11}$$

where $N$ is an overall normalization and $R(\Omega_{\text{reco}}|\Omega_{\text{true}})$ is the resolution function.

In practice, the effect of the angular resolution of the detector will be visible as a distortion of the angular distributions and can be accounted for in a modified efficiency function $\bar{\varepsilon}$, re-defined as follows:

$$\bar{\varepsilon}(\Omega_{\text{reco}}) \equiv \frac{\int \mathrm{d}\Omega_{\text{true}}\ R(\Omega_{\text{reco}}|\Omega_{\text{true}})\varepsilon(\Omega_{\text{true}})\mathcal{P}_{\text{phys}}(\Omega_{\text{true}}|S)}{\mathcal{P}_{\text{phys}}(\Omega_{\text{reco}}|S)}, \tag{4.12}$$

such that Equation (4.1) can be rewritten as:

$$\mathcal{P}_{\text{obs}}(\Omega_{\text{reco}}|S) = \frac{1}{N}\mathcal{P}_{\text{phys}}(\Omega_{\text{reco}}|S)\bar{\varepsilon}(\Omega_{\text{reco}}). \tag{4.13}$$

For the modified efficiency function $\bar{\varepsilon}(\Omega_{\text{reco}})$, efficiency moments can be defined analogously to Equation (4.4):

$$\begin{aligned}\bar{a}_k &\equiv \int \mathrm{d}\Omega_{\text{reco}}\ f_k(\Omega_{\text{reco}})\bar{\varepsilon}(\Omega_{\text{reco}}) \\ &= \int \mathrm{d}\Omega_{\text{reco}}\ f_k(\Omega_{\text{reco}})\frac{\int \mathrm{d}\Omega_{\text{true}} R(\Omega_{\text{reco}}|\Omega_{\text{true}})\varepsilon(\Omega_{\text{true}})\mathcal{P}_{\text{phys}}(\Omega_{\text{true}}|S)}{\mathcal{P}_{\text{phys}}(\Omega_{\text{reco}}|S)}.\end{aligned} \tag{4.14}$$

Again, using a Monte Carlo integration method one can calculate the moments with [56]:

$$\bar{a}_k = \frac{1}{n_{\text{sel}}}\sum_i^{n_{\text{sel}}} \frac{f_k(\Omega_{\text{reco},i})}{\mathcal{P}_{\text{gen}}(\Omega_{\text{true},i}|S_{\text{gen}})}\frac{\mathcal{P}_{\text{phys}}(\Omega_{\text{true}}|S_{\text{phys}})}{\mathcal{P}_{\text{phys}}(\Omega_{\text{reco}}|S_{\text{phys}})}. \tag{4.15}$$

Equation (4.12) and (4.15) in principle provide a calculation framework for the estimation of the efficiency function $\bar{\varepsilon}$. In practice, the parameters $S$ of the physics PDF are not known a priori and only later estimated by performing a maximum likelihood fit, requiring this estimation to be carried out in an iterative procedure. First, a set of temporary moments is calculated using Equation (4.15), with $S_{\text{gen}}$ values used in place of $S_{\text{phys}}$. This results in a set of moments that does not correctly account for the resolution effects. These moments are then used in a maximum likelihood fit to obtain a set of PDF parameters $S$. This allows for a second iteration with $S_{\text{phys}}$ values, during which a set of moments that take the resolution effects into account is obtained.

The difference between Equation (4.9) and Equation (4.15) is only due to the model with which the sample was generated. If one would assume the correct model $S_{\text{gen}} \approx S_{\text{phys}}$, the formula becomes:

$$\bar{a}_k \approx \frac{1}{n_{\text{sel}}} \sum_{i}^{n_{\text{sel}}} \frac{f_k(\Omega_{\text{reco},i})}{\mathcal{P}_{\text{gen}}(\Omega_{\text{reco},i}|S)}. \tag{4.16}$$

It will be shown later that the uncertainty arising from this assumption is small and can be included in the systematic uncertainties.

## 4.4 Acceptance parametrisation

The angular efficiency in the numerator of Equation (4.5) can be parametrised in a number of ways, depending on the choice of base functions. In this analysis, a combination of Legendre polynomials and Fourier series terms is used, without assuming factorization between the decay angles $\vec{\Omega} = (\cos\theta_l, \cos\theta_K, \phi)$. The efficiency function is parametrised as:

$$\varepsilon(\cos\theta_l, \cos\theta_K, \phi) = \sum_{klm} c_{klm} L_k(\cos\theta_l) L_l(\cos\theta_K) F_m(\phi), \tag{4.17}$$

where $c_{klm}$ denotes the acceptance parameters and functions $L_{k,l}(x)$ and $F_m(x)$ refer to the base functions used in this parametrisation: Legendre polynomials and Fourier series terms, respectively.

Legendre polynomials $L_{k,l}(x)$ [58], where $k, l$ denote the polynomial order, were chosen to parametrise the distributions of $\cos\theta_l$ and $\cos\theta_K$, making use of their orthogonality under simple inner product:

$$\int_{-1}^{+1} L(x,k) L(x,k') \mathrm{d}x = \frac{2}{2k+1} \delta_{kk'}. \tag{4.18}$$

Fourier series were chosen to parametrise the azimuthal angle $\phi$, in order to ensure the continuity of the function at $\pm\pi$:

$$F_m(x) = \begin{cases} \cos(\frac{mx}{2}) & \text{if } m \text{ even}, \\ \sin(\frac{(m+1)x}{2}) & \text{if } m \text{ odd}. \end{cases} \tag{4.19}$$

In Equation (4.17), the factor $p_m$ comes from the orthogonality of Fourier series terms:

$$\int_{-1}^{+1} F(x,m) F(x,m') \mathrm{d}x = p_{mm'}, \tag{4.20}$$

where

$$p_{mm'} = \begin{cases} 2\pi & \text{if } m = m' = 0, \\ \pi & \text{if } m = m \neq 0, \\ 0 & \text{if } m \neq m'. \end{cases} \tag{4.21}$$

Since the base functions are orthogonal, the parameters $c_{klm}$ are calculated using the Monte Carlo integration method (see Equations (4.4) – (4.9)):

$$c_{klm} = \frac{1}{N'} \sum_{i=1}^{N} \frac{(w_i)}{\mathcal{P}_{\mathrm{gen}}(\Omega_i)} \left[ \left( \frac{2}{2k+1} \right) \left( \frac{2}{2l+1} \right) \left( \frac{1}{p_{mm'}} \right) L_k(\cos\theta_l) L_l(\cos\theta_K) F_m(\phi) \right], \tag{4.22}$$

where $w_i$ stands for the per-candidate event weights used to account for data and MC differences, as explained in Section 3.2, and $N' \equiv \sum_{i=1}^{N} w_i$ with the sum running only over the events passing the selection.

In the $c_{klm}$ calculation, only a finite set of base function terms is used and this introduces a systematic uncertainty in the parametrisation. The impact of using only a finite subset of Legendre polynomials and Fourier series terms has been estimated using the efficiency moments in Equation (4.4). Although these were introduced to compute the PDF normalization without having to worry about the efficiency parametrisation (see Section 4.2), one can instead perform the integral in Equation (4.4) using an explicit efficiency parametrisation obtained with a finite set of base function terms. These two approaches are shown schematically in Figure 4.2. The differences between the two sets of efficiency moments will reflect the bias due to the fact that only a finite subset of Legendre polynomials and Fourier series terms are used.

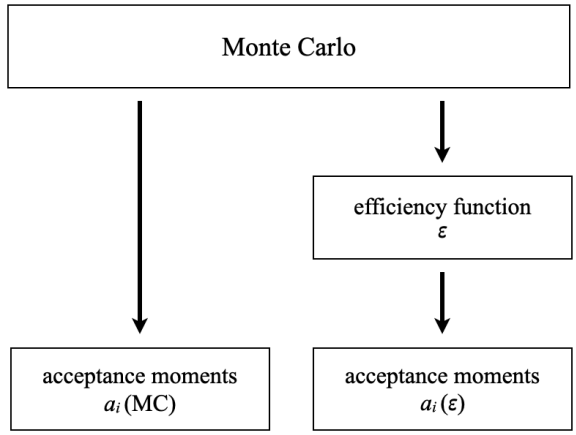


**Figure 4.2:** Scheme of the evaluation of acceptance parametrisation.

The acceptance parametrisation is modeled using the lowest orders of the Legendre polynomials and Fourier series terms that show a good description of the angular distributions. These terms are chosen such that the difference between the efficiency moments $a_i(\text{MC})$ and $a_i(\varepsilon)$, according to the scheme in Figure 4.2, is smaller than the statistical error of $a_i(\text{MC})$.

| i | $a_i$ (MC) | $a_i$ ($\varepsilon$) | | |
|---|---|---|---|---|
| | | $(2,2,2)$ | $(4,5,4)$ | $(7,6,4)$ |
| 01 | $0.47757 \pm 0.00026$ | 0.47795 | 0.47683 | 0.47689 |
| 02 | $-0.09700 \pm 0.00067$ | −0.09712 | −0.09405 | −0.09429 |
| 03 | $0.00676 \pm 0.00055$ | −0.00008 | 0.00705 | 0.00698 |
| 04 | $-0.01131 \pm 0.00048$ | −0.00835 | −0.01200 | −0.01178 |
| 05 | $-0.00072 \pm 0.00048$ | −0.00105 | −0.00067 | −0.00073 |
| 06 | $0.00438 \pm 0.00060$ | 0.00436 | 0.00427 | 0.00414 |
| 07 | $0.00022 \pm 0.00045$ | 0.00001 | 0.00019 | 0.00032 |
| 08 | $0.00033 \pm 0.00044$ | 0.00062 | 0.00042 | 0.00063 |
| 09 | $0.00056 \pm 0.00056$ | −0.00001 | 0.00094 | 0.00058 |
| 10 | $0.65928 \pm 0.00042$ | 0.65986 | 0.66210 | 0.66223 |
| 11 | $-0.07923 \pm 0.00039$ | −0.07938 | −0.07754 | −0.07759 |
| 12 | $-0.01275 \pm 0.00060$ | −0.01245 | −0.01297 | −0.01322 |
| 13 | $0.00071 \pm 0.00069$ | 0.00100 | 0.00035 | 0.00021 |
| 14 | $0.00184 \pm 0.00063$ | 0.00163 | 0.00198 | 0.00177 |
| 15 | $-0.00104 \pm 0.00056$ | −0.00132 | −0.00119 | −0.00096 |

**Table 4.2:** Efficiency moments, all normalized on the first efficiency moment $a_{00}$, obtained with the methods shown in Figure 4.2. Numbers $(k,l,m)$ refer to the maximal order of the Legendre polynomial and Fourier series in the method described in Section 4.4. The error of the numbers in the first column represents the uncertainties coming from the statistics of the MC sample.

The results obtained for three polynomial order combinations are summarized in Table 4.2, with all efficiency moments normalized on the first efficiency moment $a_{00}$. In the first column ($a_i$ (MC)) are listed the efficiency moments obtained directly from the simulated data and in the remaining ones ($a_i$ ($\varepsilon$)) the efficiency

moments obtained with the procedure described in Figure 4.2, using a given maximum Legendre polynomial and Fourier series orders. The differences between the efficiency moments obtained with these two methods are shown in Table 4.3; the discrepancies between the two values can be considered a measure of the bias in the method described in this section.

| mom. | $\Delta(\mathrm{MC}-222)$ | $\Delta(\mathrm{MC}-454)$ | $\Delta(\mathrm{MC}-764)$ |
|---|---|---|---|
| 01 | $-0.00037 \pm 0.00026$ | $0.00075 \pm 0.00026$ | $0.00069 \pm 0.00026$ |
| 02 | $0.00012 \pm 0.00067$ | $-0.00295 \pm 0.00067$ | $-0.00271 \pm 0.00067$ |
| 03 | $0.00683 \pm 0.00055$ | $-0.00029 \pm 0.00055$ | $-0.00022 \pm 0.00055$ |
| 04 | $-0.00296 \pm 0.00048$ | $0.00069 \pm 0.00048$ | $0.00046 \pm 0.00048$ |
| 05 | $0.00032 \pm 0.00048$ | $-0.00005 \pm 0.00048$ | $0.00001 \pm 0.00048$ |
| 06 | $0.00001 \pm 0.00060$ | $0.00011 \pm 0.00060$ | $0.00024 \pm 0.00060$ |
| 07 | $0.00022 \pm 0.00045$ | $0.00003 \pm 0.00045$ | $-0.00010 \pm 0.00045$ |
| 08 | $-0.00029 \pm 0.00044$ | $-0.00009 \pm 0.00044$ | $-0.00031 \pm 0.00044$ |
| 09 | $0.00058 \pm 0.00056$ | $-0.00037 \pm 0.00056$ | $-0.00001 \pm 0.00056$ |
| 10 | $-0.00059 \pm 0.00042$ | $-0.00283 \pm 0.00042$ | $-0.00296 \pm 0.00042$ |
| 11 | $0.00015 \pm 0.00039$ | $-0.00169 \pm 0.00039$ | $-0.00164 \pm 0.00039$ |
| 12 | $-0.00030 \pm 0.00060$ | $0.00022 \pm 0.00060$ | $0.00047 \pm 0.00060$ |
| 13 | $-0.00029 \pm 0.00069$ | $0.00036 \pm 0.00069$ | $0.00049 \pm 0.00069$ |
| 14 | $0.00021 \pm 0.00063$ | $-0.00013 \pm 0.00063$ | $0.00007 \pm 0.00063$ |
| 15 | $0.00028 \pm 0.00056$ | $0.00016 \pm 0.00056$ | $-0.00007 \pm 0.00056$ |

**Table 4.3:** Differences between the values of the efficiency moments obtained directly from the simulated data and from the efficiency function $\varepsilon$ with different maximum polynomial and series orders, presented in Table 4.2. The uncertainty includes only the statistical uncertainty in $a_i(MC)$.

The projections of the acceptance-corrected PDF, corresponding to the parametrisations considered in Table 4.3 ($a_i$ ($\varepsilon$)) are shown in Figure 4.3. One can observe that the parametrisation with low maximum orders, $(k, l, m) = (2, 2, 2)$, does not provide a sufficiently accurate acceptance description. The parametrisation with higher maximum orders, $(k, l, m) = (4, 5, 4)$, shows a better description of the angular distributions. However, the discrepancies between the efficiency

moments $a_i(\mathrm{MC})$ and $a_i(\varepsilon)$ are still large, as shown in Table 4.3. This does not improve with the increase of the maximum orders, $(k, l, m) = (7, 6, 4)$. In addition, increasing the orders carries the risk of artificial modelling of the statistical fluctuations of the angular distributions. It was decided that, despite the discrepancies, the acceptance parametrisation obtained with $(k, l, m) = (4, 5, 4)$ will be used and that the bias will be included in the systematic uncertainties.

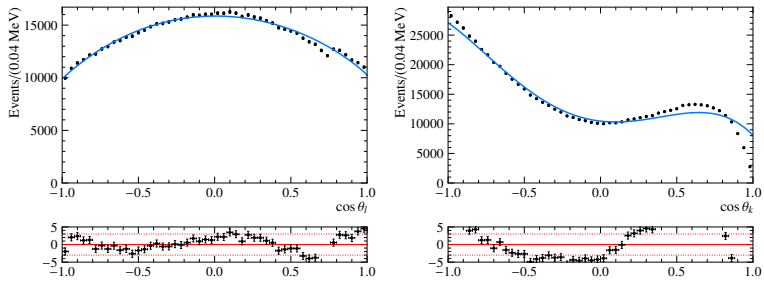


**(a)**

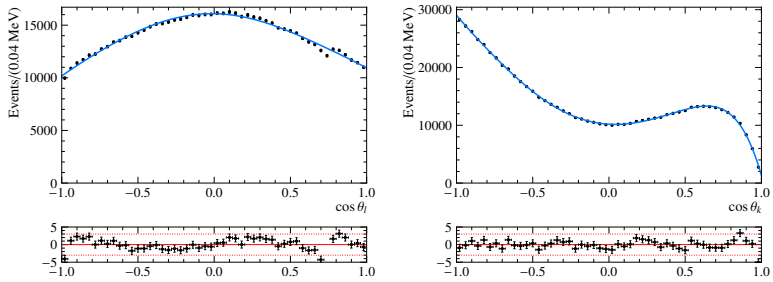


**(b)**

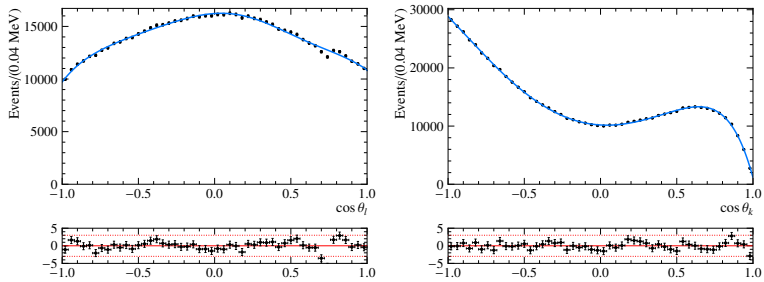


**(c)**

**Figure 4.3:** Projections of the acceptance-corrected decay PDF for $\cos\theta_l$ (*left*) and $\cos\theta_K$ (*right*) integrated over the two remaining angles, overlaying data points corresponding to the simulated data for Run 2. Three choices of polynomial orders $(k, l, m)$ are presented: $(2, 2, 2)$ (a), $(4, 5, 4)$ (b) and $(7, 6, 4)$ (c).

## 4.5 Acceptance in different subsets of the data

The data set used in this analysis corresponds to the full available LHCb data. However, in the future it might be beneficial to split the data set in different sub-samples. The acceptance parametrisation would have to be obtained separately for each of the data subsets. If the acceptance differs significantly, treating each sub-set separately may decrease the systematic uncertainty. However, it comes at a cost of an increased statistical uncertainty.

The differences in acceptance were studied for various splits of the data, such as years of data taking, bremsstrahlung recovery categories and bins of the invariant mass of the $K\pi$ system, $m_{K\pi}$. To illustrate the differences between these subsets, the values of efficiency moments were compared. Since the absolute values of the efficiency moments can differ by order of magnitudes, they will be compared after the subtraction of the values of the efficiency moments obtained for the full data set.

Figures 4.4 and 4.5 show the efficiency moments obtained for different years of Run 1 and Run 2, respectively. The consistency between the two years of Run 1 seems better than that among the years of Run 2, but overall the differences are considered small and do not point to benefits of splitting the data in the angular fit.

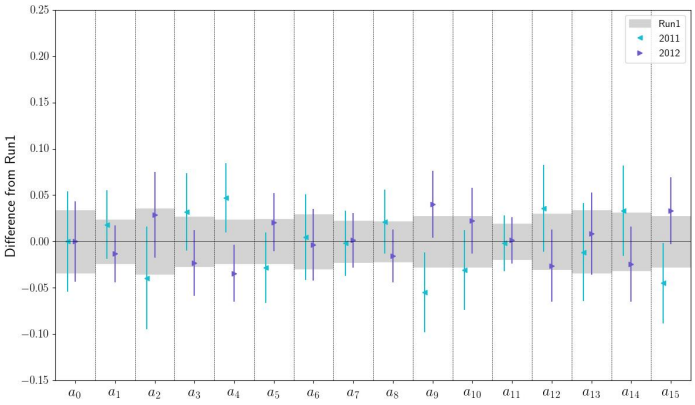


**Figure 4.4:** Efficiency moments for different years of Run 1, after subtraction of the values obtained with full Run 1; the indicated uncertainties are only statistical.

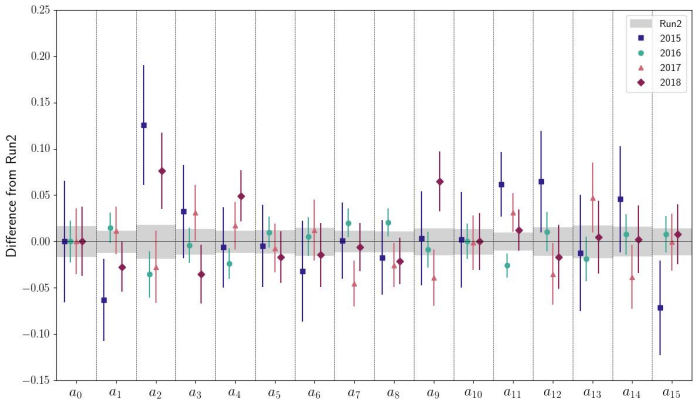


**Figure 4.5:** Efficiency moments for different years of Run 2, after subtraction of the values obtained with full Run 2; the indicated uncertainties are only statistical.

Another variable according to which data were split was the bremsstrahlung recovery for the electrons in the event – known as bremsstrahlung categories, explained in Section 2.6. Figures 4.6 and 4.7 show the efficiency moments for each of the categories for Run 1 and Run 2. For both runs, but especially for Run 2, there are significant discrepancies between the three categories.

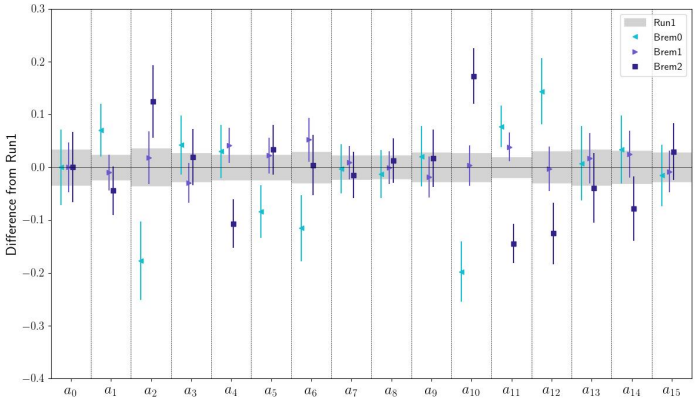


**Figure 4.6:** Efficiency moments for different bremsstrahlung categories in Run 1, after subtraction of the values obtained with full data sample; the indicated uncertainties are only statistical.

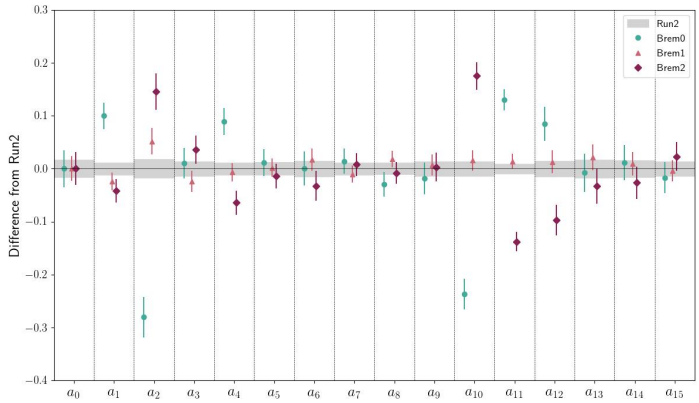


**Figure 4.7:** Efficiency moments for different bremsstrahlung categories in Run 2, after subtraction of the values obtained with full data sample; the indicated uncertainties are only statistical.

The final variable considered was the invariant mass of the $K\pi$ system, $m_{K\pi}$. The interference terms in Equation (1.16), $S_{s1}$ – $S_{s5}$, although it is not shown explicitly, are dependent on $m_{K\pi}$ [59]. However, it is not modeled in the fit and not accounted for in the efficiency parametrisation. If the efficiency depends on $m_{K\pi}$, it is then important to obtain the efficiency parametrisation from a simulation with the right $m_{K\pi}$ distribution. In the simulated data used in this analysis it is not the case: it does not include the S-wave and does not model $m_{K\pi}$ well.

To study the possibility of this dependence, the data is split in six different bins of the $K\pi$ invariant mass, following previous analyses [59]. The bins shown in Table 4.4 and indicated in the $m_{K\pi}$ distribution shown in Figure 4.8.

| | | | | | | |
|---|---|---|---|---|---|---|
| $m^{\text{min}}_{K\pi}$ [MeV/c$^2$] | 795.9 | 826.0 | 861.0 | 896.0 | 931.0 | 966.0 |
| $m^{\text{max}}_{K\pi}$ [MeV/c$^2$] | 826.0 | 861.0 | 896.0 | 931.0 | 966.0 | 995.9 |

**Table 4.4:** Bins of the invariant mass of the $K\pi$ system, $m_{K\pi}$, used in the analysis.

The efficiency moments calculated for each $m_{K\pi}$ bins are shown in Figure 4.9. The variations indicate a strong dependence of the efficiency on the $K\pi$ invariant mass. This effect will be accounted for in the systematic uncertainties. In addition, another fit will be performed in which the data is split into six $m_{K\pi}$ bins to study this effect, discussed in Section 5.4.3.

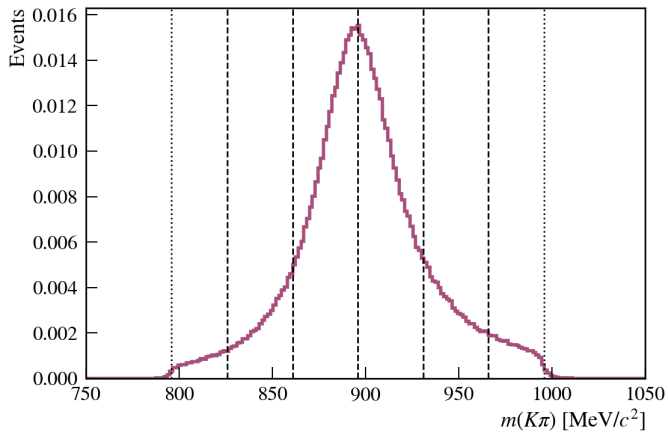


**Figure 4.8:** Distribution of the $m_{K\pi}$ invariant mass in Run 2 data. Mass bins are denoted by the dashed lines.

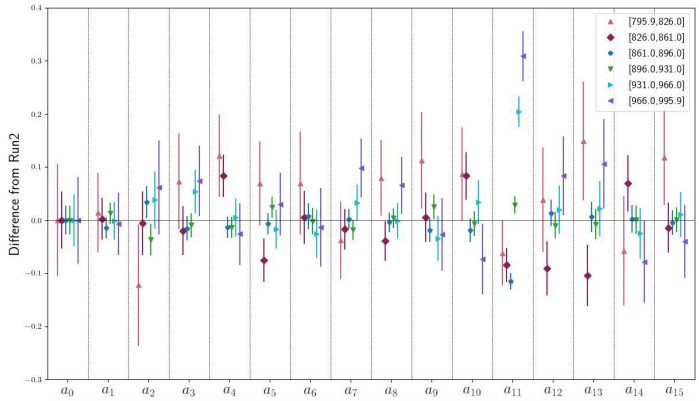


**Figure 4.9:** Efficiency moments in bins of $m_{K\pi}$ (Run 2 simulated data), presented as a difference from average.

# 5 | Angular analysis

The angular analysis of $B^0 \to K^{0*}e^+e^-$ decays aims at extracting the angular observables from the four-dimensional decay rate in Equation (1.15). This is achieved by performing an unbinned maximum likelihood fit, described in Section 5.1. The details of the signal modeling are described in Section 5.2 and the background modeling is presented in Section 5.3. The maximum likelihood fit of the control channel $B^0 \to K^{0*}J/\psi$ is presented in Section 5.4 and the results are compared to the results of the $B^0 \to K^{0*}\mu^+\mu^-$ analyses [59]. In order to better understand the contribution of the S-wave, also angular observables in bins of $m_{K\pi}$ were measured. The studies of the systematic uncertainties are presented in Section 5.5.

## 5.1 Likelihood fit

A likelihood fit is performed in order to extract a set of parameters $\theta = (\theta_1, ..., \theta_M)$ that best describe the data $x = (x_1, ..., x_N)$ by maximizing the likelihood function $\mathcal{L}$. The likelihood is defined as a product of all conditional probability density functions $\mathcal{P}$ describing the measurements:

$$\mathcal{L}(\vec{\theta}) = \prod_{i=1}^{N} \mathcal{P}(x_i|\vec{\theta}). \tag{5.1}$$

The number of observations $N$ in the samples used in this analysis follows a Poisson distribution with the mean $\mu$, corresponding to the expected number of observations depending on the model parameters and therefore a modified likelihood function is used:

$$\mathcal{L}(\vec{\theta}) = \frac{\mu^N}{N!} e^{-\mu} \prod_{i=1}^{N} \mathcal{P}(x_i|\vec{\theta}), \tag{5.2}$$

often called "extended likelihood" [60, 61, 62].

It is customary to use a logarithm of the likelihood function, $\ln \mathcal{L}$, since both $\mathcal{L}$ and $\ln \mathcal{L}$ are maximized for the same values of $\theta$. The maximum likelihood estimator can be found by solving the likelihood equations:

$$\frac{\partial \ln \mathcal{L}}{\partial \theta_i} = 0. \tag{5.3}$$

In this analysis, an unbinned extended maximum likelihood fit is applied to the distributions of the invariant mass and decay angles of the $B^0$ candidates. The fit is implemented in the `zfit` toolkit [63], which relies on the `minuit` package [64] for the minimization of $\ln \mathcal{L}$.

The fit accounts for the signal and two possible background sources: the combinatorial background and misidentified $\Lambda_b$ decays, each of them described with individual PDFs. The fit takes as parameters both the parameters of the PDFs as well as the yield of each of these components. However, it is important to note that in this implementation of the fit the yield of the $\Lambda_b$ background is relative to the yield of the signal expressed as:

$$\mathcal{P} = (1 - f) \times \mathcal{P}_{\text{sign}} + f \times \mathcal{P}_{\Lambda_b}, \tag{5.4}$$

where $f$ is a fixed relative fraction of the $\Lambda_b$ decays over $B^0 \to K^{0*} J/\psi$ decays. This choice was made due to the nature of the two PDFs: since the $\Lambda_b \to pKJ/\psi(\to e^+e^-)$ decay is a peaking background, both components have a similar shape, as explained in Section 3.1.2.

The fraction $f$ is calculated in the following way:

$$f = \frac{f_{\Lambda_b^0}}{f_d} \frac{\mathcal{B}(\Lambda_b^0 \to pKJ/\psi(\to ee))}{\mathcal{B}(B \to K^{*0} J/\psi(\to ee)) \times \mathcal{B}(K^{*0} \to K\pi)} \frac{\varepsilon_{\text{tot}}^{\Lambda_b^0}}{\varepsilon_{\text{tot}}^{B^0}} = 0.0011 \pm 0.0002, \tag{5.5}$$

where $f_q \equiv \mathcal{B}(b \to B_q)$, $f_{\Lambda_b} \equiv \mathcal{B}(b \to \Lambda_b)$ and $f_{\Lambda_b^0}/f_d = 2 \times f_{\Lambda_b^0}/(f_u + f_d)$ are the fractions of the quark and $\Lambda_b^0$ baryon to light $B$ meson production, respectively [65]. $\mathcal{B}$ refers to branching fractions of the decays, and $\varepsilon_{\text{tot}}$ is the reconstruction, trigger and selection efficiency calculated from simulation. The uncertainty on this number is dominated mostly by the branching fraction uncertainty [1] (see Section 5.5).

## 5.2 Signal model

The signal is modeled in four dimensions: the invariant mass of the decay products, $m_{K\pi ee}$, and the decay angles $\Omega = (\cos\theta_l, \cos\theta_K, \phi)$. Factorisation of the decay PDF, $\mathcal{P}_{\text{sign}}(m, \Omega)$, in mass and angles is assumed:

$$\mathcal{P}_{\text{sign}}(m, \Omega|S) = \mathcal{P}_{\text{sign}}(m) \times \mathcal{P}_{\text{sign}}(\Omega|S), \tag{5.6}$$

with $S$ indicating the angular coefficients of the PDF.

Although the objective of the analysis is extracting the angular parameters, the mass fit is an essential part of the process. A simultaneous fit to the invariant mass and the decay angles ensures a good separation of signal and background contributions. The parameters of the angular distribution of the background are left 'free' in the fit.

### 5.2.1 Invariant mass signal model

The shape of the invariant mass distribution of the signal candidates is parametrised using a sum of two Crystal Ball functions (DCB) [66], combined with a Gaussian function, in order to improve the modeling of the tails of the mass distribution. The two Crystal Ball functions have common mean $\mu$ and width $\sigma$, but different tail parameters $\alpha$ and $n$. The Gaussian function shares the $\mu$ parameter with the DCB and has its own width $\sigma_{\text{G}}$.

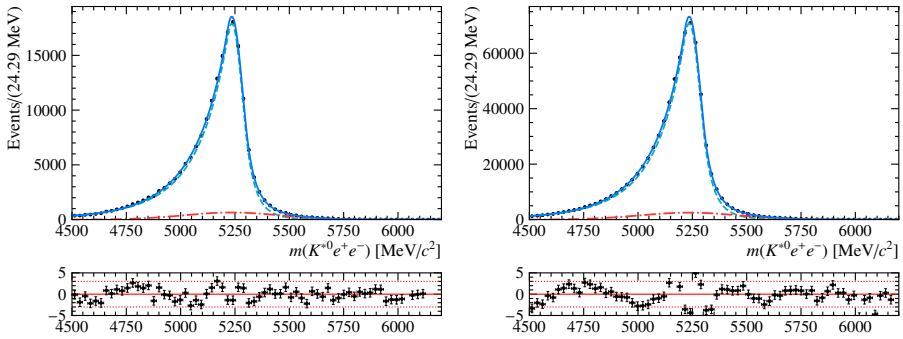


**Figure 5.1:** Invariant mass fits to Run 1 and Run 2 simulated data. The green line denotes the DCB contribution, the red line the Gauss contribution, and the blue line the sum of both.

| par. | Run 1 | | Run 2 | |
|---|---|---|---|---|
| $\mu$ | 5235 | $\pm$ 0.144 | 5236 | $\pm$ 0.08410 |
| $\sigma$ | 51.14 | $\pm$ 0.094 | 52.87 | $\pm$ 0.03805 |
| $\alpha_0$ | 0.367 | $\pm$ 0.005 | 0.391 | $\pm$ 0.00276 |
| $\alpha_1$ | 1.263 | $\pm$ 0.022 | 1.255 | $\pm$ 0.01195 |
| $n_0$ | 7.268 | $\pm$ 0.440 | 7.069 | $\pm$ 0.20671 |
| $n_1$ | 7.740 | $\pm$ 2.329 | 7.383 | $\pm$ 1.04499 |
| $\sigma_{\mathrm{G}}$ | 221.0 | $\pm$ 4.725 | 229.2 | $\pm$ 2.62434 |
| $f$ | 0.922 | $\pm$ 0.015 | 0.921 | $\pm$ 0.00786 |

**Table 5.1:** Invariant mass fit results to Run 1 and Run 2 $B^0 \to K^{0*}J/\psi(\to e^+e^-)$ simulated data.

The results of the fits to the $B^0 \to K^{0*}J/\psi$ simulated data sets are shown in Figure 5.1 and the resulting fit parameters are shown in Table 5.1. The fit model describes well the simulated data, with the exception of the region around $m(K^{*0}ee) = 4800\,\mathrm{MeV/c^2}$. This is not considered to be a substantial issue and this model will be used in the analysis. Furthermore, this problem appears only in the simulation and should not pose an issue in the analysis of $B^0 \to K^{0*}e^+e^-$ decays, in which the statistical error will be significantly larger.

For the purpose of the final fit, some of the parameters are fixed in order to ensure a good signal-background separation. The parameters that are actually fitted to the data are $\mu$, $\sigma$ and $\sigma_{\mathrm{G}}$.

### 5.2.2 Angular signal model

The shape of the angular distributions $\Omega = (\cos\theta_l, \cos\theta_K, \phi)$ is described by the differential decay rate (Equations (1.15) and (1.16)). The angular coefficients are the fit parameters. To account for the resolution and acceptance effects discussed in Chapter 4, the angular efficiency has been included in the angular PDF, as shown in Equation (4.1). The efficiency function has been parametrized with the Legendre polynomials up to order four for $\cos\theta_l$, order five for $\cos\theta_K$, and Fourier series terms up to four for $\phi$, see Section 4.4.

Figure 5.2 shows the angular distributions in the simulated data for Run 1 and Run 2, overlaid with the best fit model. The step visible in the $\cos\theta_l$ distribution around $\cos\theta_l = \pm 0.8$ is connected to the presence of veto against $B \to \bar{D}^0(\to$

$K^+\pi^-)\pi^- e^+\nu_e$ and $B \to D^-(\to K^+\pi^+\pi^-)e^+\nu_e$ decays, discussed in Section 3.1.2. While it is not yet done in this analysis, this veto will be removed for the analysis of the $B^0 \to K^{0*}e^+e^-$ decay.

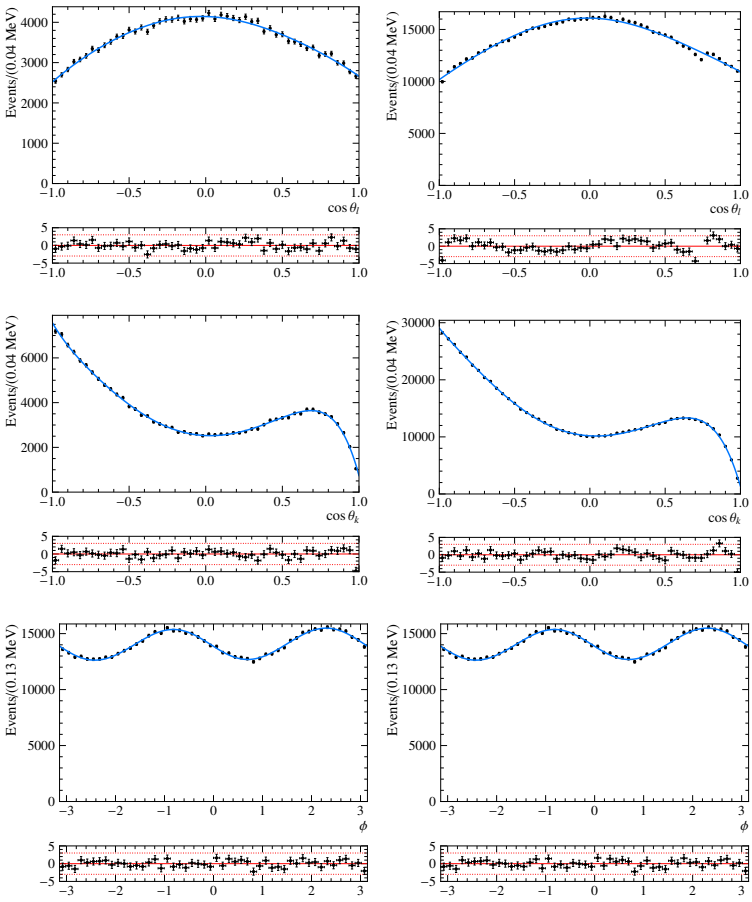


**Figure 5.2:** Distributions of the angular variables in Run 1 (*left*) and Run 2 (*right*) $B^0 \to K^{0*}J/\psi$ simulated data. The curve denotes the PDF resulting from the fit to the data.

To test the fitting procedure the parameters resulting from the fit to the simulated data were compared with the parameter values that were used to generate the data, as shown in Table 5.2. The values obtained in the fit are close to the generator values because the same sample of simulated data was used to compute the efficiency moments for the fit as well as in the fit itself. As a result, any 'statistical fluctuations' in that sample are absorbed in the efficiency moments. This result also shows that it is essential that the efficiency moments are computed with the correct generator level values.

| par. | Gen. | Run 1 | Run 2 |
|---|---|---|---|
| $F_L$ | 0.60035 | 0.60035 ± 0.00168 | 0.60035 ± 0.00085 |
| $S_3$ | -0.03982 | -0.03981 ± 0.00206 | -0.03982 ± 0.00103 |
| $S_4$ | -0.21502 | -0.21502 ± 0.00243 | -0.21502 ± 0.00124 |
| $S_5$ | 0.00000 | 0.00000 ± 0.00232 | 0.00000 ± 0.00117 |
| $A_{FB}$ | 0.00000 | 0.00000 ± 0.00142 | 0.00000 ± 0.00071 |
| $S_7$ | 0.00000 | 0.00000 ± 0.00246 | 0.00000 ± 0.00125 |
| $S_8$ | 0.03715 | 0.03715 ± 0.00253 | 0.03715 ± 0.00129 |
| $S_9$ | -0.08874 | -0.08873 ± 0.00211 | -0.08874 ± 0.00106 |
| $F_S$ | | 0.00000 ± 0.00375 | 0.00000 ± 0.00188 |
| $S_{s1}$ | | 0.00000 ± 0.00439 | 0.00000 ± 0.00226 |
| $S_{s2}$ | | 0.00000 ± 0.00281 | 0.00000 ± 0.00142 |
| $S_{s3}$ | | 0.00000 ± 0.00246 | 0.00000 ± 0.00124 |
| $S_{s4}$ | | 0.00000 ± 0.00267 | 0.00000 ± 0.00135 |
| $S_{s5}$ | | 0.00000 ± 0.00300 | 0.00000 ± 0.00151 |

**Table 5.2:** Fit results to the Run 1 and Run 2 $B^0 \to K^{0*} J/\psi$ simulated data compared to the parameter values used to generate these simulations.

## 5.3 Background model

Several backgrounds were considered for the control channel, as discussed in Section 3.1.2. In the analysis of $B^0 \to K^{0*} J/\psi$ decays two of the backgrounds are modeled: the combinatorial background and the misidentified $\Lambda_b$ decays. These two backgrounds are modeled separately in mass and angles, assuming factorization. The remaining backgrounds are considered to be marginal and are thus not explicitly modelled in the fit.

### 5.3.1 Invariant mass background

The distribution of the transverse momentum has an approximately exponential behavior and the pseudo-rapidity has an approximately flat distribution. Since the particles making up the combinatorial background are combined at random, their invariant mass distribution is expected to be exponential. It is also found in data that an exponential distribution describes the combinatorial background around the $B$ mass well [59].

In case of the background originating from the misidentified $\Lambda_b$ decays, the $\Lambda_b$ invariant mass is modeled with a double Crystal Ball function, similar to that used for the $B$ mass in $B^0 \to K^{0*}J/\psi$ decays. The parameters of the model are obtained from a fit to the simulated $\Lambda_b \to pKJ/\psi(\to e^+e^-)$ data. The available $\Lambda_b \to pKJ/\psi(\to e^+e^-)$ samples are low in statistics, with only 823 events available from all simulated data sets. To improve the quality of the four-dimensional fit to the collected data, the initial parameters of the PDF of this background are obtained from a fit to all available simulated data, which includes data from both Run 1 and Run 2. The results of this fit are given in Figure 5.3 and Table 5.3.

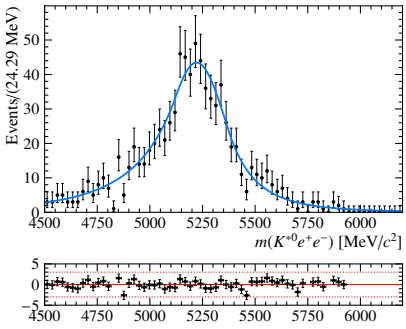


**Figure 5.3:** Mass fit to the B mass in $\Lambda_b \to pKJ/\psi(\to e^+e^-)$ decays in simulated data combined for Run 1 and Run 2.

| par. | Fitted value | |
|---|---|---|
| $\mu$ | 5222 | $\pm$ 10 |
| $\sigma$ | 138.1 | $\pm$ 17.4 |
| $\alpha_0$ | 0.7134 | $\pm$ 0.1029 |
| $\alpha_1$ | 1.117 | $\pm$ 0.159 |

**Table 5.3:** Fit results from the $B$ mass fit in $\Lambda_b \to pKJ/\psi(\to e^+e^-)$ decays in simulated data combined for Run 1 and Run 2.

### 5.3.2 Angular background

The combinatorial background in the angular distributions is modeled using Chebyshev polynomials of order up to two. To account for the acceptance effects in the background as well as the signal, the same acceptance parametrisation (see

Section 4.4) is applied also to the combinatorial background PDF.

Analogously to the background parametrisation of the invariant mass distribution, the angular background parametrisation of the misidentified $\Lambda_b$ decays comes from a fit to the simulated data. The background is parametrized with a signal-like PDF, including the acceptance effects.

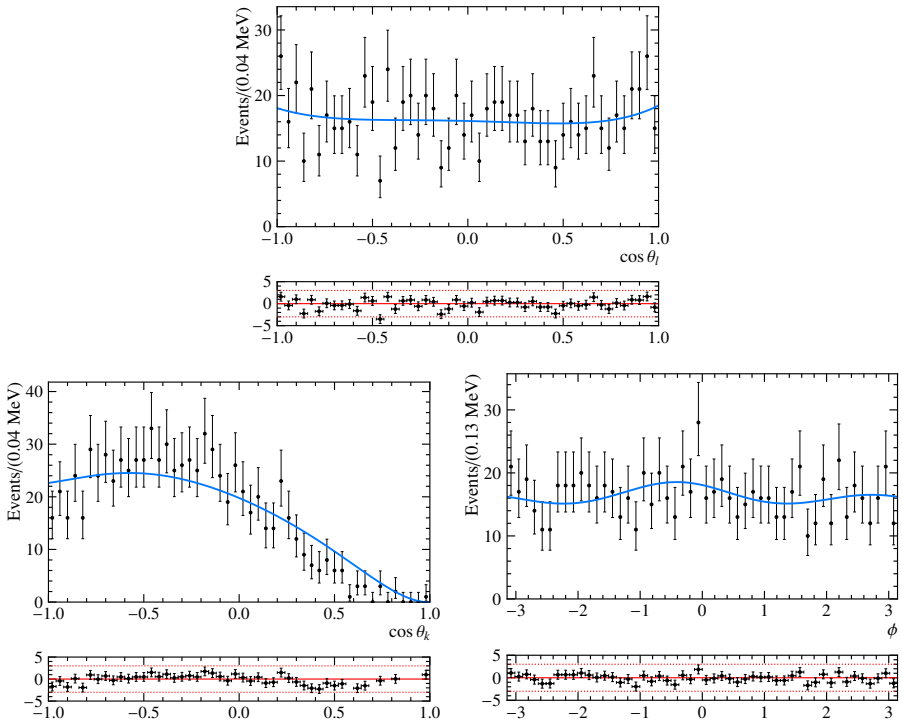


**Figure 5.4:** Fit to the angular distributions in $\Lambda_b \to pKJ/\psi(\to e^+e^-)$ decays in the combination of simulated data for Run 1 and Run 2.

Figure 5.4 shows the results of the fit to the simulated data, the fit results are shown in Table 5.4. These results are not expected to correspond to the actual angular distributions with which the events were generated, since the efficiency function is strictly only applicable to $B^0 \to K^{0*}J/\psi$ decays.

| param. | fit value |
|---|---|
| $F_{\mathrm{L}}$ | 0.20603 ± 0.02736 |
| $S_3$ | 0.03682 ± 0.04657 |
| $S_4$ | 0.08938 ± 0.05348 |
| $S_5$ | -0.01448 ± 0.04182 |
| $A_{\mathrm{FB}}$ | -0.01267 ± 0.03416 |
| $S_7$ | 0.02734 ± 0.04867 |
| $S_8$ | -0.00565 ± 0.05305 |
| $S_9$ | -0.06396 ± 0.04583 |
| $F_{\mathrm{S}}$ | 0.11895 ± 0.07148 |
| $S_{s1}$ | -0.70769 ± 0.05420 |
| $S_{s2}$ | 0.01452 ± 0.06053 |
| $S_{s3}$ | 0.05349 ± 0.04963 |
| $S_{s4}$ | -0.02815 ± 0.05000 |
| $S_{s5}$ | 0.06464 ± 0.06190 |

**Table 5.4:** Results of the fit to the angular distributions in $\Lambda_b \to pKJ/\psi(\to e^+e^-)$ decays in the combination of simulated data for Run 1 and Run 2.

## 5.4 Fits to the collected data

The PDF parameters $S_i$ are extracted using a maximum likelihood fit. The signal shape in mass and decay angles is parametrized analytically as described in Section 5.2. The background shape parametrisation was described in Section 5.3.

### 5.4.1 Invariant mass fit

Obtaining a good mass fit demonstrates a good control of the background modeling. Figure 5.5 shows the results of the fit to the Run 1 and Run 2 data. The resulting fit parameters are shown in Table 5.5.

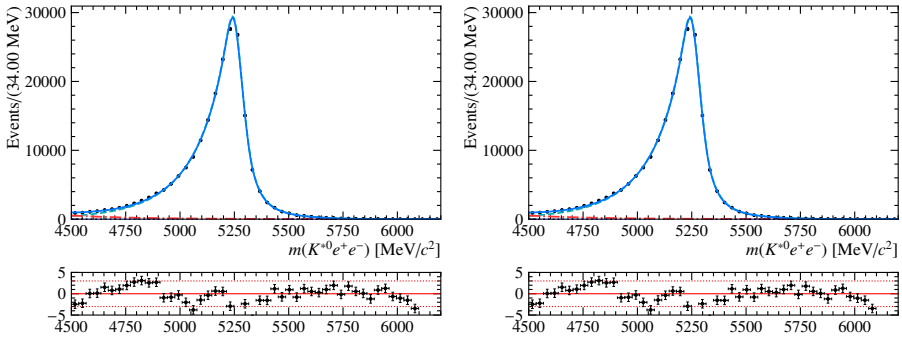


**Figure 5.5:** Fit to the $B$ invariant mass in collected data for Run 1 (*left*) and Run 2 (*right*). The green line corresponds to the signal, the red one to the combinatorial background, and the navy one to the misidentified $\Lambda_b$ background.

| par. | Run 1 | | Run 2 | |
|---|---|---|---|---|
| $\delta_\mu$ | 13.91 | ± 0.49 | 2.62 | ± 0.24 |
| $\delta_\sigma$ | 1.018 | ± 0.008 | 0.963 | ± 0.0036 |
| $\lambda$ | -0.0038 | ± 0.00056 | -0.0037 | ± 0.00017 |
| $\text{yield}_{\text{sign}}$ | 54270 | ± 280 | 201800 | ± 510 |
| $\text{yield}_{\text{comb}}$ | 1073 | ± 160 | 4510 | ± 240 |

**Table 5.5:** Results of the fit to $B$ invariant mass simulated data for Run 1 (*left*) and Run 2 (*right*), with the backgrounds included.

The yield of the misidentified $\Lambda_\text{b}$ background is not one of the fit parameters.

Since the shape of this background is very similar to that of the signal, it is very difficult to separate it. Therefore, it is fixed using the known ratio in Equation (5.5).

### 5.4.2 Four-dimensional fit

A maximum likelihood fit to invariant mass and decay angles is performed in order to obtain the angular coefficients, using the full available LHCb data set. As described in Section 5.2.2, the angular PDF follows Equation (1.16) and includes the description of both P- and S-wave states. To prove the necessity of including both of them in the PDF, a four-dimensional fit to Run 2 data was performed in two modes: using only the P-wave contribution first, and then including the modeling of the S-wave and their interference. The results of the fit are summarized in Table 5.6 and the angular distributions overlaid with the best fit model are shown in Figure 5.6, with P-wave included in the fit on the left side and both P- and S-wave included in the fit on the right.

| par. | P-wave only | P- and S-wave |
|---|---|---|
| $F_L$ | 0.5681 ± 0.0016 | 0.5586 ± 0.0018 |
| $S_3$ | -0.0039 ± 0.0020 | -0.0038 ± 0.0023 |
| $S_4$ | -0.2290 ± 0.0024 | -0.2448 ± 0.0027 |
| $S_5$ | -0.0045 ± 0.0023 | -0.0049 ± 0.0025 |
| $A_{FB}$ | 0.0001 ± 0.0015 | 0.0017 ± 0.0016 |
| $S_7$ | -0.0012 ± 0.0024 | -0.0005 ± 0.0026 |
| $S_8$ | -0.0445 ± 0.0025 | -0.0545 ± 0.0027 |
| $S_9$ | -0.0740 ± 0.0020 | -0.0849 ± 0.0023 |
| $F_S$ | | 0.0608 ± 0.0039 |
| $S_{s1}$ | | -0.1958 ± 0.0046 |
| $S_{s2}$ | | 0.0288 ± 0.0030 |
| $S_{s3}$ | | -0.0005 ± 0.0027 |
| $S_{s4}$ | | -0.0038 ± 0.0028 |
| $S_{s5}$ | | -0.0618 ± 0.0031 |

**Table 5.6:** Fit results to the Run 2 $B^0 \to K^{0*}J/\psi$ data with parametrizations including only P-wave (*left*) and including both P-wave and S-wave and their interference (*right*). The indicated uncertainties are only statistical.

The difference between the quality of both fits is quite visible in the angular

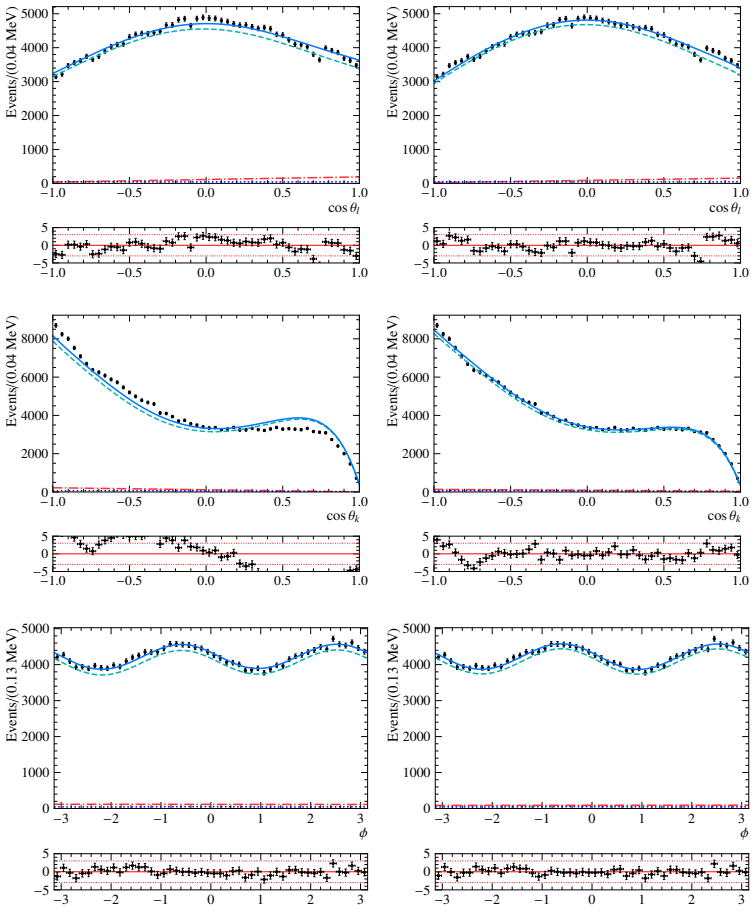


**Figure 5.6:** Distribution of the angular variables in Run 2 $B^0 \to K^{0*} J/\psi(\to e^+e^-)$ data. The parametrisations from fits including only P-wave (*left*) and including both P-wave and S-wave and their interference (*right*) are also shown. The dashed green line corresponds to the signal component, dashed red to the combinational background, dashed purple to the misidentified $\Lambda_b$ decays. The solid blue line corresponds to the sum of all of these components.

distributions, especially in the $\cos\theta_K$ distribution. This comparison confirms that including the S-wave modeling is necessary and subsequent fits were performed including the modeling of both P- and S-wave and their interference.

The four-dimensional maximum likelihood fit is performed in three data sets: only Run 1, only Run 2 and both Run 1 and Run 2 combined in a simultaneous fit. As discussed in Section 4.5, the acceptance parametrisation was obtained separately for Run 1 and Run 2 and two separate parametrisations were used also in the simultaneous fit.

The values of the angular parameters resulting from all three fits are shown in Table 5.7 and Figure 5.7; the uncertainties are only statistical. The distributions of the invariant mass and decay angles overlaid with the best fit model are shown in Figure 5.9 for the individual fits to Run 1 (*left*) and Run 2 (*right*) and in Figure 5.8 for the simultaneous fit to Run 1 and Run 2.

There is a discrepancy between the $F_{\mathrm{L}}$ parameters obtained in the various fits, at the level of $2.6\sigma$. Since the acceptance is parametrised separately for each of the runs, the effect must be of a different origin, not understood yet. Another visible discrepancy concerns the parameter $S_{s1}$, which is connected to the interference of the P- and S-waves. As it was discussed in Section 4.5, there is a slight dependence of the acceptance on the invariant mass of the $K\pi$ system, $m_{K\pi}$, which is ignored in this fit. It will be accounted for in the fit presented it Section 5.4.3 and there will be a systematic uncertainty assigned to it.

| par. | Run 1 | Run 2 | Run 1 + Run 2 |
|---|---|---|---|
| $F_{\mathrm{L}}$ | 0.5432 ± 0.0034 | 0.5557 ± 0.0018 | 0.5530 ± 0.0016 |
| $S_3$ | -0.0039 ± 0.0044 | -0.0035 ± 0.0023 | -0.0035 ± 0.0020 |
| $S_4$ | -0.2419 ± 0.0051 | -0.2424 ± 0.0027 | -0.2431 ± 0.0024 |
| $S_5$ | -0.0047 ± 0.0048 | -0.0050 ± 0.0025 | -0.0050 ± 0.0022 |
| $A_{\mathrm{FB}}$ | -0.0050 ± 0.0031 | 0.0013 ± 0.0016 | 0.0000 ± 0.0014 |
| $S_7$ | -0.0048 ± 0.0050 | -0.0002 ± 0.0026 | -0.0012 ± 0.0023 |
| $S_8$ | -0.0459 ± 0.0051 | -0.0541 ± 0.0027 | -0.0537 ± 0.0024 |
| $S_9$ | -0.0856 ± 0.0046 | -0.0848 ± 0.0024 | -0.0850 ± 0.0021 |
| $F_S$ | 0.0478 ± 0.0077 | 0.0615 ± 0.0039 | 0.0591 ± 0.0035 |
| $S_{s1}$ | -0.2237 ± 0.0087 | -0.2002 ± 0.0046 | -0.2057 ± 0.0040 |
| $S_{s2}$ | 0.0295 ± 0.0058 | 0.0286 ± 0.0029 | 0.0288 ± 0.0026 |
| $S_{s3}$ | 0.0056 ± 0.0052 | -0.0001 ± 0.0026 | 0.0011 ± 0.0023 |
| $S_{s4}$ | -0.0030 ± 0.0054 | -0.0041 ± 0.0027 | -0.0039 ± 0.0024 |
| $S_{s5}$ | -0.0610 ± 0.0060 | -0.0606 ± 0.0030 | -0.0612 ± 0.0027 |

**Table 5.7:** Results of the four-dimensional fit to the Run 1 (*left*), Run 2 (*middle*) and combined Run 1 and Run 2 (*right*); the uncertainties are only statistical.

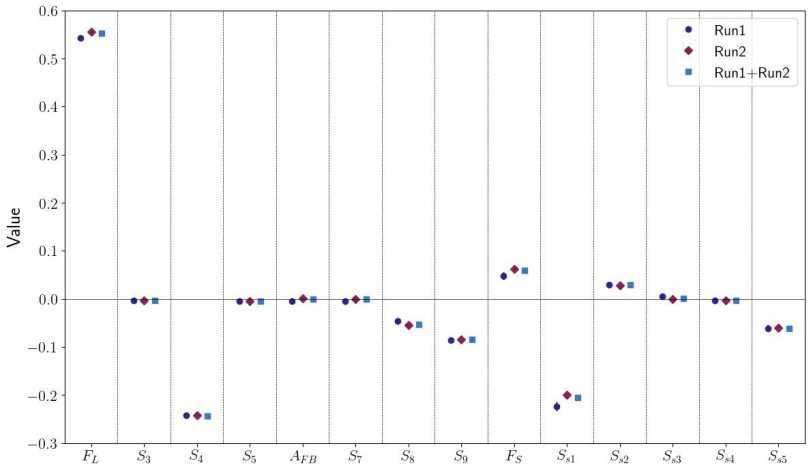


**Figure 5.7:** Results of the fits to Run 1, Run 2 and the simultaneous fit to Run1 and Run2 $B^0 \to K^{0*} J/\psi(\to e^+e^-)$ data; the uncertainties are only statistical.

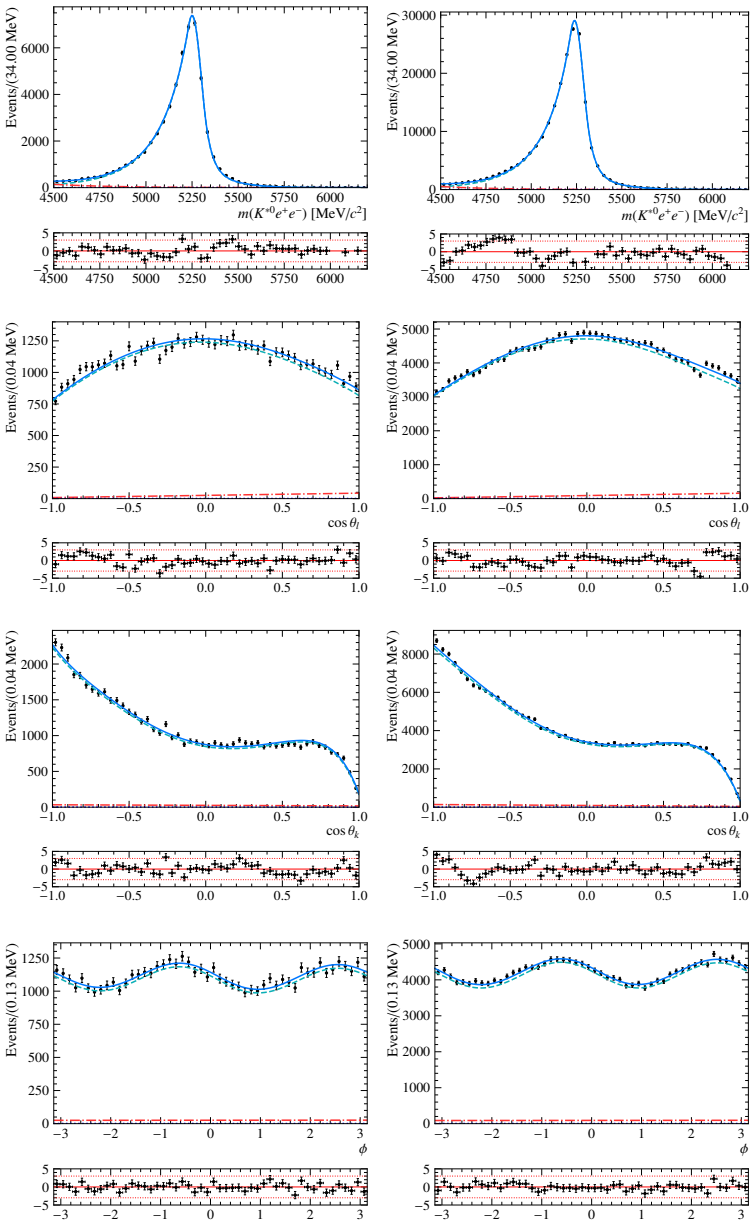


**Figure 5.8:** Results of the four-dimensional fit to invariant mass and decay angles, performed simultaneously using Run1 (left) and Run2 (right) data. Lines as in Figure 5.6.

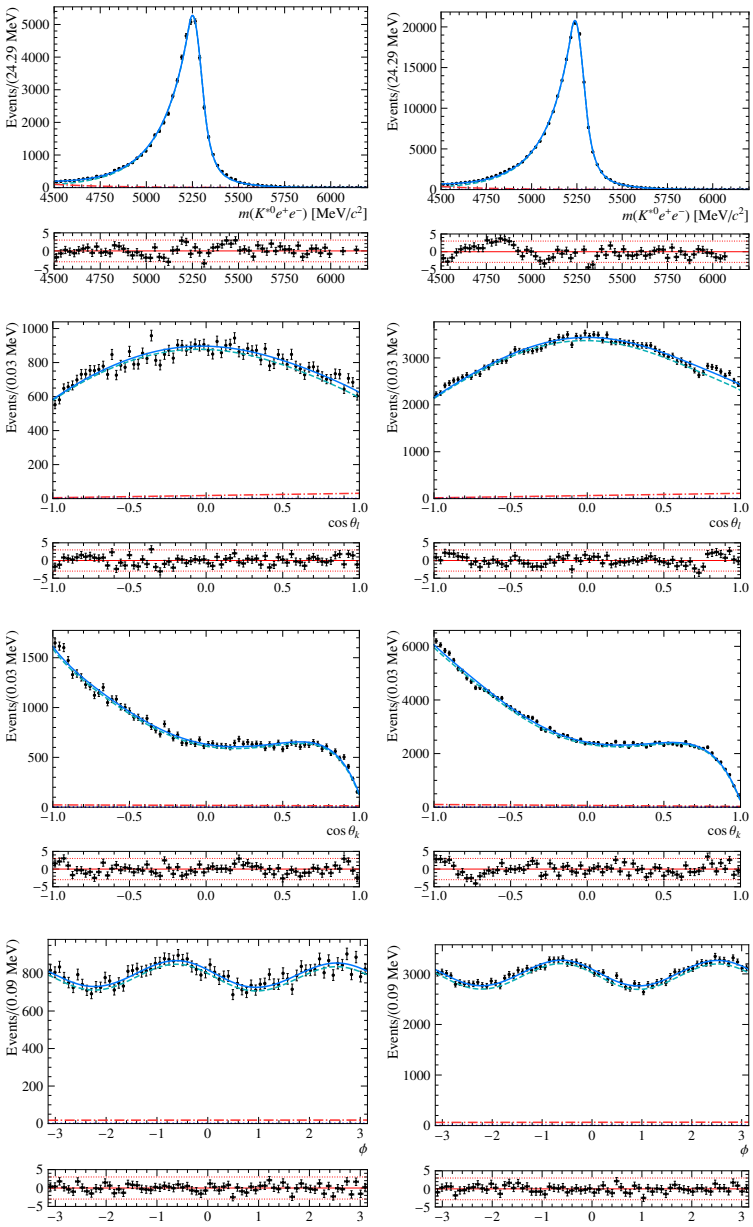


**Figure 5.9:** Results of the four-dimensional fit to invariant mass and decay angles, performed using Run 1 (*left*) and Run 2 (*right*) data. Lines as in Figure 5.6.

### 5.4.3 Four dimensional fit in $m_{K\pi}$ bins

The description of the decay presented in Section 1.3 and used throughout the analysis considers the differential decay rate dependence on four observables: the invariant mass and the angles. This approach does not include a possible dependence on the invariant mass of the $K\pi$ system, $m_{K\pi}$. To obtain the P-wave related angular parameters, modelling the $m_{K\pi}$ dependence is not necessary. However, in order to better understand the P- and S-wave interference, this dependence is accounted for by performing a binned fit in bins of $K\pi$ mass.

The $B^0 \to K^{0*} J/\psi(\to e^+e^-)$ analysis follows the $m_{K\pi}$ bins used in the $B^0 \to K^{0*} J/\psi(\to \mu^+\mu^-)$ analyses [59], as previously shown in Figure 4.8 and Table 4.4. The fit is performed using a separate angular acceptance for each of the invariant mass intervals. The largest dependence of the angular distributions on the $K\pi$ mass was observed in the distribution of $\cos\theta_K$, $\theta_K$ being the angle between the flight directions of $K$ and $B$ in $K^{0*}$ rest frame. This distribution is therefore henceforth used to illustrate the differences between the fits in the $K\pi$ mass bins. Figure 5.10 shows the $\cos\theta_K$ distribution in Run 2 data in each $m_{K\pi}$ bin, with the result of the simultaneous four-dimensional fit performed in this bin. While $m_{K\pi}$-dependent acceptance effects are not modeled in the parametrisation, these results show the importance of accounting for the $m_{K\pi}$-dependence in the angular fit itself.

It is also visible in the $\cos\theta_K$ distribution in the last two bins, $[931.0, 966.0]$ and $[966.0, 995.9]$ (Figure 5.10 bottom row), that the low values of $\cos\theta_K$ are not well described. Also the corresponding $F_{\mathrm{L}}$ values are smaller than in the other bins, as this angular parameter is very sensitive to the description of the $\cos\theta_K$ distribution. Therefore, this behaviour can be due to an efficiency problem. Alternatively, it could be a contribution from an unidentified background, that could be investigated in future studies, possibly by performing the invariant mass fit in a smaller mass range or by using a new BDT classifier with a tighter cut.

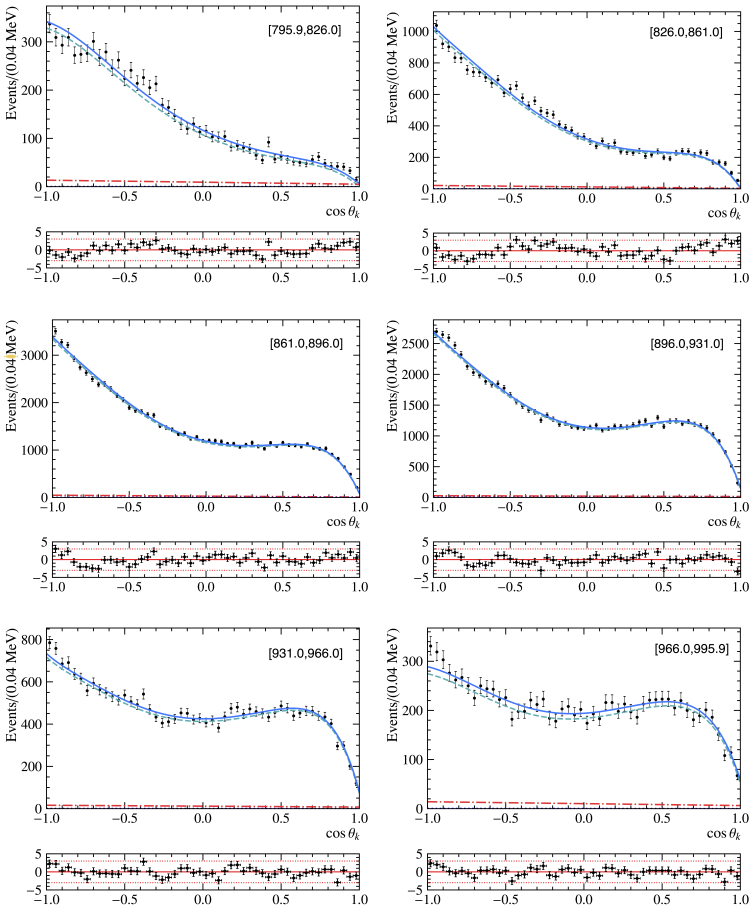


**Figure 5.10:** Distribution of $\cos\theta_K$ in bins of $m_{K\pi}$ in Run2 data presenting the results of the simultaneous fit. Lines as in Figure 5.6.

The fit results in different $m_{K\pi}$ bins are shown in Table 5.8 and in Figure 5.11. There is a clear difference between the parameter values corresponding to the P- and the S-wave interference part of the PDF. The parameters from $F_{\rm L}$ to $S_9$ are not expected to vary among the bins, while for the parameters from $F_{\rm S}$ to $S_{s5}$ a dependence on the $K\pi$ mass is expected, since the $m_{K\pi}$ dependence is connected to the presence of the S-wave. The obtained results confirm the predictions for the S-wave and interference terms, showing a large $m_{K\pi}$ dependence. The trend observed in $F_{\rm S}$ is due to the distance from the mass peak: the closer the bin is

| | $m_{K\pi}$ range in MeV/$c^2$ | | |
|---|---|---|---|
| par. | [795.9,826.0] | [826.0,861.0] | [861.0, 896.0] |
| $F_{\mathrm{L}}$ | 0.5531 ± 0.0100 | 0.57008 ± 0.00513 | 0.56096 ± 0.00253 |
| $S_3$ | -0.0383 ± 0.0136 | -0.00270 ± 0.00655 | -0.00622 ± 0.00319 |
| $S_4$ | -0.2174 ± 0.0149 | -0.24729 ± 0.00758 | -0.24437 ± 0.00377 |
| $S_5$ | -0.0200 ± 0.0140 | 0.00895 ± 0.00711 | -0.00307 ± 0.00353 |
| $A_{FB}$ | -0.0178 ± 0.0093 | 0.00193 ± 0.00458 | -0.00052 ± 0.00225 |
| $S_7$ | 0.0183 ± 0.0146 | 0.00729 ± 0.00738 | -0.00460 ± 0.00367 |
| $S_8$ | -0.0685 ± 0.0151 | -0.05984 ± 0.00761 | -0.05600 ± 0.00381 |
| $S_9$ | -0.0889 ± 0.0139 | -0.06615 ± 0.00666 | -0.08397 ± 0.00328 |
| $F_{\mathrm{S}}$ | 0.1951 ± 0.0196 | 0.07665 ± 0.01103 | 0.02439 ± 0.00567 |
| $S_{s1}$ | -0.9241 ± 0.0206 | -0.65125 ± 0.01239 | -0.30756 ± 0.00671 |
| $S_{s2}$ | 0.2114 ± 0.0146 | 0.14518 ± 0.00824 | 0.06884 ± 0.00428 |
| $S_{s3}$ | -0.0108 ± 0.0134 | -0.00346 ± 0.00743 | 0.00245 ± 0.00381 |
| $S_{s4}$ | 0.0201 ± 0.0145 | -0.01122 ± 0.00780 | -0.00610 ± 0.00400 |
| $S_{s5}$ | 0.0570 ± 0.0156 | 0.05327 ± 0.00857 | -0.02393 ± 0.00445 |

| | $m_{K\pi}$ range in MeV/$c^2$ | | |
|---|---|---|---|
| par. | [896.0, 931.0] | [931.0, 966.0] | [966.0,995.9] |
| $F_{\mathrm{L}}$ | 0.55393 ± 0.00261 | 0.527020 ± 0.00485 | 0.52583 ± 0.00809 |
| $S_3$ | -0.00243 ± 0.00333 | 0.000368 ± 0.00656 | 0.00421 ± 0.01147 |
| $S_4$ | -0.24373 ± 0.00391 | -0.243667 ± 0.00739 | -0.23163 ± 0.01237 |
| $S_5$ | -0.00712 ± 0.00367 | -0.003118 ± 0.00697 | -0.02835 ± 0.01191 |
| $A_{FB}$ | 0.00036 ± 0.00233 | 0.004643 ± 0.00445 | -0.00516 ± 0.00746 |
| $S_7$ | 0.00012 ± 0.00379 | 0.005954 ± 0.00717 | -0.02630 ± 0.01224 |
| $S_8$ | -0.04823 ± 0.00392 | -0.043636 ± 0.00729 | -0.04189 ± 0.01217 |
| $S_9$ | -0.08995 ± 0.00342 | -0.089932 ± 0.00672 | -0.09052 ± 0.01189 |
| $F_{\mathrm{S}}$ | 0.03052 ± 0.00584 | 0.112813 ± 0.01033 | 0.20126 ± 0.01597 |
| $S_{s1}$ | -0.07703 ± 0.00685 | 0.112981 ± 0.01173 | 0.16940 ± 0.01802 |
| $S_{s2}$ | -0.00404 ± 0.00445 | -0.078078 ± 0.00785 | -0.12157 ± 0.01200 |
| $S_{s3}$ | 0.00487 ± 0.00395 | -0.008466 ± 0.00710 | -0.00985 ± 0.01114 |
| $S_{s4}$ | -0.00530 ± 0.00412 | -0.000452 ± 0.00745 | 0.01311 ± 0.01175 |
| $S_{s5}$ | -0.09008 ± 0.00459 | -0.148356 ± 0.00805 | -0.20775 ± 0.01226 |

**Table 5.8:** Results of the simultaneous fit to Run1 and Run2 $B^0 \to K^{0*} J/\psi(\to e^+e^-)$ , performed in bins of the invariant mass of the $K\pi$ system.

to the peak, the smaller the fraction of the S-wave comparing to the P-wave and the interference effect is less visible. The biggest dependence can be seen in the value of the $S_{s1}$ parameter. This is connected to a highly asymmetric distribution of $\cos\theta_K$, which in Equation (1.16) appears with this parameter.

However, contrary to the expectations, the results show a very small dependence on $m_{K\pi}$ also in the P-wave-related parameters. There are deviations from average visible in the outer bins of $m_{K\pi}$, especially in the $F_{\mathrm{L}}$ parameter. This effect is indicative of a missing systematic uncertainty.

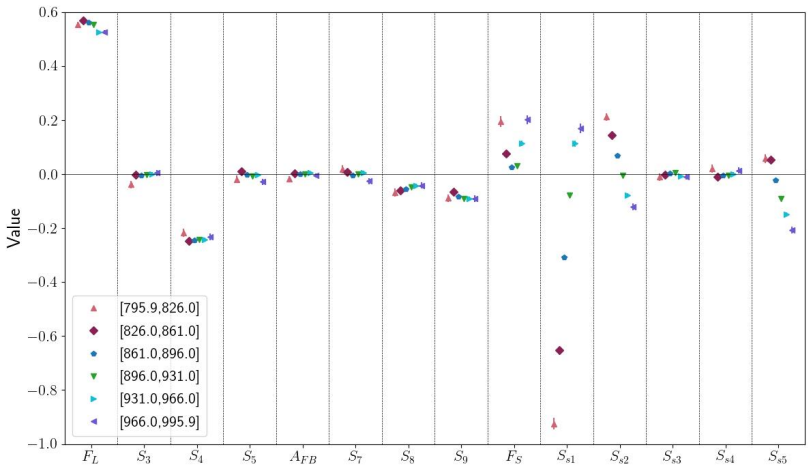


**Figure 5.11:** Results of the four-dimensional simultaneous fit to Run1 and Run2 $B^0 \to K^{0*}J/\psi(\to e^+e^-)$ data, performed in six bins of the invariant mass of the $K\pi$ system. Each point corresponds to the deviation of the parameter value from the average in the six bins.

## 5.5 Systematic uncertainties

During the analysis, several decisions are made that may lead to systematic uncertainties. The following systematic uncertainties were studied:

— **Acceptance parametrisation**: the procedure to obtain the acceptance parametrisation can introduce a systematic error, coming from the parametrisation choice and from the size of the sample that was used to obtain the parametrisation. In case of negligible background, the parametrisation choice does not introduce an error, as it does not impact the minimisation. In the

$B^0 \to K^{0*} J/\psi$ decay the signal is very clear and the low background is parametrised with a significantly less complex model than the signal. What matters in this case is the PDF normalisation. The uncertainty comes from the calculation of the efficiency moments and is dominated by the statistics of the simulation. Since in the simultaneous fit the acceptance is obtained separately for Run 1 and Run 2, the uncertainties are obtained separately as well.

— **Simulation model**: the simulation was generated according to a certain physics model and corrected for possible detector simulation discrepancies. A possible uncertainty coming from the simulation model is estimated as a difference between two extreme scenarios. In the first one, the acceptance parametrisation was obtained from simulated data that was weighted to correct for the discrepancies from the real data, as discussed in Chapter 3. In the second case, these weights were omitted. As Table 5.9 shows, in this analysis this is the dominating systematic uncertainty on the $F_L$ parameter.

— **Angular resolution**: accounting for this effect was discussed in Section 4.3. A possible error coming from this method was estimated by comparing acceptance parametrisations with and without the correction described in Section 4.1.

— **Combinatiorial background parametrisation**: the choice of the angular combinatorial background parametrisation may introduce an uncertainty. To estimate its size, two fits with different background models were compared. The first uses the nominal background parametrisation. The second one uses the same basis functions as signal. The difference between the results of these two fits is taken as the estimate of the uncertainty. It is the dominating uncertainty in the $F_{\mathrm{S}}$ parameter.

— **Misidentified $\Lambda_b^0$ background**: the fraction of the $\Lambda_b \to pKJ/\psi(\to e^+e^-)$ decays used in the analysis carries the error coming from the input used to calculate it: the fraction of the $\Lambda_{\mathrm{b}}^0$ baryon to light $B$ meson production [65], the values of branching fractions $\mathcal{B}$, and the total efficiency $\varepsilon_{\mathrm{tot}}$. The relative error on the fraction was estimated to be 19%, dominated mostly by the $\Lambda_b \to pKJ/\psi(\to e^+e^-)$ branching fraction uncertainty [1]. The systematic uncertainty of the fit parameters was calculated as the difference between the values of fit parameters obtained using the nominal value of $f$ and those obtained by varying the values of $f$ by its relative error of 19%.

— **Dependence on $m_{K\pi}$ mass**: as discussed in Section 5.4.3, this analysis does not include the $m_{K\pi}$ dependence in the differential decay rate used in the acceptance parametrisation. However, the study discussed in Section 4.5 shows a small dependence of the efficiency moments on the $m_{K\pi}$ bins. Since the simulated data do not include the S-wave, it should either be corrected for the $m_{K\pi}$ dependence or the fit should be performed in bins of $m_{K\pi}$, as it was done for results presented in Section 5.4.3. In case of the simultaneous fit performed without this binning, the systematic uncertainty was estimated as a difference between the fit parameters obtained from the simultaneous fit and those obtained from an average of the fit performed in bins of $m_{K\pi}$. This is the dominating uncertainty in the interference terms $S_{s1} - S_{s5}$.

The results of the uncertainty estimation are presented in Table 5.9. The full results of the simultaneous fit to Run 1 and Run 2 data shown in Table 5.7 are reported with statistical and systematic uncertainties in Table 5.10.

| par. | acceptance | | MC model | angular | comb. | $\Lambda_b^0$ | $m_{K\pi}$ |
|---|---|---|---|---|---|---|---|
| | Run1 | Run2 | | resolution | background | background | dependence |
| $F_{\mathrm{L}}$ | 0.0017 | 0.0009 | 0.0061 | 0.0001 | 0.0007 | 0.00006 | 0.0013 |
| $S_3$ | 0.0021 | 0.0010 | 0.0011 | 0.0001 | 0.0006 | 0.00001 | 0.0008 |
| $S_4$ | 0.0024 | 0.0012 | 0.0009 | 0.0008 | 0.0000 | 0.00004 | 0.0001 |
| $S_5$ | 0.0023 | 0.0012 | 0.0003 | 0.0001 | 0.0011 | 0.00000 | 0.0003 |
| $A_{\mathrm{FB}}$ | 0.0014 | 0.0007 | 0.0003 | 0.0000 | 0.0001 | 0.00001 | 0.0000 |
| $S_7$ | 0.0025 | 0.0012 | 0.0001 | 0.0000 | 0.0007 | 0.00000 | 0.0003 |
| $S_8$ | 0.0025 | 0.0013 | 0.0004 | 0.0013 | 0.0006 | 0.00000 | 0.0016 |
| $S_9$ | 0.0021 | 0.0011 | 0.0002 | 0.0000 | 0.0004 | 0.00000 | 0.0003 |
| $F_{\mathrm{S}}$ | 0.0037 | 0.0019 | 0.0043 | 0.0003 | 0.0105 | 0.00001 | 0.0042 |
| $S_{s1}$ | 0.0044 | 0.0023 | 0.0134 | 0.0004 | 0.0024 | 0.00009 | 0.0103 |
| $S_{s2}$ | 0.0028 | 0.0014 | 0.0010 | 0.0001 | 0.0008 | 0.00001 | 0.0021 |
| $S_{s3}$ | 0.0025 | 0.0012 | 0.0003 | 0.0000 | 0.0006 | 0.00001 | 0.0005 |
| $S_{s4}$ | 0.0027 | 0.0013 | 0.0003 | 0.0000 | 0.0006 | 0.00001 | 0.0002 |
| $S_{s5}$ | 0.0030 | 0.0015 | 0.0005 | 0.0006 | 0.0001 | 0.00003 | 0.0017 |

**Table 5.9:** List of the systematic uncertainties for each of the fit parameters.

| par. | value | $\sigma_{\text{stat}}$ | $\sigma_{\text{syst}}$ |
|---|---|---|---|
| $F_{\text{L}}$ | 0.5530 | 0.0016 | 0.0066 |
| $S_3$ | -0.0035 | 0.0020 | 0.0027 |
| $S_4$ | -0.2431 | 0.0024 | 0.0030 |
| $S_5$ | -0.0050 | 0.0022 | 0.0029 |
| $A_{\text{FB}}$ | 0.0000 | 0.0014 | 0.0016 |
| $S_7$ | -0.0012 | 0.0023 | 0.0029 |
| $S_8$ | -0.0537 | 0.0024 | 0.0036 |
| $S_9$ | -0.0850 | 0.0021 | 0.0024 |
| $F_S$ | 0.0591 | 0.0035 | 0.0128 |
| $S_{s1}$ | -0.2057 | 0.0040 | 0.0178 |
| $S_{s2}$ | 0.0288 | 0.0026 | 0.0040 |
| $S_{s3}$ | 0.0011 | 0.0023 | 0.0029 |
| $S_{s4}$ | -0.0039 | 0.0024 | 0.0031 |
| $S_{s5}$ | -0.0612 | 0.0027 | 0.0038 |

**Table 5.10:** Results of the simultaneous fit to Run 1 and Run 2 $B^0 \to K^{0*}J/\psi(\to e^+e^-)$ with statistical and systematic uncertainties.

# 6 | Results and outlook

The analysis presented in this thesis provides results for a set of angular coefficients describing the $B^0 \to K^{0*} J/\psi(\to e^+e^-)$ decay. The results were obtained from a fit to $B^0$ invariant mass and decay angles. Table 6.1 and Figure 6.1 show these results with statistical and systematic uncertainties, compared to the results from a previous analysis of the muon-decay channel, $B^0 \to K^{0*} J/\psi(\to \mu^+\mu^-)$ [59].

| par. | $B^0 \to K^{0*} J/\psi(\to e^+e^-)$ | $B^0 \to K^{0*} J/\psi(\to \mu^+\mu^-)$ |
|---|---|---|
| $F_{\mathrm{L}}$ | 0.5530 ± 0.0016 ± 0.0066 | 0.5557 ± 0.0013 ± 0.0029 |
| $S_3$ | -0.0035 ± 0.0020 ± 0.0027 | 0.0001 ± 0.0018 ± 0.0015 |
| $S_4$ | -0.2431 ± 0.0024 ± 0.0030 | -0.2518 ± 0.0020 ± 0.0016 |
| $S_5$ | -0.0050 ± 0.0022 ± 0.0029 | -0.0020 ± 0.0019 ± 0.0018 |
| $A_{\mathrm{FB}}$ | 0.0000 ± 0.0014 ± 0.0016 | 0.0005 ± 0.0012 ± 0.0010 |
| $S_7$ | -0.0012 ± 0.0023 ± 0.0029 | -0.0005 ± 0.0020 ± 0.0001 |
| $S_8$ | -0.0537 ± 0.0024 ± 0.0036 | -0.0516 ± 0.0020 ± 0.0001 |
| $S_9$ | -0.0850 ± 0.0021 ± 0.0024 | -0.0861 ± 0.0018 ± 0.0004 |
| $F_S$ | 0.0591 ± 0.0035 ± 0.0128 | 0.0647 ± 0.0021 ± 0.0007 |
| $S_{s1}$ | -0.2057 ± 0.0040 ± 0.0178 | -0.2349 ± 0.0035 ± 0.0252 |
| $S_{s2}$ | 0.0288 ± 0.0026 ± 0.0040 | 0.0228 ± 0.0022 ± 0.0022 |
| $S_{s3}$ | 0.0011 ± 0.0023 ± 0.0029 | 0.0027 ± 0.0021 ± 0.0030 |
| $S_{s4}$ | -0.0039 ± 0.0024 ± 0.0031 | -0.0007 ± 0.0021 ± 0.0002 |
| $S_{s5}$ | -0.0612 ± 0.0027 ± 0.0038 | -0.0687 ± 0.0023 ± 0.0004 |

**Table 6.1:** Comparison of the results of this study of the $B^0 \to K^{0*} J/\psi(\to e^+e^-)$ decay with those of $B^0 \to K^{0*} J/\psi(\to \mu^+\mu^-)$ [59].

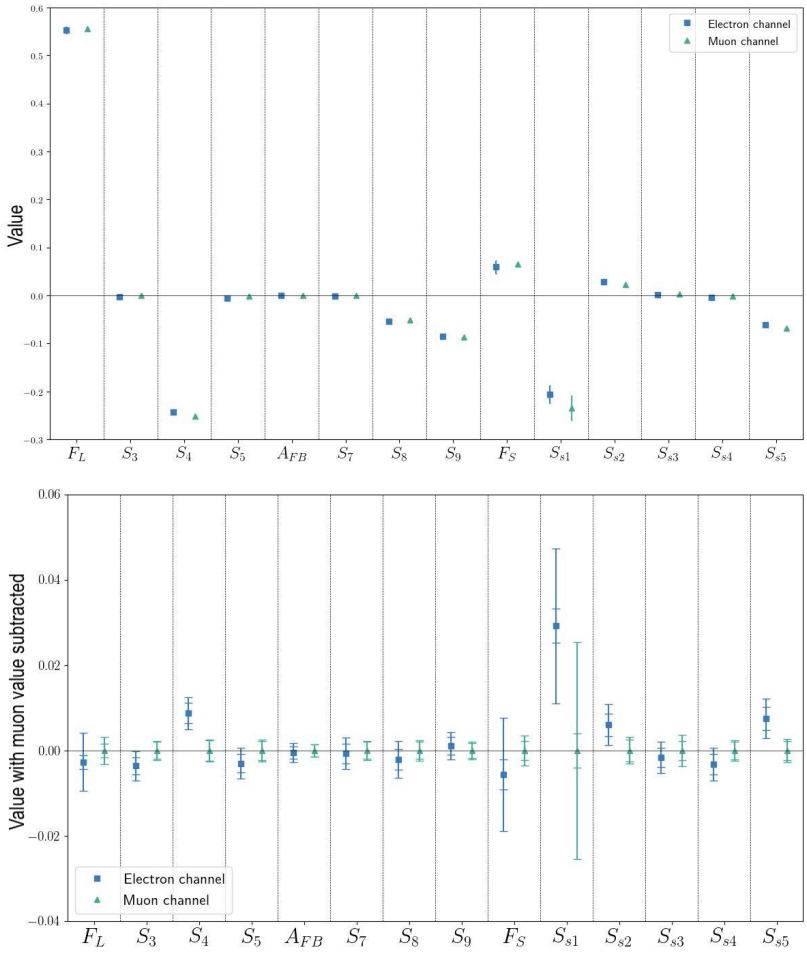


**Figure 6.1:** Results of the four-dimensional simultaneous fit to Run 1 and Run 2 $B^0 \to K^{0*}J/\psi(\to e^+e^-)$ data (see Table 5.7). The results are presented in comparison with the $B^0 \to K^{0*}J/\psi(\to \mu^+\mu^-)$ Run1 results.

The bottom panel of Figure 6.1 displays the difference between the $B^0 \to K^{0*}J/\psi(\to e^+e^-)$ results and the $B^0 \to K^{0*}J/\psi(\to \mu^+\mu^-)$ results, in order to provide a better visualisation of the small differences. Taking into account the uncertainties, the results are in good agreement. The two results show some tension in the value of the parameter $S_4$ that is likely connected to the parametrisation of $\cos\theta_K$, seen in Figure 5.10 and discussed in Section 5.4.3. This effect should be studied in the future.

In addition to the comparison with the angular analysis of the muon channel, the angular parameters obtained in this thesis can be compared with the amplitude results obtained by the $B$-factories, presented in Table 1.3.

The comparison between the angular parameters from this analysis and the amplitudes in Table 1.3 can be obtained by combining Equation (1.13) and the relations in Table 1.1. While in Table 1.1 both left- and right-chirality amplitudes are listed, for the $B^0 \to K^{0*}J/\psi(\to e^+e^-)$ channel one can assume $\mathcal{A}_{\rm L} = \mathcal{A}_{\rm R}$, since this decay, unlike the rare mode $B^0 \to K^{0*}e^+e^-$ , is dominated by the tree-level contributions, and therefore assume the parameters $S_5$, $A_{\rm FB}$, $S_7$, $S_{s3}$ and $S_{s4}$ to be zero. This is consistent with the results in Table 6.1. The values of $\mathcal{A}_\perp$, $\mathcal{A}_\parallel$, $\mathcal{A}_S$ obtained from a fit to the angular coefficients measured in this analysis (Table 6.1) are shown in Table 6.2. As can be seen, they agree with the $B$-factories measurements [30, 31] of the $B^0 \to K^{0*}J/\psi(\to \mu^+\mu^-)$ decay and previous LHCb measurement [7] of this decay within the uncertainties.

| param. | LHCb [This analysis] $B^0 \to K^{0*}J/\psi(\to e^+e^-)$ | LHCb [7] $B^0 \to K^{0*}J/\psi(\to \mu^+\mu^-)$ |
|---|---|---|
| $\lvert\mathcal{A}_\parallel\rvert^2$ | $0.227 \pm 0.002 \pm 0.004$ | $0.220 \pm 0.004 \pm 0.003$ |
| $\lvert\mathcal{A}_\perp\rvert^2$ | $0.220 \pm 0.002 \pm 0.004$ | $0.210 \pm 0.004 \pm 0.004$ |
| $\delta_\parallel$ [rad] | $-3.00 \pm 0.01 \pm 0.02$ | $-2.98 \pm 0.03 \pm 0.01$ |
| $\delta_\perp$ [rad] | $2.90 \pm 0.01 \pm 0.02$ | $2.97 \pm 0.02 \pm 0.02$ |
| $\mathrm{Re}(\mathcal{A}_S)$ | $-0.041 \pm 0.001 \pm 0.003$ | — |
| $\mathrm{Im}(\mathcal{A}_S)$ | $0.135 \pm 0.004 \pm 0.007$ | — |

| param. | BaBar [30] | Belle [31] |
|---|---|---|
| $\lvert\mathcal{A}_\parallel\rvert^2$ | $0.211 \pm 0.010 \pm 0.006$ | $0.231 \pm 0.012 \pm 0.008$ |
| $\lvert\mathcal{A}_\perp\rvert^2$ | $0.233 \pm 0.010 \pm 0.005$ | $0.195 \pm 0.012 \pm 0.008$ |
| $\delta_\parallel$ [rad] | $-2.93 \pm 0.08 \pm 0.04$ | $-2.887 \pm 0.090 \pm 0.008$ |
| $\delta_\perp$ [rad] | $2.91 \pm 0.05 \pm 0.03$ | $2.938 \pm 0.064 \pm 0.010$ |
| $\mathrm{Re}(\mathcal{A}_S)$ | — | — |
| $\mathrm{Im}(\mathcal{A}_S)$ | — | — |

**Table 6.2:** Comparison of the polarisation amplitudes $\mathcal{A}$ and their phases $\delta$, obtained from angular parameters obtained in this analysis and previous LHCb $B^0 \to K^{0*}J/\psi(\to \mu^+\mu^-)$ results assuming no S-wave component [7], BaBar [30] and Belle [31]. The uncertainties are statistical and systematic, respectively.

It can be concluded that the acceptance is well understood, although the study presented in Section 4.5 and Section 5.4.3 shows that it would be beneficial to include the $m_{K\pi}$ dependence in the acceptance modelling. Performing the fit in bins of $m_{K\pi}$ should be sufficient to addresses this issue.

It is important to remember that, with respect to $B^0 \to K^{0*}e^+e^-$ , the control channel $B^0 \to K^{0*}J/\psi(\to e^+e^-)$ has a very high statistics and therefore a much smaller statistical error. In the angular analysis of the $B^0 \to K^{0*}e^+e^-$ decay the statistical error will be dominating: since the statistics is about 400 times smaller, the error will be 20 times larger. This in turn means that the acceptance parametrisation obtained in this study will be applicable to the rare decay analysis even if not all still open issues are completely resolved.

# Bibliography


[1] R. L. Workman et al. Review of Particle Physics. *PTEP*, 2022:083C01, 2022.

[2] Standard model of elementary particles. [Accessed on July 12th, 2023].

[3] S. L. Glashow, J. Iliopoulos, and L. Maiani. Weak interactions with lepton-hadron symmetry. *Phys. Rev. D*, 2:1285–1292, Oct 1970.

[4] Gerhard Buchalla, Andrzej J. Buras, and Markus E. Lautenbacher. Weak decays beyond leading logarithms. *Reviews of Modern Physics*, 68(4):1125–1244, oct 1996.

[5] Sébastien Descotes-Genon, Diptimoy Ghosh, Joaquim Matias, and Marc Ramon. Exploring new physics in the c 7-c 7′ plane. *Journal of High Energy Physics*, 2011(6), jun 2011.

[6] Roel Aaij et al. Amplitude Analysis of the B0→K*0$\mu$+$\mu$- Decay. *Phys. Rev. Lett.*, 132(13):131801, 2024.

[7] R Aaij et al. Measurement of the polarization amplitudes in $B^0 \to J/\psi K^*(892)^0$ decays. *Phys. Rev. D*, 88:052002, 2013.

[8] R. Aleksan, A. Le Yaouanc, L. Oliver, O. Pene, and J. C. Raynal. Critical analysis of theoretical estimates for B to light meson form-factors and the B —> psi K(K*) data. *Phys. Rev. D*, 51:6235–6252, 1995.

[9] R. Aaij et al. Differential branching fraction and angular analysis of the decay $B^0 \to K^{*0}\mu^+\mu^-$. *JHEP*, 08:131, 2013.

[10] Christoph Bobeth, Gudrun Hiller, and Giorgi Piranishvili. CP Asymmetries in bar $B \to \bar{K}^*(\to \bar{K}\pi)\bar{\ell}\ell$ and Untagged $\bar{B}_s$, $B_s \to \phi(\to K^+K^-)\bar{\ell}\ell$ Decays at NLO. *JHEP*, 07:106, 2008.

[11] T. Hurth, C. Langenbruch, and F. Mahmoudi. Direct determination of Wilson coefficients using $B^0 \to K^{*0}\mu^+\mu^-$ decays. *JHEP*, 11:176, 2017.

[12] Wolfgang Altmannshofer, Patricia Ball, Aoife Bharucha, Andrzej J. Buras, David M. Straub, and Michael Wick. Symmetries and Asymmetries of $B \to K^*\mu^+\mu^-$ Decays in the Standard Model and Beyond. *JHEP*, 01:019, 2009.

[13] Sébastien Descotes-Genon, Lars Hofer, Joaquim Matias, and Javier Virto. On the impact of power corrections in the prediction of $B \to K^*\mu^+\mu^-$ observables. *JHEP*, 12:125, 2014.

[14] George F. Sterman and Paul Stoler. Hadronic form-factors and perturbative QCD. *Ann. Rev. Nucl. Part. Sci.*, 47:193–233, 1997.

[15] Marcel Algueró, Paula Alvarez Cartelle, Alexander Mclean Marshall, Pere Masjuan, Joaquim Matias, Michael Andrew McCann, Mitesh Patel, Konstantinos A. Petridis, and Mark Smith. A complete description of P- and S-wave contributions to the $\mathrm{B}^0 \to \mathrm{K}^+\pi\ell^+\ell$ decay. *JHEP*, 12:085, 2021.

[16] R. Aaij et al. Differential branching fractions and isospin asymmetries of $B \to K^{(*)}\mu^+\mu^-$ decays. *JHEP*, 06:133, 2014.

[17] Christoph Bobeth, Gudrun Hiller, and Danny van Dyk. More Benefits of Semileptonic Rare B Decays at Low Recoil: CP Violation. *JHEP*, 07:067, 2011.

[18] Christoph Bobeth, Gudrun Hiller, Danny van Dyk, and Christian Wacker. The Decay $B \to K\ell^+\ell^-$ at Low Hadronic Recoil and Model-Independent $\Delta B = 1$ Constraints. *JHEP*, 01:107, 2012.

[19] J. P. Lees et al. Measurement of Branching Fractions and Rate Asymmetries in the Rare Decays $B \to K^{(*)}l^+l^-$. *Phys. Rev. D*, 86:032012, 2012.

[20] J. T. Wei et al. Measurement of the Differential Branching Fraction and Forward-Backward Asymmetry for $B \to K^{(*)}\ell^+\ell^-$. *Phys. Rev. Lett.*, 103:171801, 2009.

[21] R. Aaij et al. Measurement of lepton universality parameters in $B^+ \to K^+\ell^+\ell^-$ and $B^0 \to K^{*0}\ell^+\ell^-$ decays. *Phys. Rev. D*, 108(3):032002, 2023.

[22] David M. Straub. flavio: a Python package for flavour and precision phenomenology in the Standard Model and beyond. 10 2018.

[23] Sebastien Descotes-Genon, Joaquim Matias, Marc Ramon, and Javier Virto. Implications from clean observables for the binned analysis of $B- > K*\mu^+\mu^-$ at large recoil. *JHEP*, 01:048, 2013.

[24] Roel Aaij et al. Measurement of $CP$-Averaged Observables in the $B^0 \to K^{*0}\mu^+\mu^-$ Decay. *Phys. Rev. Lett.*, 125(1):011802, 2020.

[25] Morad Aaboud et al. Angular analysis of $B_d^0 \to K^*\mu^+\mu^-$ decays in $pp$ collisions at $\sqrt{s} = 8$ TeV with the ATLAS detector. *JHEP*, 10:047, 2018.

[26] Albert M Sirunyan et al. Measurement of angular parameters from the decay $\mathrm{B}^0 \to \mathrm{K}^{*0}\mu^+\mu^-$ in proton-proton collisions at $\sqrt{s} = 8$ TeV. *Phys. Lett. B*, 781:517–541, 2018.

[27] S. Wehle et al. Lepton-Flavor-Dependent Angular Analysis of $B \to K^*\ell^+\ell^-$. *Phys. Rev. Lett.*, 118(11):111801, 2017.

[28] Aoife Bharucha, David M. Straub, and Roman Zwicky. $B \to V\ell^+\ell^-$ in the Standard Model from light-cone sum rules. *JHEP*, 08:098, 2016.

[29] Wolfgang Altmannshofer and David M. Straub. New physics in $b \to s$ transitions after LHC run 1. *Eur. Phys. J. C*, 75(8):382, 2015.

[30] Bernard Aubert et al. Measurement of decay amplitudes of $B \to J/\psi K^*, \psi(2S)K^*$, and $\chi_{c1}K^*$ with an angular analysis. *Phys. Rev. D*, 76:031102, 2007.

[31] R. Itoh et al. Studies of CP violation in B —> J/psi K* decays. *Phys. Rev. Lett.*, 95:091601, 2005.

[32] CERN. Accelerator Complex — CERN, 2023. [Accessed on 14th of March, 2023].

[33] Roel Aaij et al. The LHCb upgrade I. 5 2023.

[34] A. Augusto Alves, Jr. et al. The LHCb Detector at the LHC. *JINST*, 3:S08005, 2008.

[35] Marian Stahl. Machine learning and parallelism in the reconstruction of LHCb and its upgrade. *J. Phys. Conf. Ser.*, 898(4):042042, 2017.

[36] R. Aaij et al. Performance of the LHCb Vertex Locator. *JINST*, 9:P09007, 2014.

[37] J. Gassner, M. Needham, and O. Steinkamp. Layout and Expected Performance of the LHCb TT Station. 4 2004.

[38] LHCb: Inner tracker technical design report. 11 2002.

[39] M. Adinolfi et al. Performance of the LHCb RICH detector at the LHC. *Eur. Phys. J. C*, 73:2431, 2013.

[40] Roel Aaij et al. LHCb Detector Performance. *Int. J. Mod. Phys. A*, 30(07):1530022, 2015.

[41] Carlos Abellán Beteta et al. Calibration and performance of the LHCb calorimeters in Run 1 and 2 at the LHC. 8 2020.

[42] Elena Dall'Occo. *Search for heavy neutrinos and characterisation of silicon sensors for the VELO upgrade.* PhD thesis, Vrije U., Amsterdam, Vrije U., Amsterdam, 2020.

[43] LHCb muon system technical design report. 5 2001.

[44] R. Aaij et al. Test of lepton universality with $B^0 \to K^{*0}\ell^+\ell^-$ decays. *JHEP*, 08:055, 2017.

[45] Maarten van Veghel. *Pursuing forbidden beauty: Search for the lepton-flavour violating decays B0 $\to$ e$\pm$ $\mu\mp$ and Bs0 $\to$ e$\pm$ $\mu\mp$ and study of electron-reconstruction performance at LHCb.* PhD thesis, Van Swinderen Institute for Particle Physics and G, Groningen U., Groningen U., 2020.

[46] Roel Aaij et al. Design and performance of the LHCb trigger and full real-time reconstruction in Run 2 of the LHC. *JINST*, 14(04):P04013, 2019.

[47] Torbjorn Sjostrand, Stephen Mrenna, and Peter Z. Skands. A Brief Introduction to PYTHIA 8.1. *Comput. Phys. Commun.*, 178:852–867, 2008.

[48] Torbjorn Sjostrand, Stephen Mrenna, and Peter Z. Skands. PYTHIA 6.4 Physics and Manual. *JHEP*, 05:026, 2006.

[49] I. Belyaev et al. Handling of the generation of primary events in Gauss, the LHCb simulation framework. *J. Phys. Conf. Ser.*, 331:032047, 2011.

[50] D. J. Lange. The EvtGen particle decay simulation package. *Nucl. Instrum. Meth. A*, 462:152–155, 2001.

[51] N. Davidson, T. Przedzinski, and Z. Was. PHOTOS interface in C++: Technical and Physics Documentation. *Comput. Phys. Commun.*, 199:86–101, 2016.

[52] John Allison et al. Geant4 developments and applications. *IEEE Trans. Nucl. Sci.*, 53:270, 2006.

[53] S. Agostinelli et al. GEANT4–a simulation toolkit. *Nucl. Instrum. Meth. A*, 506:250–303, 2003.

[54] M. Clemencic, G. Corti, S. Easo, C. R. Jones, S. Miglioranzi, M. Pappagallo, and P. Robbe. The LHCb simulation application, Gauss: Design, evolution and experience. *J. Phys. Conf. Ser.*, 331:032023, 2011.

[55] Roel Aaij et al. Selection and processing of calibration samples to measure the particle identification performance of the LHCb experiment in Run 2. *EPJ Tech. Instrum.*, 6(1):1, 2019.

[56] M. Atzeni, A. Biolchini, M. Borsato, J. Eschle, M. Lucio Martínez, A. Mauri, M. Schubiger, N. Serra, R. Silva Coutinho, A. Snoch, and Z. Wang. Angular analysis of $B^0 \to K^{*0} e^+ e^-$ decays. LHCb-ANA-2021-024.

[57] Wikipedia. Monte Carlo Integration — Wikipedia, The Free Encyclopedia, 2023. [Accessed on May 4th, 2023].

[58] Wikipedia. Legendre Polynomials — Wikipedia, The Free Encyclopedia, 2023. [Accessed on December 6th, 2023].

[59] Roel Aaij et al. Angular analysis of the $B^0 \to K^{*0} \mu^+ \mu^-$ decay using 3 $\text{fb}^{-1}$ of integrated luminosity. *JHEP*, 02:104, 2016.

[60] L. Lyons. *STATISTICS FOR NUCLEAR AND PARTICLE PHYSICISTS*. 1986.

[61] Roger Barlow. Extended maximum likelihood. *Nuclear Instruments and Methods in Physics Research Section A: Accelerators, Spectrometers, Detectors and Associated Equipment*, 297(3):496–506, 1990.

[62] G. Cowan. *Statistical data analysis*. 1998.

[63] Jonas Eschle, Albert Puig Navarro, Rafael Silva Coutinho, and Nicola Serra. zfit: scalable pythonic fitting. 10 2019.

[64] F. James and M. Roos. Minuit: A System for Function Minimization and Analysis of the Parameter Errors and Correlations. *Comput. Phys. Commun.*, 10:343–367, 1975.

[65] R. Aaij et al. Measurement of $b$-hadron production fractions in 7 TeV pp collisions. *Phys. Rev. D*, 85:032008, 2012.

[66] Tomasz Skwarnicki. *A study of the radiative CASCADE transitions between the Upsilon-Prime and Upsilon resonances.* PhD thesis, Cracow, INP, 1986.

# Summary

Fundamental research in physics aims to answer questions about the nature of the Universe. Particle physics focuses on the fundamental forces and building blocks of matter. The best model to date is the Standard Model (SM) of particle physics. According to the Standard Model, the Universe is composed of particles that make up matter — quarks and leptons — and particles that carry the interactions between them. One of the quarks, called a beauty quark $b$, is the focus of this dissertation.

It is known that the Standard Model, while accurate, is not the most fundamental theory. Investigating the decays of the beauty quark can provide an insight into physics beyond the SM. In particular, this research focuses on the $b \to sll$ transition, where a beauty quark $b$ decays to a strange quark $s$ and two leptons of opposite charge. According to the SM, this process is very rare, making it easier to observe potential contributions from new physics, even if they are small.

This research involves measuring values predicted by the SM and comparing them with experimental results. Discrepancies between these predictions and the experimental results might indicate new physics. One promising approach consists of performing an angular analysis of a decay, focusing on the decay geometry obtained by measuring the angles between the flight directions of the decay products. The analysis is performed by fitting an angular function to the distributions of the decay angles and comparing the best-fit parameters with SM predictions.

The decay of interest in this search is $B^0 \to K^{0*}e^+e^-$ , where the $B$-meson contains the $b$-quark, the kaon $K$ contains the $s$-quark and the electron and positron are two leptons of opposite charge. To ensure reliable results, the angular analysis is performed first using a "control channel": a decay that results in the same particles but is well known and agrees with the Standard Model predictions. In this analysis, the control decay is $B^0 \to K^{0*}J/\psi(\to e^+e^-)$ . An angular analysis of this decay

is the main topic of this thesis. Detail motivations for this research are presented in Chapter 1.

These decays are produced using the Large Hadron Collider at CERN. They are registered using the particle detectors of the LHCb experiment. The experimental information allows the identification of particles and the reconstruction of their properties, such as trajectory or energy, and enables the selection of the best decay candidates. With this information, it is possible to reconstruct the geometry of the decay and perform an angular analysis. The research presented in this thesis uses data collected by the LHCb experiment between 2011 and 2018, referred to as Run 1 (2011-2012) and Run 2 (2015-2018). The experimental setup and the details of the particle reconstruction and selection are presented in Chapters 2 and 3.

One of the goals of the analysis is to account for all known factors that might affect the result. One crucial factor, arising from the particle reconstruction and selection process, is known as *acceptance effects*. These are accounted for by calculating an angular efficiency and including it in the fit to the angular distributions. The process is described in Chapter 4.

Then the final fit can be performed (Figure 1). In addition to the fit to the collected data, the uncertainty on the obtained result is estimated. This accounts for possible measurement errors arising from factors such as the amount of available data, detector effects, or incorrect modeling of the distributions. The details of the fit and the uncertainty estimation are described in Chapter 5.

The results obtained for the $B^0 \to K^{0*} J/\psi(\to e^+e^-)$ decay are compared with existing results from an analogous decay measured by the LHCb experiment, $B^0 \to K^{0*} J/\psi(\to \mu^+\mu^-)$ (Figure 2). They are also compared with results from other experiments who performed similar analyses. These comparisons, discussed in Chapter 6, show good agreement indicating that the treatment of acceptance effects and the fitting method are applicable to the main decay of interest, $B^0 \to K^{0*}e^+e^-$ .

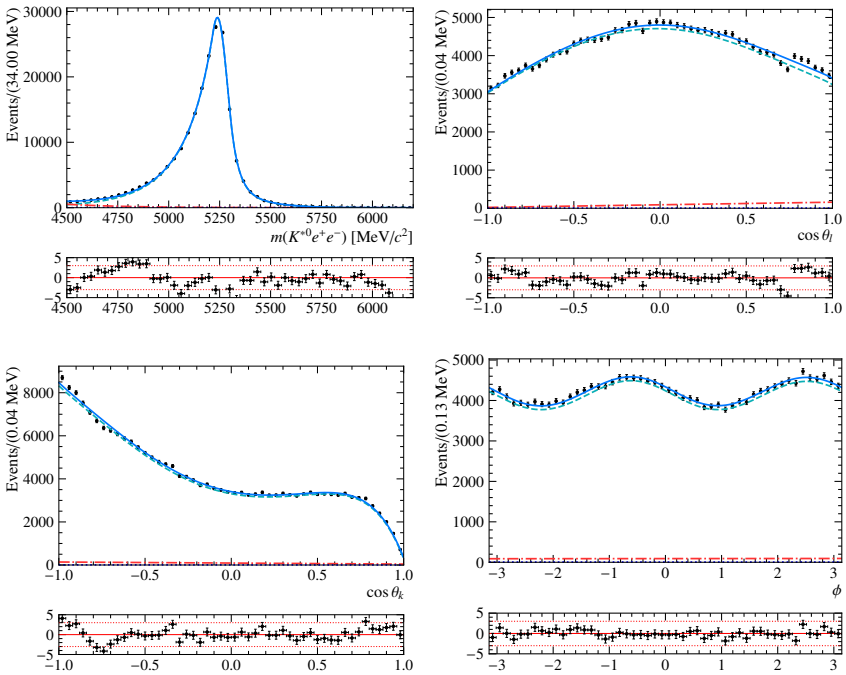


**Figure 1:** Results of the four-dimensional fit to invariant mass and decay angles, presented using Run 2 data; Figure 5.8 in Chapter 5.

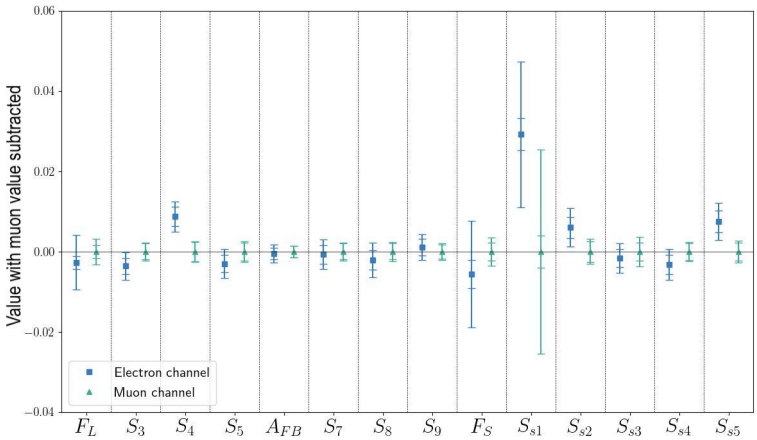


**Figure 2:** Results of the four-dimensional simultaneous fit to Run 1 and Run 2 $B^0 \to K^{0*}J/\psi(\to e^+e^-)$ data in comparison with the $B^0 \to K^{0*}J/\psi(\to \mu^+\mu^-)$ Run 1 results; Figure 6.1 in Chapter 6.

# Samenvatting

Fundamenteel onderzoek in de fysica heeft als doel vragen over de aard van het universum te beantwoorden. De deeltjesfysica richt zich op de fundamentele krachten en bouwstenen van materie. Het beste model tot nu toe is het Standaardmodel (SM) van de deeltjesfysica. Volgens het Standaardmodel bestaat het universum uit deeltjes welke materie vormen - quarks en leptonen - en deeltjes welke interacties tussen hen dragen. Een van de quarks, een beauty quark genaamd, $b$, is het onderwerp van dit proefschrift.

Het is bekend dat het Standaardmodel, hoewel accuraat, niet de meest fundamentele theorie is. Onderzoek naar het vervallen van de beauty quark kan inzicht geven in fysica voorbij/buiten het SM. Dit onderzoek richt zich, in het bijzonder, op de $b \to sll$ transitie, waarbij een beauty quark $b$ vervalt naar een strange quark $s$ en twee leptonen met tegengestelde lading. Volgens het SM is dit proces zeer zeldzaam, dat maakt het observeren van mogelijke bijdragen aan nieuwe fysica eenvoudiger, zelfs als deze bijdragen klein zijn.

Dit onderzoek omvat het meten van waarden voorspelt door het SM en de vergelijking van deze waarden met experimentele resultaten. Verschillen tussen deze voorspellingen en de experimentele resultaten kunnen wijzen op nieuwe fysica. Een veelbelovende benadering bestaat uit het uitvoeren van een hoeksanalyse van een verval, waarbij de vervalgeometrie wordt verkregen door de hoeken tussen de vluchtrichtingen van de vervalproducten te meten. De analyse wordt uitgevoerd door een hoekfunctie te passen op de verdelingen van de vervalhoeken en de best passende parameters te vergelijken met SM-voorspellingen.

Het verval van belang in dit onderzoek is $B^0 \to K^{0*} e^+ e^-$ , waarbij het $B$-meson het $b$-quark bevat, het kaon $K$ het $s$-quark bevat en het elektron en positron twee leptonen met tegengestelde lading zijn. Om betrouwbare resultaten te garanderen, wordt de hoeksanalyse eerst uitgevoerd met behulp van een "controlekanaal": een

verval dat dezelfde deeltjes oplevert maar goed bekend is en overeenkomt met de voorspellingen van het Standaardmodel. In deze analyse is het controlevel $B^0 \to K^{0*}J/\psi(\to e^+e^-)$ . Een hoeksanalyse van dit verval is het hoofdonderwerp van dit proefschrift. Gedetailleerde motivatie voor dit onderzoek wordt gepresenteerd in Hoofdstuk 1.

De betreffende vervallen worden geproduceerd met behulp van de Large Hadron Collider bij CERN en worden geregistreerd met behulp van de deeltjes detectoren van het LHCb-experiment. De experimentele informatie maakt de identificatie van deeltjes en de reconstructie van hun eigenschappen, zoals traject of energie, mogelijk en daarbij de selectie van de beste vervalkandidaten. Met deze informatie is het mogelijk om de geometrie van het verval te reconstrueren en een hoeksanalyse uit te voeren. Het onderzoek gepresenteerd in dit proefschrift maakt gebruik van gegevens verzameld door het LHCb-experiment tussen 2011 en 2018, aangeduid als Run 1 (2011-2012) en Run 2 (2015-2018). De experimentele opstelling en de details van de deeltjesreconstructie en selectie worden gepresenteerd in Hoofdstukken 2 en 3.

Een van de doelen van de analyse is alle bekende factoren, welke invloed kunnen hebben op het resultaat, in beschouwing te nemen. Een belangrijke factor welke voortkomt uit het deeltjesreconstructie- en selectieproces, staat bekend als *acceptatie-effecten*. Hier wordt rekening mee gehouden door de hoekefficiëntie te berekenen en toe te passen op de gevonden functie van de vervalhoeken. Het proces wordt beschreven in Hoofdstuk 4.

Vervolgens kan de definitieve passende functie worden uitgevoerd (Figuur 1). Naast de gevonden functie op basis van de verzamelde gegevens, wordt de nauwkeurigheid van het verkregen resultaat geschat. Waarbij rekening gehouden wordt met mogelijke meetfouten, welke voorkomen uit factoren als het aantal beschikbare gegevens, detector-effecten of onjuist modellering van de verdelingen. Een gedetailleerde beschrijving van de gevonden functie en de schatting van de nauwkeurigheid wordt gegeven in Hoofdstuk 5.

De verkregen resultaten voor het $B^0 \to K^{0*}J/\psi(\to e^+e^-)$ verval worden vergeleken met bestaande resultaten van een analoog verval, gemeten door het LHCb-experiment, $B^0 \to K^{0*}J/\psi(\to \mu^+\mu^-)$ (Figuur 2). Daarnaast zijn de verkregen resultaten ook vergeleken met resultaten van andere experimenten met soortelijke analyses. Deze vergelijkingen, besproken in Hoofdstuk 6, tonen een goede overeenstemming aan, wat aangeeft dat de behandeling van acceptantie-effecten en de fitmethode toepasbaar zijn op het hoofdverval van interesse, $B^0 \to K^{0*}e^+e^-$ .

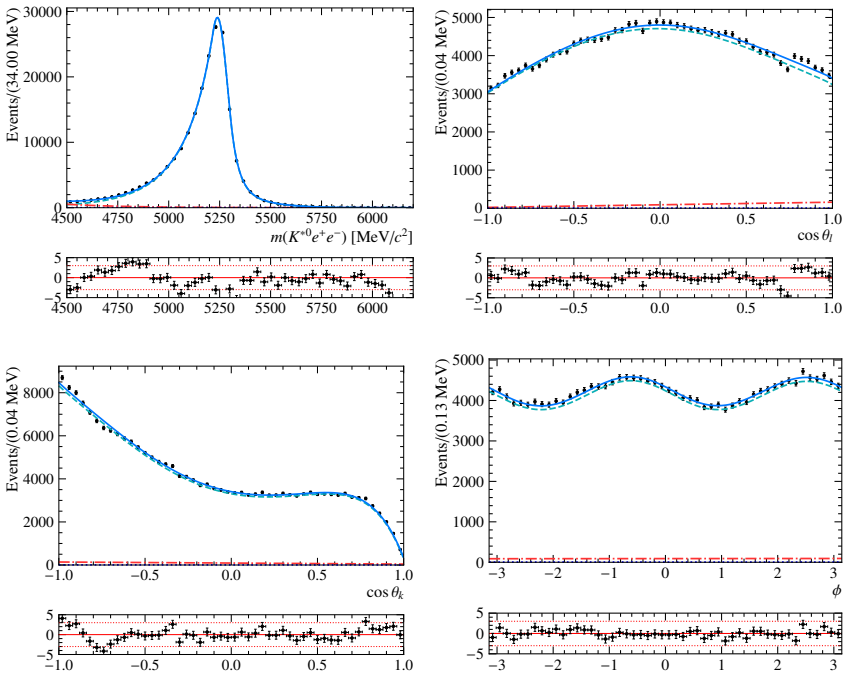


**Figuur 1:** Resultaten van de vierdimensionale fit op invariant massa en vervalhoeken, gepresenteerd met behulp van gegevens van Run 2; Figuur 5.8 in Hoofdstuk 5.

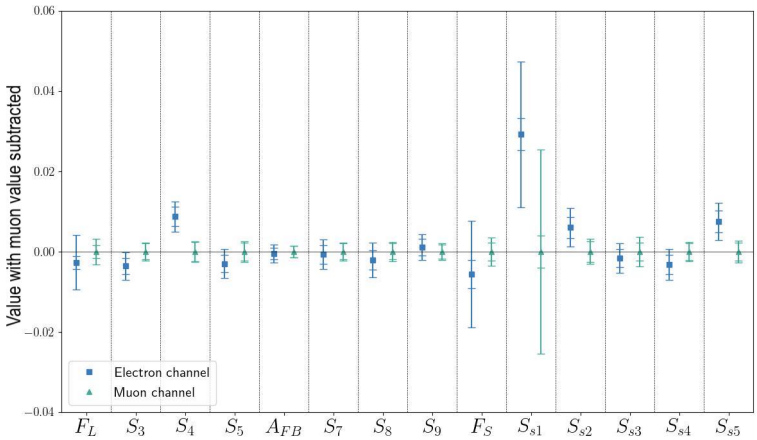


**Figuur 2:** Resultaten van de vierdimensionale gelijktijdige fit van Run 1 en Run 2 $B^0 \to K^{0*}J/\psi(\to e^+e^-)$ -gegevens in vergelijking met de $B^0 \to K^{0*}J/\psi(\to \mu^+\mu^-)$ resultaten van Run 1; Figuur 6.1 in Hoofdstuk 6.

# Streszczenie

Podstawowe badania w fizyce mają na celu znalezienie odpowiedzi na pytania dotyczące natury Wszechświata. Fizyka cząstek skupia się na oddziaływaniach podstawowych i składowych elementach materii. Obecnie najlepszym modelem w fizyce cząstek jest Model Standardowy (z ang. Standard Model, SM), według którego Wszechświat składa się z cząstek tworzących materię — kwarków i leptonów — oraz cząstek przenoszących oddziaływania pomiędzy nimi. Jeden z kwarków, zwany kwarkiem pięknym $b$, stanowi główny temat tej rozprawy.

Mimo swej trafności Model Standardowy nie jest najbardziej podstawową teorią. Badanie rozpadów kwarku pięknego może dostarczyć wglądu w możliwą fizykę wychodzącą poza SM. Między innymi badania te skupiają się na przejściu $b \to sll$ , podczas którego kwark piękny $b$ rozpada się na kwark dziwny $s$ i dwa leptony o przeciwnych ładunkach. Według SM proces ten jest bardzo rzadki, w wyniku czego łatwiej jest zaobserwować potencjalną obecność nowej fizyki, nawet jeśli jest ona niewielka.

Omawiane badanie polega na pomiarze wartości przewidywanych przez SM i porównaniu ich z wynikami doświadczalnymi. Rozbieżności między tymi przewidywaniami a wynikami z eksperymentów mogą wskazywać na nową fizykę. Jedno z obiecujących metod obejmuje przeprowadzenie analizy kątowej rozpadu poprzez badanie geometrii rozpadu uzyskanej z pomiaru kątów pomiędzy kierunkami lotu jego produktów. Analiza jest przeprowadzona poprzez dopasowanie funkcji kątowej do rozkładów kątów rozpadów i porównanie najlepiej dopasowanych parametrów z przewidywaniami SM.

Przedmiotem zainteresowania niniejszych badań jest $B^0 \to K^{0*} e^+ e^-$ , gdzie meson $B$ zawiera kwark $b$, kaon $K$ zawiera kwark $s$, a elektron i pozyton są leptonami o przeciwnych ładunkach. Aby zapewnić wiarygodne wyniki, analiza kątowa jest przeprowadzana najpierw przy użyciu „kanału kontrolnego”. Jest to rozpad o tych

samych produktach co kanał główny, dobrze znany oraz jego pomiary zgadzają się z przewidywaniami Modelu Standardowego. W tej analizie rozpadem kontrolnym jest $B^0 \to K^{0*} J/\psi(\to e^+e^-)$ . Analiza kątowa tego rozpadu jest głównym tematem tej rozprawy. Szczegółowe uzasadnienie przeprowadzenia tych badań zostało przedstawione w Rozdziale 1.

Rozpady te są wytwarzane przy użyciu Wielkiego Zderzacza Hadronów w CERN i są rejestrowane przy użyciu detektorów cząstek eksperymentu LHCb. Informacje uzyskane doświadczalnie pozwalają na rozpoznawanie cząstek i rekonstrukcję ich własności, takich jak trajektoria czy energia, umożliwiając wybór najlepszego kandydata wśród zarejestrowanych rozpadów. Dzięki tym informacjom istnieje również możliwość odtworzenia geometrii rozpadu i przeprowadzenia analizy kątowej. Badanie przedstawione w tej pracy korzysta z danych zebranych przez eksperyment LHCb w latach 2011-2018, określanych jako kampanie Run 1 (2011-2012) i Run 2 (2015-2018). Układ eksperymentalny oraz szczegóły rekonstrukcji i selekcji cząstek zostały przedstawione w Rozdziałach 2 i 3.

Jednym z zadań omawianej analizy jest uwzględnienie wszystkich znanych czynników, które mogą wpływać na wynik końcowy. Jednym z takich kluczowych czynników, wynikających z rekonstrukcji cząstek i procesu selekcji, są tzw. *efekty akceptancji*. Są one uwzględniane poprzez obliczenie wydajności kątowej i zawarcie jej w funkcji dopasowywanej do rozkładów kątowych. Proces ten opisano w Rozdziale 4.

Następnie zostało wykonane ostateczne dopasowanie funkcji kątowej (Rysunek 1). Dodakowo oszacowano również niepewność pomiarową otrzymanego wyniku. Uwzględnia ona możliwe błędy pomiarowe wynikające z takich czynników jak ilość dostępnych danych, efekty pochodzące od detektorów cząstek czy nieprawidłowe modelowanie rozkładów kątów. Szczegóły opisano w Rozdziale 5.

Wyniki uzyskane dla rozpadu $B^0 \to K^{0*} J/\psi(\to e^+e^-)$ porównano do istniejących wyników analogicznego rozpadu zmierzonego w ramach eksperymentu LHCb, $B^0 \to K^{0*} J/\psi(\to \mu^+\mu^-)$ (Rysunek 2). Porównano je także do wyników innych eksperymentów, w których została przeprowadzona podobna analiza. Porównania te, omówione w Rozdziale 6, wykazują dobrą zgodność pomiędzy wynikami, z czego można wnioskować, że parametryzacja efektów akceptancji i przedstawiona metoda dopasowania rozkładów kątów mają zastosowanie do głównego przedmiotu badań, rozpadu $B^0 \to K^{0*} e^+e^-$ .

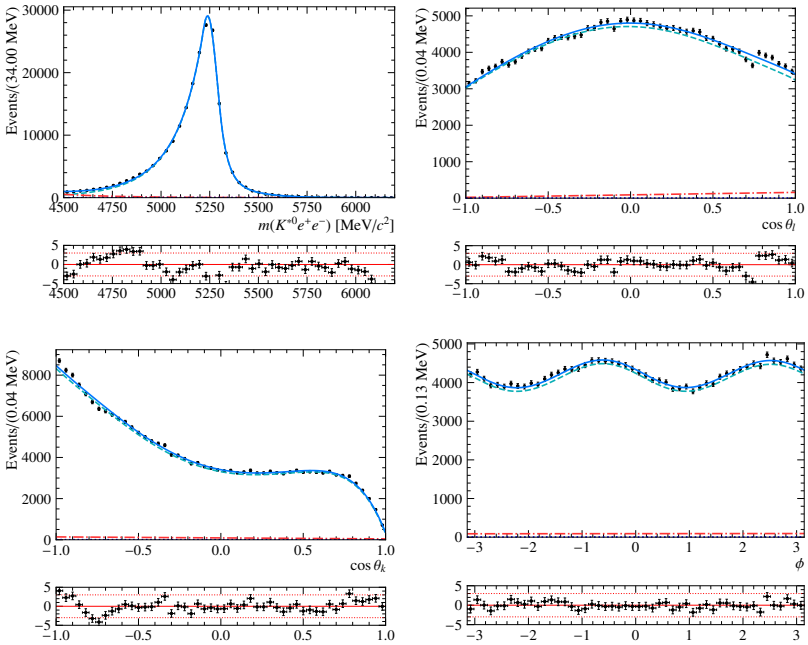


**Rysunek 1:** Wyniki czterowymiarowego dopoasywania rozkładów masy spoczynkowej i kątów rozpadu, wykonanego z użyciem danych zebranych podczas kampanii Run 2; Rysunek 5.8 w Rozdziale Chapter 5.

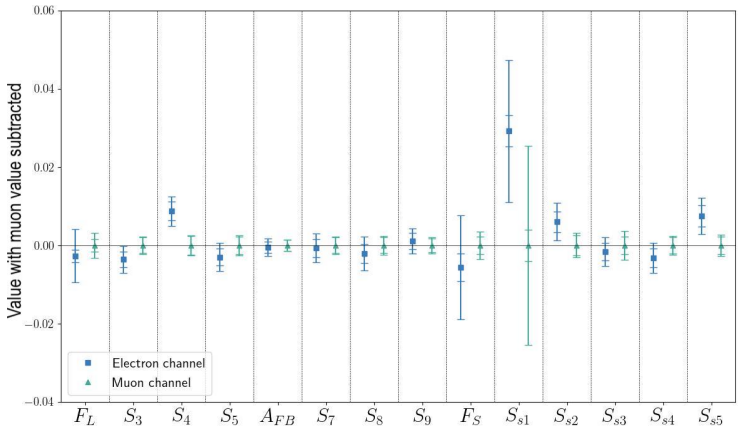


**Rysunek 2:** Wyniki analizy rozpadzu $B^0 \to K^{0*}J/\psi(\to e^+e^-)$ wykonanej z jednoczesnym użyciem danych zebranych podczas kampanii Run 1 i Run 2, porównane z wynikami z analizy rozpadu $B^0 \to K^{0*}J/\psi(\to \mu^+\mu^-)$ z użyciem danych z kampanii Run 1; Rysunek 6.1 w Rozdziale 6.

# Acknowledgements

Those of you who know me from my childhood or heard the story of the ceiling lamp know that I never planned to become a physicist. And yet, thanks to a series of *„this sounds interesting"* decisions, here I am, having written my PhD thesis and being glad for where my curiosity took me.

I do believe that finishing a PhD takes a village and completing this work would not be possible without the help and presence of so many of you.

To my supervisors, **Wouter** and **Antonio**, thank you for all the support I got from you over these years. **Wouter**, working with you was such an adventure, first building Velo and then performing this analysis. I'm very grateful for the opportunity you gave me to do my PhD here at Nikhef. Thank you for all the physics discussions, useful coding tips, and showing me how to be a scientist and have fun while doing that. **Antonio**, the support I got from you with writing this thesis is unimaginable. Thank you for always understanding what I meant, for bringing such a positive spirit, being there whenever I needed you, and for all the life, travel and science advice.

To my paranymphs, **Alice** and **Krista**, thank you for helping me make all of this happen. **Alice**, this friendship at first sight was a blessing. Thank you for doing this analysis with me, for being an amazing office mate, for all the framboise croissant mornings and pizza evenings, all the jokes and tips exchanged over the computer screens. You are such a big part of my thesis and of my life, thank you for everything. **Krista**, I had no idea that building a detector together will be such a bonding experience, but all those days of tile gluing and glue decanting brought me way more than I expected. Thank you for all the ice skating trips (and tips!) and our monthly gossip dinners. You are a great lab partner and an even better friend, thank you for being there for me.

To everyone in the Bfys group, thank you for making the years of my PhD such an amazing experience. **Lex**, my office bestie, best hiking buddy, and support in whatever I needed. Thank for for all the bouldering evenings, for the trip to Austria, checking in on me, showing over and over again that you can be kind and fight for what you believe in. And for always being two doors down the corridor, ready to discuss anything I needed to. **Brían**, the adventures we had make for a lifetime of stories. (If I loved you less, I might be able to talk about it more.) Knowing that you were there to have coffee with me carried me through all the tough days and made the good days even better. Thank you for watching all the movies with me, from *Finding Dory*, through my first watch of *Lord of the Rings*, all the way to *Only Lovers Left Alive* and *An Cailín Ciúin*. Thank you for introducing me to Irish tea (and milk!), for all the jokes, and for always being there. **Maarten**, searching for cats at the triangular square saved my sanity. Thank you for being one of the pillars of this group, showing me so many amazing restaurants, teaching me how make risotto and being my duck whenever I needed to talk about some theory or analysis details. **Daniel (Hynds)**, I am still dreaming about the curry you would make for us when we were building Velo. Thank you for being a great office mate, making sure that after hours of work in the lab we get to kick something really hard (table football ball) and swapping cucumbers and tomatoes with me. **Daniel (Magdalinski)**, I never thought I'd like liquorice but you brought me one I actually love. Thank you for the bike rides in the rain, for bouldering together, for finding that orzo recipe (!) and for somehow becoming such a close friend in such a short time. **Miriam**, thank you for sharing your life with me in our first two years in Amsterdam, surviving the lockdown together and shamelessly watching so much nonsense with me. **Lera**, you and I understand each other on another level. Thank you for always speaking your mind, understanding the *White Fang* reference, sharing the story of Mr. Oppenheimer, and letting me play with Amadeya. **Cristina**, you brought me so much comfort with the endless teas and weekly housewives. Thank you for being so compassionate, always offering support and jokes, and for all the love I received. **Silvia**, what the housewives brought together nothing can tear apart. Thank you for being so strong and for being the life of the party. **Jordy**, thank you for walking with me on the *uneven terrain* of the Netherlands, being so excited about dogs, and always committing to Halloween. **MD**, *ci sono cinque gatti...* Thank you for your passion for the proper way to make carbonara and for reminding us that naps are important. **Igor**, it's still so funny to me that I heard about this PhD position thanks you before we even knew about

each other. Thank you for bringing me here and for being my friend all these years. **Suzanne**, we had so many serious and not serious chats over tea, thank you for them. And for bringing Saartje into my life. **Emmy**, you were often the first person I saw when I came to work, and it always made me so happy. Thank you for being there and for always having time for a tea. **Efrén**, your year in Amsterdam was such a gift, thank you for all the fun we've head together. **Ganrong**, you're a ray of sunshine, thank you for making sure we have good food and believing that I can handle spice. **Maurice**, thank you for all your bouldering tips. **Sese**, I'm so glad we stayed friends even after you graduated. You were a great neighbour, thank you for all the evenings we shared, for always speaking your mind and for all the movie discussions. **Roman**, our overlap in Bfys was short and yet important, thank you for remembering how much I love quarkbällchen. **Robbert**, you're one of very few people I could take for an over-25 kmhike. Thank for you for these and for all the park lunches we had during lockdown. **Hilbrand**, thank you for creating the tradition of Bfys movie nights, willingness to take on ridiculous bets and reminding me how important is to listen to your gut. **Carolina**, *Hola! Carolina!* There was always so much geographical distance between us, but every time we met, we had so much fun. **Davide**, I promise to finally travel south of Naples. Thank you for being so kind, cheerful and supportive. **Marcel**, to had a group leader like you was a gift. Thank you for creating such an amazing atmosphere and for bringing in all the people I love so much. **Mara**, when you joined the group, you immediately took care of us. Thank you for always being there when I needed support with the analysis and for understanding all the physics- and non-physics-related topics I brought up. **Gerhard**, I will never forget those coffee breaks. Thank you for always taking time to chat with us, for explaining all the intricate details of LHCb, and for all the pop culture chats we had. **Jacco**, thank you for always having a joke ready to cheer me up. And everyone else in Bfys who I met these years, **Michele**, **Katya**, **Elena**, **Tim**, **Maxime**, **Andrea**, **Sean**, **Jan**, **Mauricio**, **Mick**, **Mark**, **Bas**, **Olaf**, **Andrii**, **Laurent**, **Niels**, **Kazu**, **Tjerd**, **Kristof**, **Chris**, **Patrick**, **Keri**, **Roel**, thank you so much for being there. I will always have you in my heart.

Everyone from the LHCb experiment, whom I met building Velo and perfoming this analysis. **Paula**, **Victor**, **Oscar**, **Peter**, **Karol**, **Stefano**, **Wiktor**, **Martin**, **Marie-Helene**, **Guillame**, **Zhenzi**, **Jonas**, **Martino**, **Nicola**, **Rafael**, thank you for joining me on this journey.

There so many other people at Nikhef, who made these years such an unforgettable experience. **Lodewijk**, thank you for all the walks and trips and being there for me. **Andrea (Spanish)**, thank you for bringing LHCb and Atlas together. You were always there to party and celebrate and to support me when I needed it, thank you for everything. **Andrea (Swiss)**, **Andrea (Italian)**, **Alis**, **Mat**, **Bouke**, **Navrit**, **Kevin**, thank you for making my time at Nikhef so great.

**Janina**, who knew that going to Moriond will bring us a friendship like this. You have been one of the most supportive people in this last year of my PhD, thank you for all the serious and non-serious chats, our Venice trip, and everything you have done and are still doing for me. **Jack**, I loved our workouts twice a week. Thank you for letting me vent, always checking in on me and making me feel so strong, because *if I can push a hundred kilogram pile of cast iron, I can also finish this*. **Sebastian**, thank you for supporting me for all these years, believing in me and sometimes knowing better than I do what I'm looking for in science.

My dearest friends from back home, who know me so well and have been with me through my whole scientific journey. **Ania**, you are my oldest friend, witnessing us grow up and both become scientist is not what I thought would happen when we sat together in school at 12 years old. Thank you always being there for me, for all the support and love. **Marysia** and **Valeriya**, *princesski*, scientifically we went in such different directions, but I couldn't be happier that we've been following and supporting each other since the first semester of our physics studies. Thank you for listening to me, for sending me love from afar, and always being there. **Emilia**, you are my biggest champion. Thank you for always believing in me, finding time to visit me in Amsterdam, and listening to all my stories. **Iza**, for so many years you've been making sure that I don't forget the creative, non-scientific part of me. Thank you for giving my mind a break, for sending me all the books that made you think about me and for bringing art to my life, I needed it a lot.

And finally, my family. **Mamo, tato, Pawle**, dziękuję wam za wszystko, za cały ogrom wsparcia i miłości. Nie byłabym tu, gdzie jestem, gdyby nie wasza wiara we mnie, wspieranie moich pomysłów, marzeń i mojej *techniczności*. Dziękuję za przypominanie mi, jak dumni ze mnie jesteście, za troszczenie się o mnie, kiedy pracowałam z Pawłowic, za chwalenie się mną, komu tylko sie dało. Kocham was ogromnie.